UC San Diego

UC San Diego Electronic Theses and Dissertations

Title

Studying binding of small molecules to protein targets using chemical, structural and computational biology methods

Permalink

https://escholarship.org/uc/item/4p01r788

Author

Shivkumar, Aashish

Publication Date

2024

Peer reviewed|Thesis/dissertation

eScholarship.org Powered by the California Digital Library
University of California

UNIVERSITY OF CALIFORNIA SAN DIEGO

Studying binding of small molecules to protein targets using chemical, structural and computational biology methods

A Dissertation submitted in partial satisfaction of the requirements
for the degree Doctor of Philosophy

in

Chemistry

by

Aashish Shivkumar

Committee in charge:

Professor Jerry Yang, Chair
Professor Rommie Amaro
Professor Pradipta Ghosh
Professor Michael Gilson
Professor Patricia Jennings

2024

©

Aashish Shivkumar, 2024

All rights reserved.

The Dissertation of Aashish Shivkumar is approved, and it is acceptable in quality and form for publication on microfilm and electronically.

University of California San Diego

2024

DEDICATION

This dissertation is dedicated to Amma, Appa, Amama and Thatha!

EPIGRAPH

Add persistence to patience, you get perseverance. Multiply perseverance, you get success.

- *Manuela George-Izunwa*

TABLE OF CONTENTS

DISSERTATION APPROVAL PAGE iii

DEDICATION iv

EPIGRAPH v

TABLE OF CONTENTS vi

LIST OF FIGURES x

LIST OF TABLES xiv

LIST OF ABBREVIATIONS xv

ACKNOWLEDGEMENTS xxi

VITA xxv

ABSTRACT OF THE DISSERTATION xxvi

Part I: Structural and functional consequences of targeting fascin with BTA 1

Chapter 1 : Introduction to spinogenic molecules and their effect on neurodegeneration 1

1.1 Alzheimer's Disease 1

1.2 Previous studies in the Yang lab - development of BTA compounds 2

1.3 Identification of fascin as a target for BTA compounds 4

1.4 Overview of work presented in part I of this dissertation 6

Chapter 2 : Changes in fascin expression affect dendritic spine density 7

2.1 Do BTA molecules induce the increase in spine density by binding to fascin? 7

2.2 Fascin is primarily an actin bundling protein 7

2.3 Fascin in neurons and dendritic spines 10

2.4 Identification of a method for fascin knockdown in primary rat neurons 12

2.6 Spine density analysis of primary neurons when fascin is knocked down 15

2.7 BTA compounds increase actin bundling activity of fascin 17

2.8 Conclusion 19

2.7 Methods 20

2.7 Acknowledgments 24

Chapter 3 : Investigation of BTA binding site on fascin using *in silico* tools and mutagenesis studies 25

3.1 Introduction 25

3.2 Molecular docking 25

3.3 Mutational analysis 33

3.4 Biochemical assays 34

3.4.3 Actin bundling assay 36

3.3.4 Isothermal Titration Calorimetry studies 37

3.5 Conclusion 41

3.6 Methods 41

3.7 Acknowledgements 45

Chapter 4 : Structural studies of fascin and BTA-EG_6 to identify key residues in their binding complex 46

4.1 Introduction 46

4.2 Previous work in the Yang lab 46

4.3 X-ray crystallography of fascin and BTA-EG_6 47

4.4 Introduction to protein NMR 49

4.5 Previous studies in the Yang lab – 2D solution NMR of WT fascin 51

4.6 Site directed mutagenesis 54

4.7 Identification of peak belonging to G390 56

4.8 Identification of peak belonging to G393 59

4.9 Selective labeling of Ala residues 61

4.10 Identification of peak corresponding to A137 63

4.11 Identification of peak corresponding to A406 66

4.12 Conclusion 68
4.13 Methods 69
4.14 Acknowledgements 71
Chapter 5 : Screening and development of small molecules that bind to fascin 72
5.1 Introduction 72
5.2 Thermal shift assay for screening BTA analogs 73
5.3 Binding studies with hits from the thermal screening assay 75
5.4 Molecular docking studies 77
5.5 *In vitro* and *in vivo* activity of BTA analogs 78
5.6 Conclusion 80
5.7 Methods 80
5.8 Acknowledgements 82
Part II: Design novel AMPKβ1 selective activators for IBD 83
Chapter 6 : Introduction 83
6.1 Inflammatory Bowel Disease 83
6.2 Identification of AMPK as a target for IBD 84
6.3 AMPK – master regulator of cell homeostasis 85
6.4 AMPK – role and function in stabilization of the gut barrier 87
6.5 Overview of approach and methodology 88
Chapter 7 : Development and screening of AMPKβ1 selective ligand 90
7.1 Introduction 90
7.2 Development of a pharmacophore model for AMPK ligands 90
7.3 Design and synthesis of novel compounds targeting AMPKβ1 93
7.4 *In silico* virtual screening of ligands from NCI datasets 95
7.4.1 Dataset Selection 95

7.4.2 Molecular Docking 95
7.5 Biochemical assays 97
7.5.1 Expression and isolation of AMPK proteins 97
7.5.2 Kinase-Glo activity assay 98
7.5.3 HeLa cell-based kinase activity assay 100
7.5.4 ITC Binding studies 102
7.5.5 Selectively of compounds binding to AMPK isoforms 103
7.6 Conclusion 107
7.7 Methods 108
7.8 Acknowledgements 112
REFERENCES 113

LIST OF FIGURES

Figure 1.1: Illustration of the chemical structures of Thioflavin T, BTA-EG_4, and BTA-EG_6 with the core and tail regions identified. 3

Figure 1.2: Illustration of the photoaffinity labeling and pulldown process by which Dr. Sibucao identified Fascin1 as a binder of the BTA-EG_4 analog probe **1** 5

Figure 2.1: Illustration of globular actin being polymerized into actin filaments followed by bundling together by fascin. 8

Figure 2.2: (A) A representation of a β-trefoil. The top view exhibits a barrel like structure formed by the β-sheets. **(B)** Crystal structure of fascin (PDB ID:1DFC[37]) with the regulatory site S39. 9

Figure 2.3: Immunofluorescent image of a mature primary rat neuron expressing a filler green fluorescent protein (GFP) stained for a microtubule associated protein used to identify dendrites (MAP2) and stained for fascin 12

Figure 2.4: Verification of Fascin knockdown in PC12 cells 14

Figure 2.5: Analysis of spine density and morphology measurements upon treatment with plasmids in primary hippocampal neurons 16

Figure 2.6: Schematic showing the polymerization of actin in the slow speed sedimentation assay. Fascin bundles free F-actin in solution. Once the bundles are formed, the fascin-actin complex can be pelleted by centrifugation. 18

Figure 2.7: Data examining the actin bundling activity of fascin at varying concentrations of fascin 18

Figure 2.8: Examination of the effects of fascin ligands on the bundling of actin filaments 19

Figure 3.1: Results from SiteMap[90] tool. Two proposed binding sites (sites 1 and 2) on fascin for small molecules were identified (solid rectangle). 26

Figure 3.2: Results from molecular docking. Representative top docked poses of BTA-EG_6 and G2 bound to fascin at sites 1 and 2, respectively. 28

Figure 3.3: 2D interactions map between fascin and BTA-EG_6 at binding site 1 between β-trefoils 1 and 4. 29

Figure 3.4: 2D interactions map between fascin and G2 at binding site 1 between β-trefoils 1 and 4. 30

Figure 3.5: 2D interactions map between fascin and BTA-EG_6 at binding site 2 between β-trefoils 1 and 2. 31

Figure 3.6: 2D interactions map between fascin and G2 at binding site 2 between β-trefoils 1 and 2. 32

Figure 3.7: Purification of recombinantly expressed fascin fusion protein. 34

Figure 3.8: CD spectra of recombinantly expressed WT and mutant fascin proteins. .. 36

Figure 3.9: Analysis of the actin bundling capability of WT fascin and seven fascin mutant proteins. 37

Figure 3.10: A) Representative binding isotherm from the titration of fascin with BTA-EG_6. **B)** Results from ITC measurements of BTA-EG_6 (1mM) and G2 (1mM) with WT fascin (100 µM)..... 38

Figure 3.11: Graphical representation of binding affinities of site 1 and site 2 fascin mutants to **A)** BTA-EG_6 and **B)** G2..... 40

Figure 4.1: X-ray crystallography of fascin using soaking method 48

Figure 4.2: Surface representation of the actin-binding site in β-trefoil-1 colored by residue conservation (*left*) and an enlarged view (*right*) showing molecules of PEG bound in the cleft formed at the interface between β-trefoil domains 1 and 4. 49

Figure 4.3: TROSY-HSQC of fascin in solution. 463 out of 477 expected peaks were visualized for 97% coverage. 52

Figure 4.4: TROSY-HSQC of fascin (blue) overlayed with TROSY-HSQC of fascin with BTA-EG_6 added (olive green)..... 53

Figure 4.5: Proposed binding site of BTA-EG_6 with fascin between beta trefoils 1 (cyan) and 4 (purple). Residues A137, A406, G390 and G393 were chosen for point mutations..... 54

Figure 4.6: A) Binding affinity data for WT fascin and fascin mutants with BTA-EG_6. **B)** Graphical representation of the binding affinities of WT fascin and fascin mutants. Each mutant was compared to WT fascin 56

Figure 4.7: TROSY-HSQC of uniformly labeled WT fascin (blue) overlayed with TROSY-HSQC of uniformly labeled fascin mutant G390S (orange). 57

Figure 4.8: Identification of peak corresponding to residue G390 59

Figure 4.9: TROSY-HSQC of uniformly labeled WT fascin (blue) overlayed with TROSY-HSQC of uniformly labeled fascin mutant G393S (red) 60

Figure 4.10: Identification of peak corresponding to G393. 61

Figure 4.11: TROSY-HSQC of uniformly labeled WT fascin (blue) overlayed with TROSY-HSQC of alanine labeled WT fascin (black)..... 63

Figure 4.12: TROSY-HSQC of uniformly labeled WT fascin (blue) overlayed with TROSY-HSQC of uniformly labeled fascin mutant A137K (pink). 65

Figure 4.13: Identification of peak corresponding to A137 66

Figure 4.14: TROSY-HSQC of uniformly labeled WT fascin (blue) overlayed with TROSY-HSQC of uniformly labeled fascin mutant A406S (green). 67

Figure 4.15: Identification of peak corresponding to A406**.** 68

Figure 5.1: A) Docked pose of BTA-EG_6 to the site between β trefoil 1 and 4 of fascin. **B)** Library of compounds used in the thermal shift screening assay. 73

Figure 5.2: A) Summary of changes in Tm of fascin induced by the presence of small molecules. **B)** First derivative of the thermal denaturation profiles (average from 4 runs) of selected hits from the thermal shift screening assay. 75

Figure 5.3: A) Summary of binding affinity data for all the BTA analogs with fascin as calculated by ITC measurements. **B)** Graphical representation of binding affinities of selected small molecules to fascin. **C)** Correlation graph between Tm and K_d data 76

Figure 5.4: Results from molecular docking of BTA analogs to the proposed binding site on fascin between β trefoil 1 and 4. **A)** BTA-EG_6 (white) **B)** E144 (cyan) **C)** D80 (yellow) **D)** D41 (pink) **E)** D46 (orange) 77

Figure 5.5: Investigation of the effects of BTA analogs on the bundling of actin filaments. 78

Figure 5.6: A) Spine density measurements in primary neurons upon treatment with BTA analogs. **B)** Representative 30 μm dendritic segments selected for dendritic spine analysis. 79

Figure 6.1: A) Boolean Network Explorer (*BoNE*) used to analyze two IBD datasets. **B)** Schematic illustrating how Boolean cluster relationships are used to chart disease paths. 85

Figure 6.2: Summary of the physiological roles of AMP-activated protein kinase (AMPK) 87

Figure 7.1: Analysis of binding site of PF compound in the crystal structure of AMPKβ1 PDB: 5KQ5[167] 91

Figure 7.2: A) Pharmacophore model for AMPK ligands **B)** Proposed series of compounds based on the computationally designed pharmacophore model. 92

Figure 7.3: Results from molecular docking studies of ligands bound to α1β1γ1 isoform of AMPK 94

Figure 7.4: Chemical structures of the top 20 compounds from the virtual screen showcasing different functional groups and scaffolds being screened. 96

Figure 7.5: Representative coomassie stained SDS-PAGE gels and western blots for AMPK and CaMKK2 proteins. **A)** α1β1γ1 **B)** α1β2γ1 **C)** CaMKK2 98

Figure 7.6: Schematic representation of the kinase-Glo assay. 99

Figure 7.7: Results from kinase-Glo luminescence assay of small molecules with AMPKβ1 100

Figure 7.8: Results from HeLa cell-based kinase activity assay. 101

Figure 7.9: A) Results from binding studies of molecules with AMPKβ1. **B)** Graphical representation of binding affinities of ligands with AMPKβ1. 102

Figure 7.10: A) Data from the kinase-Glo luminescence assay converted to reaction rates and fitted using allosteric sigmoidal model. **B)** Enzyme kinetics parameters assessed from the curve fitting model. 104

Figure 7.11: A) Results from binding studies of molecules with AMPKβ2. **B)** Graphical representation of binding affinities with AMPKβ2. 105

Figure 7.12: A) Graphical representation of binding affinities of PF and PF-CN with AMPKβ1 and AMPKβ2 isoforms. **B)** Docked poses of PF and PF-CN in the binding site of AMPKβ1 (top panel) and AMPKβ2 (bottom panel) 106

LIST OF TABLES

Table 3-1: Results from ITC measurements of site 1 fascin mutant proteins (100 μM) and BTA-EG_6 (1 mM) 39

Table 3-2: Results from ITC measurements of site 1 fascin mutant proteins (100 μM) and G2 (1 mM). 39

Table 3-3: Results from ITC measurements of site 2 fascin mutant proteins (100 μM) and BTA-EG_6 (1 mM).. 39

Table 3-4: Results from ITC measurements of site 2 fascin mutant proteins (100 μM) and G2 (1 mM). 40

Table 5-1: Results from the thermal shift screening assay. 74

LIST OF ABBREVIATIONS

AD	Alzheimer's Disease
AMPA	α-amino-3-hydroxy-5-methyl-4-isoxazolepropionic acid receptor
ASD	Autism Spectrum Disorder
AAV	Adeno-associated virus
A137	Alanine at position 137
A137K	Alanine at position 137 mutated to Lysine
A406	Alanine at position 406
A406S	Alanine at position 406 mutated to Serine
5-ASA	Amino salicylates
AI	Artificial Intelligence
AMP	Adenosine Monophosphate
ADP	Adenosine Diphosphosphate
ATP	Adenosine Triphosphate
AMPK	AMP activated protein kinase
BTA	Benzothiazole Aniline
BCA	Bicinchoninic Acid
BSA	Bovine Serum Albumin
BL21	A bacterial cell line used for expression of recombinant proteins
BoNE	Boolean Network Explorer
CMV	Cytomegalovirus
CD	Circular Dichroism
CA	Alpha Carbon

CB	Beta Carbon
CaMKK2	Calcium/calmodulin-dependent protein kinase 2
CBS	Cystathionine Beta-synthase
DIV	Days In Vitro
DNA	Deoxyribonucleic acid
DMSO	Dimethyl Sulfoxide
DTT	Dithiothreitol
D88	Aspartate at position 88
EDTA	Ethylenediaminetetraacetic acid
E215	Glutamic acid at position 215
E215A	Glutamic acid at position 215 mutated to Alanine
E492	Glutamic acid at position 492
E492A	Glutamic acid at position 492 mutated to Alanine
E. coli	Escherichia coli
EC50	Half maximal effective concentration
FBS	Fetal Bovine Serum
FPLC	Fast Protein Liquid Chromatography
G393	Glycine at position 393
G393S	Glycine at position 393 mutated to Serine
G390	Glycine at position 390
G390S	Glycine at position 390 mutated to Serine
GFP	Green Fluorescent Protein
GAPDH	Glyceraldehyde-3-phosphate-dehydrogenase

GST	Glutathione S-transferase
GI	Gastrointestinal tract
GBD	Glycogen Binding Domain
HBSS	Hank’s balanced salt solution
HEPES	4-(2-hydroxyethyl)-1-piperazineethanesulfonic acid
HSQC	Heteronuclear Single Quantum Coherence
IP	Immunoprecipitation
I45	Isoleucine at position 45
I45Q	Isoleucine at position 45 mutated to Glutamine
I93	Isoleucine at position 93
I93W	Isoleucine at position 93 mutated to tryptophan
ITC	Isothermal Titration Calorimetry
IPTG	Isopropyl β-d-1-thiogalactopyranoside
IBD	Inflammatory Bowel Disease
IL	Interleukin
kDa	Kilo Dalton
KD	Knockdown
Kd	Dissociation constant
K29	Lysine at position 29
K31	Lysine at position 31
L-CPL	Left-handed circularly polarized light
LB	Luria Broth
MAP2	Microtubule-associated protein 2

mRNA	Messenger ribonucleic acid
MOI	Multiplicity of Infection
µM	Micromolar
µL	Microliter
mM	Millimolar
µg	Microgram
MW	Molecular Weight
MRW	Mean Residue weight
MOE	Molecular Operating Environment
MHz	Mega hertz
NMR	Nuclear Magnetic Resonance
NDD	Neurodegenerative Diseases
NMDA	N-methyl-D-aspartate
nm	Nanometer
N-H	Refers to the amide N-H of a given amino acid
N48	Asparagine at position 48
N111	Asparagine at position 111
NCI	National Cancer Institute
OD	Optical density
PKC	Protein Kinase C
PDB	Protein Data Bank
PC12	A rat cell line studied for its neuronlike properties
PVDF	Polyvinylidene Fluoride

PBS-MC	Phosphate buffered saline solution supplemented with magnesium and calcium
P	Pellet
PCR	Polymerase chain reaction
PEG	Polyethylene Glycol
ppm	Parts per million
RNA	Ribonucleic acid
R389	Arginine at position 389
R389A	Arginine at position 389 mutated to Alanine
R217	Arginine at position 217
R217A	Arginine at position 217 mutated to Alanine
R-CPL	Right-handed circularly polarized light
RPM	Revolutions per minute
RMSD	Root Mean Square Deviation
R83	Arginine at position 83
RIPA	Radioimmunoprecipitation
SHSY-5Y	A human neuroblastoma cell line
SDS-PAGE	Sodium Dodecyl Sulfate Polyacrylamide Gel Electrophoresis
S39	Serine at position 39
shRNA	short hairpin RNA
S	Supernatant
ThT	Thioflavin T
TBST	Tris buffered saline solution with 0.1% tween-20
TROSY	Transverse relaxation optimized spectroscopy

TCEP	Tris(2-carboxyethyl) phosphine
Tm	Melting temperature
Thr172	Threonine at position 172
TNF-α	Tumor Necrosis Factor alpha
UV	Ultraviolet
WT	Wildtype
3xTg	A model mouse organism exhibiting Alzheimer’s Disease like symptoms

ACKNOWLEDGEMENTS

I am indebted to everyone who has been involved in making this dissertation possible. I would like to thank my advisor, Professor Jerry Yang, for giving me the opportunity to work in his lab. I am grateful for his support and mentorship. The projects that he gave me challenged me on a personal level, and I value the confidence that he had in my ability to conduct independent research. I am grateful for his patience as I grew as a scientist.

I am thankful for my committee who supported me, provided ideas and steered me in the right direction when I needed it. I am grateful to Professors Rommie Amaro and Pradipta Ghosh who welcomed me into their respective labs as a collaborator and helped me make this dissertation truly interdisciplinary through their projects. I am thankful to Professor Patricia Jennings for being my mentor outside of lab and for always being available to discuss science and life.

This work was made possible with the efforts and involvement of my many collaborators. I would like to thank Dr. Lara Dozier of the Patrick lab and Dr. Christian Seitz of the Amaro lab, for their help in completing experiments that would not have been possible in the Yang lab alone. Professor Kevin Corbett was instrumental in helping me carry out protein crystallography. I would also like to thank the NMR group consisting of Professors Galia Debelouchina and Stanley Opella, Dr. Sang Ho Park, and especially Dr. Xuemei Huang for their help in designing and carrying out protein NMR experiments. I would like to thank Dr. Geoffray Leriche and Joseph Sawires of the Yang lab for their help in making compounds that were used in all my studies. I would also like to acknowledge Dr. John Oakhill for graciously sending me plasmids that I used for the AMPK project.

Throughout my journey at UCSD, my lab mates have provided invaluable support and advice. I am thankful to all the members of the Yang lab, both old and new, for always being kind and supportive and creating an environment where I could thrive. A special mention to Dr. Kyle Berg and Dr. Meihan Li for enriching my time in the Yang lab. It was a delight to occupy the seat next to Kyle and hear him talk about his love for food, Pokémon GO, video games and his amazing family. But more importantly, I would like to thank him for being an incredible mentor. I also consider myself extremely fortunate to have had another mentor in Meihan. For whatever I know about protein expression, purification, and most of the wet lab techniques mentioned in this dissertation, I owe thanks to both Kyle and Meihan. I am thankful to her for not only being a mentor, but also one of my closest friends and allies in the Yang lab. I am grateful to her for being my pillar of strength during tough times and my partner in crime during the happier times. I am deeply indebted to her for all the sound advice and car rides, for accompanying me for late night experiments in lab as well as different restaurants and boba places. I would also like to acknowledge Dr. John Kim for his feedback and comments regarding my projects during group meetings and in general for his cheerful nature. Lastly, I would like to thank Dr. Rachel Ehrlich and Dr. Kristine Teppang for always cheering me on and being there for me throughout my time in the Yang lab.

I would not have reached this stage of writing and defending my thesis if it wasn't for my friends and peers that I met in the Chemistry department. Dr. Constanza Torres Paris for being an elder sister and always looking out for me – I am forever grateful for your presence in my life and your amazing advice on everything, science and beyond. Dr. Christian Seitz and Clark Wang for being my football buddies with whom I have shared

the most unforgettable times playing, camping and exploring different parts of San Diego – I will always cherish moments spent with you which gave me fresh perspective any time lab work was too much to handle. My current lab colleagues, Erin and Sascha, who became my close friends in the last 2 years – I am grateful for your trust in me and the opportunity to mentor you both, and I am so glad I got to know you outside of the lab.

A big thank you to Dr. Manas Likhit, who has been my roommate for almost my entire PhD, for standing by me through all the good and the bad times here at UCSD – you took care of me when I was at my lowest and I will forever be grateful for your friendship. We started our journeys at UCSD together and it is only befitting that you have seen me wrap up this chapter of my life. Heartfelt thanks to my current roommate, Dr. Pravinkumar Choudhary, for treating me as a younger brother and taking me under his wing in the later years of my PhD, helping me both in and out of lab. Thank you to Swetha Mohan for being a constant in my life and for giving me confidence in my decision to pursue a PhD – you were instrumental in me getting back on my feet after struggles in my personal life. A special mention to my friends from school – Suyash, Ayush, Chandana, Arbaz, Pranav (and Vristi), Kavya and Shubhangi, who have known me for the longest time and have stood by me and supported me through all my adventures. Also, my undergrad friends – Vivek, Benita, Jaya, Ajith and Shoaib, who have always believed in me and motivated me to pursue higher studies. Finally, my friends here in San Diego – Balaji Ganesh, Raja, Krithika, Jebin, Shubham, Balaji, Pavi, Raghav, Nitish, Mahin and Lavanya, who I spend the most time with when I am not in lab – your unwavering presence kept me going throughout these years. All my friends in the US and in India made sure that I knew I was loved and cared for and I will forever be grateful for

this feeling. Thank you to all these people for coming into my life at different stages and making their presence felt. Thank you Shradha Kabu for being so patient with me over the years while I was on this journey. I am grateful for your love, support and all the positivity that you bring into my life. I cannot imagine going through this without you being by my side and I am lucky to share this achievement with you.

Lastly, I would like to thank my parents, my brother, my grandparents and the rest of my family for all their love and support. Although I mention my immediate family in the dedication, this thesis is really dedicated to my whole family, extended family back home in India and friends in the US who became my chosen family – you are a big part of my life, thank you for always making time for me!

~ ~ ~ ~ ~ ~ ~

Chapters 2 and 3 are currently being prepared for submission for publication of the material. Aashish Shivkumar, Kyle R. Berg, Kevin C. Sibucao, Geoffray Leriche, Carla A. Espinoza, Lara Dozier, Gentry Patrick, Zied Gaieb, Christian Seitz, Rommie E. Amaro, Hyun-Hee Park, Hyang-SookHoe, Jacob Wozniak, David Gonzalez, Jerry Yang. The dissertation author is a primary researcher and author for that manuscript.

Chapter 4 is currently being prepared for submission for publication of the material. Aashish Shivkumar, Kyle R Berg, Sang-Ho Park, Galia Debelouchina, Xuemei Huang, Stanley J. Opella, Jerry Yang. The dissertation author is a primary researcher for that manuscript.

Chapter 5 is currently being prepared for submission for publication of the material. Aashish Shivkumar, Lara Dozier, Geoffray Leriche, Gentry Patrick, Jerry Yang. The dissertation author is a primary researcher for that manuscript.

VITA

2017 Bachelor of Technology in Pharmaceutical Technology, Anna University, Chennai

2019 Master of Science in Chemistry, University of California San Diego

2024 Doctor of Philosophy in Chemistry, University of California San Diego

ABSTRACT OF THE DISSERTATION

Studying binding of small molecules to protein targets using chemical, structural and computational biology methods

by

Aashish Shivkumar

Doctor of Philosophy in Chemistry

University of California San Diego, 2024

Professor Jerry Yang, Chair

The integration of chemical and structural biology with computational tools is critical in drug discovery and for developing novel therapeutics. This dissertation explores the binding of small molecules with protein targets, with a focus on protein-ligand interactions at both structural and functional levels.

In part I of this dissertation, I investigate the structural and functional consequences of targeting fascin with benzothiazole amphiphiles (BTA), compounds known to enhance memory and learning in mice and with potential applications in treating neurodegenerative diseases. Chapter 1 summarizes current research on Alzheimer's disease, the identification of fascin as a target for BTA compounds and its role and

function as an actin bundling protein. In Chapter 2, using knockdown studies in primary neurons, I show that fascin expression levels and binding of BTA to fascin are crucial for the phenotypic effect of increased dendritic spine density. In Chapter 3, I use a combination of *in silico* tools and site-directed mutagenesis experiments to identify a novel binding site for BTA compounds and provide a quantitative understanding of their binding to fascin. In Chapter 4, I provide structural evidence for the binding site of BTA-EG_6 to fascin using protein NMR studies. In Chapter 5, I screen other novel BTA analogs and identify a promising lead compound which demonstrates superior binding affinity and functional activity compared to BTA-EG_6.

In part II of this dissertation, I develop and identify potential drug candidates for Inflammatory Bowel Disease (IBD) by selectively targeting the AMPKβ1 isoform. Chapter 6 discusses the rationale for developing a new therapeutic strategy for IBD via AMPKβ1 activation, by addressing inflammation and helping to restore and maintain gut barrier integrity. Chapter 7 employs a combination of *in silico* virtual screening and synthetic chemistry to design and identify a lead compound with better potency and selectivity towards AMPKβ1.

Together, these projects represent a comprehensive approach to drug discovery by integrating computational methods, structural biology, and synthetic chemistry to advance our understanding of protein-ligand interactions and their therapeutic potential. The findings contribute to the development of targeted therapies for neurodegenerative diseases and IBD, offering new insights into drug discovery and development.

Part I: Structural and functional consequences of targeting fascin with BTA

Chapter 1 : Introduction to spinogenic molecules and their effect on neurodegeneration

1.1 Alzheimer's Disease

Alzheimer's Disease (AD) is the most prevalent age-related neurodegenerative disorder and the leading cause of dementia[1]. Early symptoms, such as memory and learning decline, typically precede significant neuronal loss [2,3]. Eventually, individuals with AD struggle to perform even basic tasks like walking and swallowing. In the later stages, patients often become bedridden and require intensive care. AD is ultimately fatal, with individuals often succumbing to complications such as pneumonia and heart failure[4]. It currently ranks as the sixth leading cause of death in the United States[5].

Age is the primary risk factor for developing AD. Approximately 5.7 million Americans live with AD, with around 5.5 million of them aged 65 and older[1]. As life expectancy increases, the prevalence of AD is expected to rise correspondingly. Projections indicate that by 2060, the number of AD patients in the U.S. will nearly triple, and the cost of care will exceed one trillion dollars[1]. The impacts of AD are extensive, affecting individuals on a personal level and having broader implications for the government and the economy.

Decades of extensive research have gone into studying AD. One of the most prevalent theories about the progression of AD is the amyloid cascade hypothesis. This theory suggests that the abnormally high levels of β-amyloid proteins found in all AD patients can aggregate to form extracellular plaques in the brain, which can lead to neuronal dysfunction and death of neurons[6]. Protein interactions with aggregated forms of β-amyloid lead to a host of problems that cause havoc on neurons and destroy synapses[7,8].

Though the amyloid cascade hypothesis does not fully explain all the features of AD, the recent development of antibody-based therapeutics that can effectively remove amyloid plaques from the brain have shown modest improvements in cognitive function in some AD patients.[9,10] The limited efficacy of these amyloid-targeting antibodies for improving memory or slowing cognitive decline in AD necessitates the development of alternative therapeutic strategies[11] to treat AD and disorders associated with memory impairment.

Synapse loss and dysfunction are key features of many neurodegenerative diseases (NDDs) and are thought to be among the earliest indicators of AD progression[2,3,12,13]. Consequently, methods that can enhance the formation and preservation of synapses could provide an effective treatment pathway for AD and other conditions that involve memory loss. The formation of excitatory synapses between neuronal axonal inputs and postsynaptic dendritic spines is essential for memory formation and storage[14]. Evidence shows a strong positive correlation between the density of hippocampal dendritic spines and cognitive abilities such as memory and learning [15,16].

1.2 Previous studies in the Yang lab - development of BTA compounds

Over the past decade, the Yang lab has been working on developing small molecules that can target amyloid aggregates. The hallmark feature of AD patients is the formation of β-amyloid plaques in the brain[6]. These extracellular plaques interact with other proteins and microglia that lead to inflammation in the brain[7,8]. The Yang lab has developed Benzothiazole Aniline (BTA) compounds such as BTA-EG_4 and BTA-EG_6 (Figure 1.1), which are uncharged oligo (ethylene glycol) derivatives of Thioflavin T[17], a traditional dye used to stain β-amyloid.

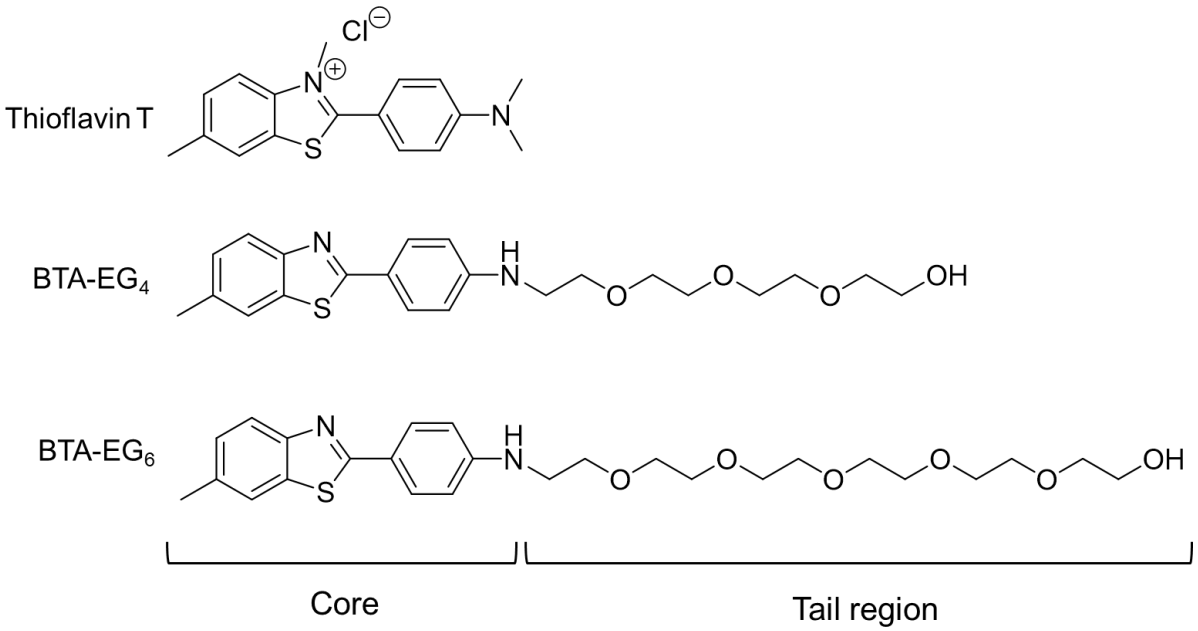


Figure 1.1: Illustration of the chemical structures of Thioflavin T, BTA-EG$_4$, and BTA-EG$_6$ with the core and tail regions identified.

BTA-EG$_4$ and BTA-EG$_6$ could both bind β-amyloid plaques and prevent other proteins from interacting with the plaques, thereby reducing inflammation in the brain[18]. Since the β-amyloid induced toxicity may result from interactions between aggregated β-amyloid peptides and essential cellular proteins, the Yang lab has specifically focused on the interference of β-amyloid with proteins that regulate reactive oxidative species levels in cells. The BTA family of compounds have shown significant potential in reducing β-amyloid induced toxicity in cells by interfering with the interaction between aggregated β-amyloid and associated proteins such as catalase[18,19].

BTA-EG$_4$ was further studied in a mouse model to assess its impact on cognitive behavior. Significantly, BTA-EG$_4$ was found to cross the blood-brain barrier in mice[18], which is crucial for a brain-targeted therapeutic. Treatment with BTA-EG$_4$ improved memory, learning, and rescued synapse loss in 3xTg AD mice[20]. Interestingly, BTA-EG$_4$

also showed beneficial effects in non-pathological conditions, enhancing memory and learning in wild-type (WT) mice as well[21]. WT mice treated with BTA-EG$_4$ demonstrated better cognitive performance in both the Morris water maze and fear conditioning tests [21]. Furthermore, analysis of neurons from both 3xTg and WT mice treated with BTA-EG$_4$ revealed an increase in the density of dendritic spines[20,21].

Dendritic spines, which are small mushroom-like actin rich structures on neuron dendrites, serve as the postsynaptic sites of synaptic connections[22,23]. Most excitatory synapses in the brain form with a dendritic spine as the postsynaptic site between neurons[23]. These spines are critical for communication, information processing, and storage in the brain. Consequently, AMPA and NMDA receptors are also found on the surface of dendritic spines[24]. Alterations or decreases in dendritic spine density are pathologies seen in AD[25] and other neurological disorders such as autism spectrum disorder (ASD) and schizophrenia[26]. Given the strong evidence linking dendritic spines to memory, an effective therapeutic strategy to combat AD and other NDDs could involve modulating dendritic spine density.

The experiments discussed above were the first to identify the nootropic effects of BTA-EG$_4$ *in vivo*. Since then, the spinogenic properties of BTA-EG$_4$ and its derivatives have been demonstrated and confirmed in rat primary neurons[27] and human neuronal induced pluripotent stem cells[28].

1.3 Identification of fascin as a target for BTA compounds

To further understand the effects of these BTA molecules, Dr. Kevin Sibucao, a former PhD student in the Yang lab, investigated the potential protein targets for these

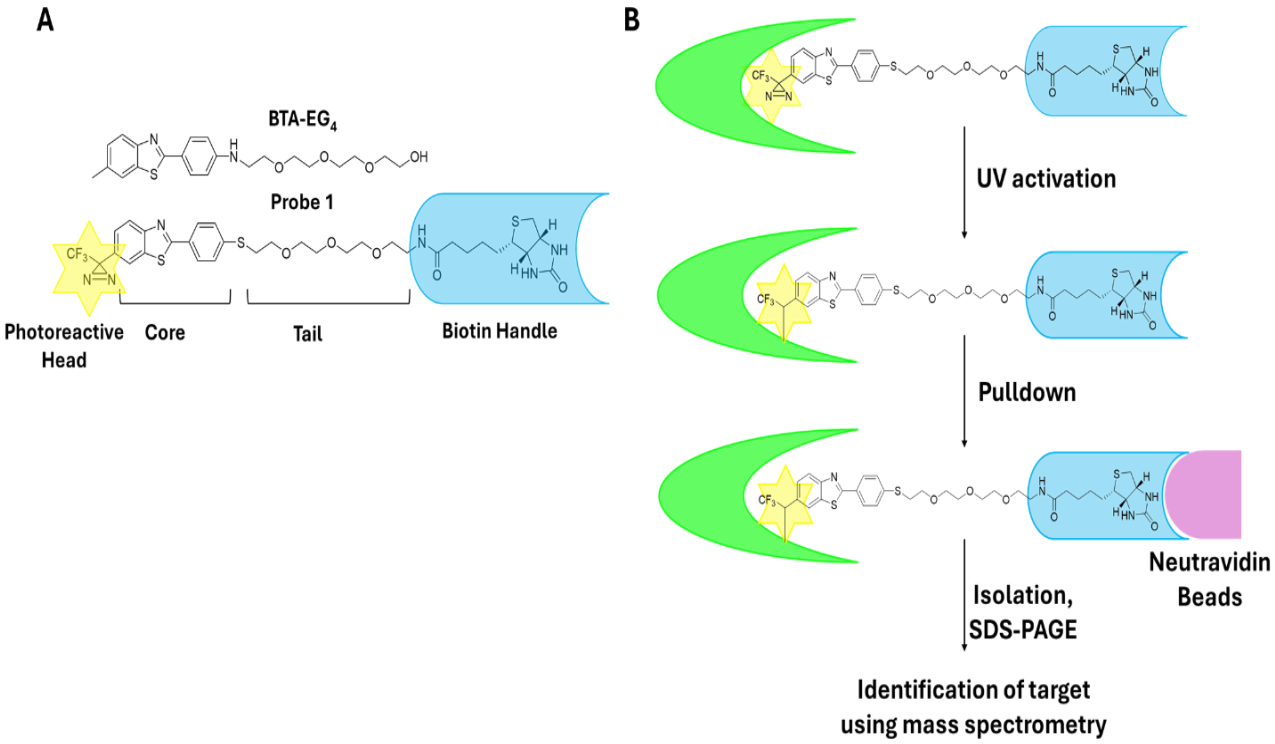


Figure 1.2: Illustration of the photoaffinity labeling and pulldown process by which Dr. Sibucao identified Fascin1 as a binder of the BTA-EG$_4$ analog probe **1**.

compounds. He utilized a photoaffinity labeling approach to identify the cellular binding partners of BTA-EG$_4$[29]. The BTA-EG$_4$-based probe **1** was equipped with a trifluoromethyl diazirine for crosslinking to nearby proteins upon UV activation. A biotin tag was also added for subsequent affinity pulldowns (Figure 1.2). Photoaffinity labeling and competition assays in cell lysates of the human cortex successfully identified a ~55kDa protein as the target of BTA-EG$_4$. Follow up affinity pull-down experiments using neutravidin-agarose resin in SH-SY5Y neuroblastoma cells were then conducted to isolate the ~55kDa protein. Tandem mass spectrometry revealed the most prominent protein as Fascin1 (hereafter referred to as fascin). Subsequent western blot analysis with a fascin antibody confirmed the presence of fascin. Additionally, pull-down studies

with human cortex and mouse midbrain tissue demonstrated that the results observed in SH-SY5Y cells were consistent across different tissue types[29].

1.4 Overview of work presented in part I of this dissertation

The intriguing activities exhibited by the BTA class of molecules and the unknown mechanisms behind BTA-EG$_{4/6}$ induced spinogenesis motivate the work in this dissertation. The first part of this dissertation focuses on investigating the structural and functional consequences of targeting fascin with BTA compounds. In subsequent chapters, I present findings related to the investigation of the following questions:

1) Is fascin on pathway for the observed phenotypic effects of BTA molecules i.e. the increase in dendritic spine density seen upon treatment with BTA compounds?
2) Can we characterize and gain structural insights into the fascin-BTA interaction and develop a better quantitative understanding of their interaction.
3) Can we improve the effectiveness of BTA-EG$_{4/6}$ by screening other BTA analogs.

Investigating these aims will help advance our understanding of novel therapeutic compounds that may be leveraged as is or modified to enhance their properties to fight the battle with cognitive loss seen in AD and other forms of dementia.

Chapter 2 : Changes in fascin expression affect dendritic spine density

2.1 Do BTA molecules induce the increase in spine density by binding to fascin?

The key question being investigated in this chapter is the involvement of fascin in the pathway leading to the observed increase in dendritic spine density in primary neurons when treated with BTA-EG_4 or BTA-EG_6. Dr. Sibucao previously demonstrated that his photoreactive analog of BTA-EG_4 binds to fascin, and this binding can be outcompeted by the addition of BTA-EG_4[29]. However, binding to a protein target does not necessarily imply a direct link to the observed cellular response. The experiments detailed in this chapter measure changes in dendritic spine density of primary neurons resulting from modulated fascin expression. These experiments are designed to test our hypothesis that fascin plays a key role in dendritic spine dynamics.

2.2 Fascin is primarily an actin bundling protein

Fascin refers to a class of proteins that binds and bundles filamentous actin[30]. Robert Kane first discovered fascin in the 1970s while isolating filamentous actin (F-actin) from sea urchin egg extracts[31]. The 58kDa protein was ultimately named “fascin” due to its ability to bundle F-actin into filopodial cores and cross-link actin filaments into fascicles[32] (Figure 2.1). In mammals, there are three isoforms of fascin, labeled 1, 2, and 3. Fascin 1 is found in many tissue types in varying quantities in young mammals, with high abundance in the brain and low quantities in the small intestine and spleen in healthy adults[33]. Fascin 2 and 3 are restricted to specific tissues; fascin 2 is expressed in the retina, while fascin 3 is expressed in the testes[34].

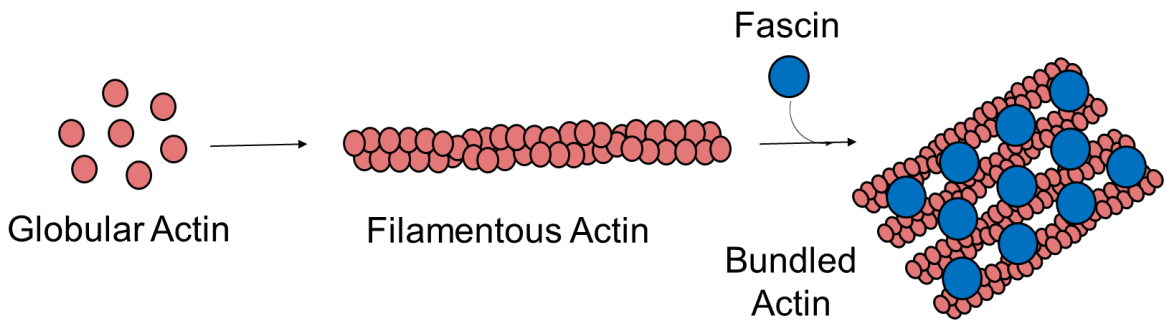


Figure 2.1: Illustration of globular actin being polymerized into actin filaments followed by bundling together by fascin.

Fascin is a globular, monomeric protein that binds actin in a 1:4 stoichiometry[35]. Extensive research has resulted in multiple crystal structures of fascin over the past two decades[35–37]. The crystal structure of fascin revealed a novel arrangement of four tandem β-trefoil domains, grouped into two pairs that act semi-independently (Figure 2.2). Fascin has a regulatory site at Ser39, which upon phosphorylation by Protein Kinase C (PKC) significantly diminishes fascin's ability to bind and bundle actin[36](Figure 2.2). This phosphorylation site contains several proximal lysine residues critical for actin binding[36,38].

Fascin is present in traditional filopodia and invadopodia, that protrude from the leading edge of the cell to explore the immediate environment surrounding the cell[39,40]. Filopodia are thin cell membrane projections which contain parallel fascin-bundled actin and have a distinctive composition as compared to dendritic filopodia which contains branched actin. Filopodia are essential for cellular functions such as migration and adhesion. The regulation, polymerization, and cross-linking of actin filaments are necessary for filopodia development. Fascin's actin bundling activity is crucial for providing the cross linked actin bundles necessary for filopodia structural support[39,41–43].

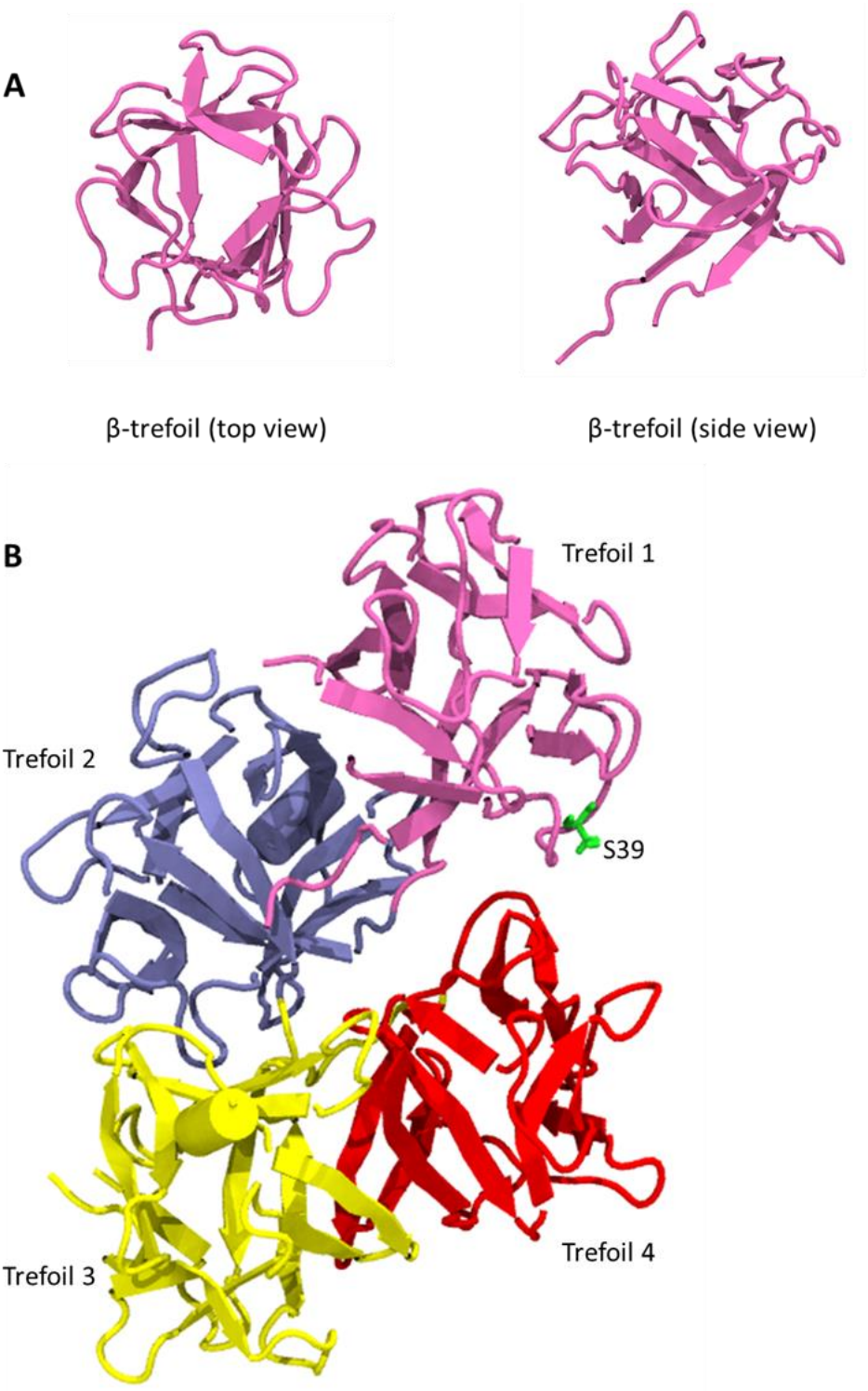


Figure 2.2: (A) A representation of a β-trefoil. The top view exhibits a barrel-like structure formed by the β-sheets. **(B)** Crystal structure of fascin (PDB ID:1DFC[37]) with the regulatory site S39.

Fascin has long been used as a prognostic biomarker for cancer, with high fascin expression in cancerous tissue often correlating with poor survival prognosis[44–48]. This correlation is frequently attributed to fascin's role in the creation and maintenance of traditional filopodia and invadopodia, which assist cancer cells in migration and metastasis[49–51]. These cellular structures are thin, finger-like extensions that probe the cell's environment and are often involved in cell migration[52]. However, some studies have shown that fascin expression positively correlates with migration and invasion in a filopodia-independent manner, suggesting other mechanisms outside its role as an actin-bundling protein[49,53–57].

Despite the extensive study of fascin in the context of cancer, it also has several other known functions. Fascin stabilizes focal adhesions[58], which are sites where the cell anchors itself to the extracellular matrix through stress fibers. Fascin plays two roles at focal adhesion sites: 1) it prevents the severing of stress fiber filaments by cofilin[58] , and 2) it maintains the size of stress fibers[58]. Knockdown of fascin in fibroblasts causes a global change in cytoskeletal structure, significantly thickening stress fibers as compared to normal fibroblasts[58]. Additionally, fascin is implicated in various other cellular processes, including retrograde transport[59], formation of extracellular vesicles[60], and it also acts as a transcription factor when transported to the nucleus[61].

2.3 Fascin in neurons and dendritic spines

In neurons, fascin is abundantly found in growth cones[62]. Neuronal growth cones are motile structures located at the elongating tips of nerve axons. These structures guide

the axon to its target and are critical for the development of the nervous system as they can sense chemotropic cues[62,63].

Fascin is involved in developing filopodia, which are essential for growth cone motility[63]. Since filopodia and dendritic spines are both cell protrusions, it would be expected that fascin is involved in dendritic spines as well. Surprisingly, however, while filopodia are fascin-positive, dendritic spines were reported to be fascin-negative. Korobova and Svitkina reported in 2009 that fascin was not present in dendritic filopodia of young neurons at 10 days *in vitro* (DIV)[64]. Dendritic filopodia are thin, finger-like protrusions extending from a dendrite that can mature into mushroom-shaped dendritic spines[23,65]. Given the absence of fascin in dendritic filopodia of 10 DIV neurons and the predominance of branched actin in these structures[66,67], fascin was presumed to not play a role in the formation, creation, and maintenance of dendritic spines. Consequently, fascin has largely been overlooked in studies of the cytoskeletal dynamics of dendritic spines. However, if BTA-EG_4 and BTA-EG_6 indeed bind to fascin and subsequently affect dendritic spine density, it suggests a previously unrecognized role of fascin in modulating dendritic spines.

Immunofluorescent images of mature rat neurons acquired by a former PhD student in the Yang lab, Dr. Kyle Berg, shows that fascin is present throughout fully mature neurons at 21 DIV, including localization to numerous areas consistent with dendritic spines[68] (Figure 2.3). This indicates that fascin might play a significant role in the structural dynamics of dendritic spines in mature neurons.

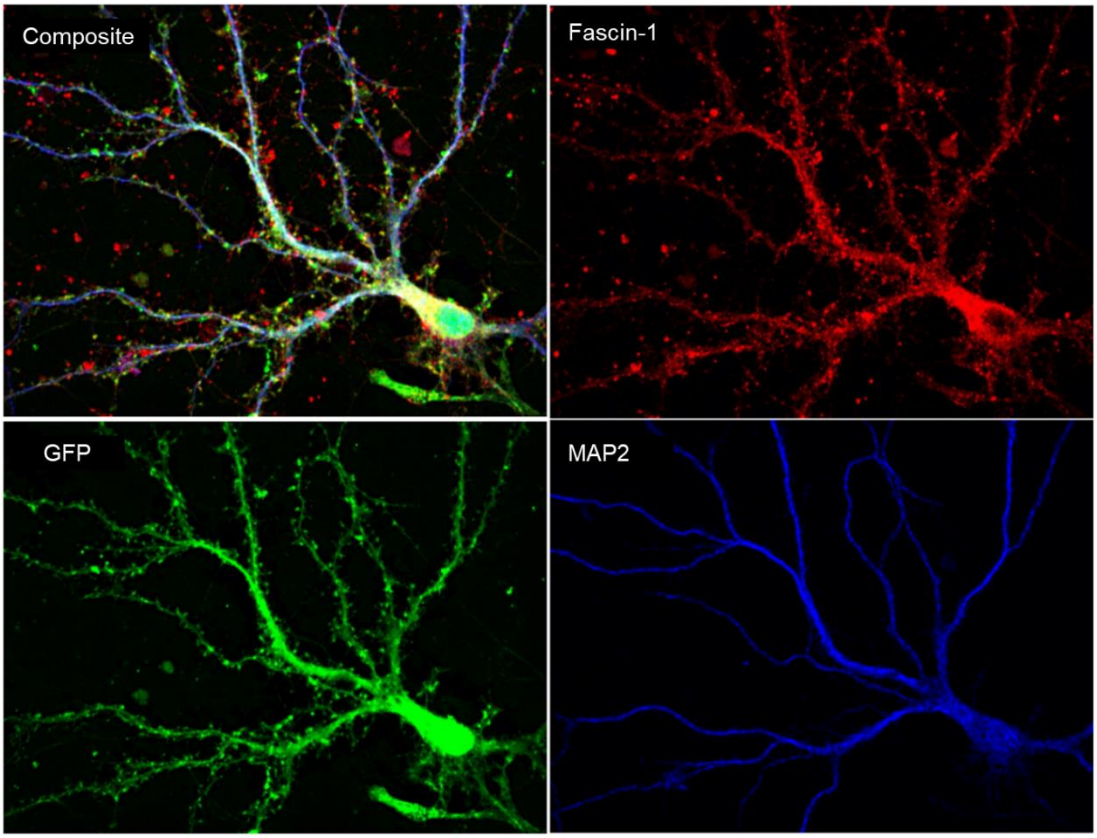


Figure 2.3: Immunofluorescent image of a mature primary rat neuron expressing a filler green fluorescent protein (GFP) stained for a microtubule associated protein used to identify dendrites (MAP2) and stained for fascin (Figure reproduced from Dr. Kyle Berg's dissertation[68]).

2.4 Identification of a method for fascin knockdown in primary rat neurons

To study if fascin is on pathway or is responsible in any way for the increased spine density seen in neurons treated with BTA compounds, I first established a method to knockdown fascin expression in primary neurons.

The method I used in this study involves using a short hairpin RNA (shRNA) to knockdown protein expression in cells. shRNAs reduce target protein levels by utilizing native cellular machinery to cut the messenger RNA (mRNA) of a particular protein

sequence. Further by providing an appropriate double stranded RNA that has a complementary sequence to the target mRNA, the RNA induced silencing complex of the cell can be guided to degrade the mRNA of fascin[69,70]. shRNAs can be delivered via lipofectamine to the nucleus, where they interact with the host DNA and are eventually expressed, producing a shRNA that is processed by the cell. The effects seen with shRNA system are longer lasting due to the constant expression of the shRNA when paired with a strong promoter such as the cytomegalovirus (CMV) promoter[69]. These long-lasting effects are particularly useful when dealing with primary neurons, which generally are studied over a course of 1-3 weeks *in vitro*.

Since our collaborators in the Patrick lab at UCSD provide rat neurons for the experiments discussed here, the knockdown and scramble control vectors were designed and made to be compatible with rat cells. The vector design contained Adeno-associated virus (AAV) as a backbone and also included the expression of a green fluorescent protein (GFP) under the CMV at a separate location of the plasmid as a reporter for positive transfection or transduction. The successful knockdown and scramble control vectors were designed using Vector builder inc.

2.5 Knockdown of fascin expression in PC12 cells

After establishing a mechanism for knockdown, I tested its efficacy in cells. The knockdown vector was first evaluated in PC12 cells, a rodent neuroblastoma cell line that exhibits many neuronal features such as neurite outgrowth and neurotransmitter secretion[71–74]. It was not advisable to test primary neurons initially, as rats must be sacrificed to obtain primary neurons. Moreover, testing in PC12 cells had its advantages

as they divide and grow quickly and can be passaged very easily. PC12 cells were infected with packaged viral particles with different multiplicity of infection (MOI) (or virus to cell ratio), and I found that a MOI of 10 or higher resulted in a high transduction efficiency of approximately 90-95%, as estimated visually by comparing the number of cells expressing the GFP reporter gene to the total number of cells in brightfield (Figure 2.4A). Due to the high transduction efficiency, it was unnecessary to select for infected cells. Next, I assessed fascin expression using a quantitative western blot normalized to a GAPDH control. PC12 cells transduced with the virus at an MOI of 10 showed an average reduction of approximately 65% in fascin expression compared to cells transduced with the scramble control virus (Figure 2.4B and 2.4C).

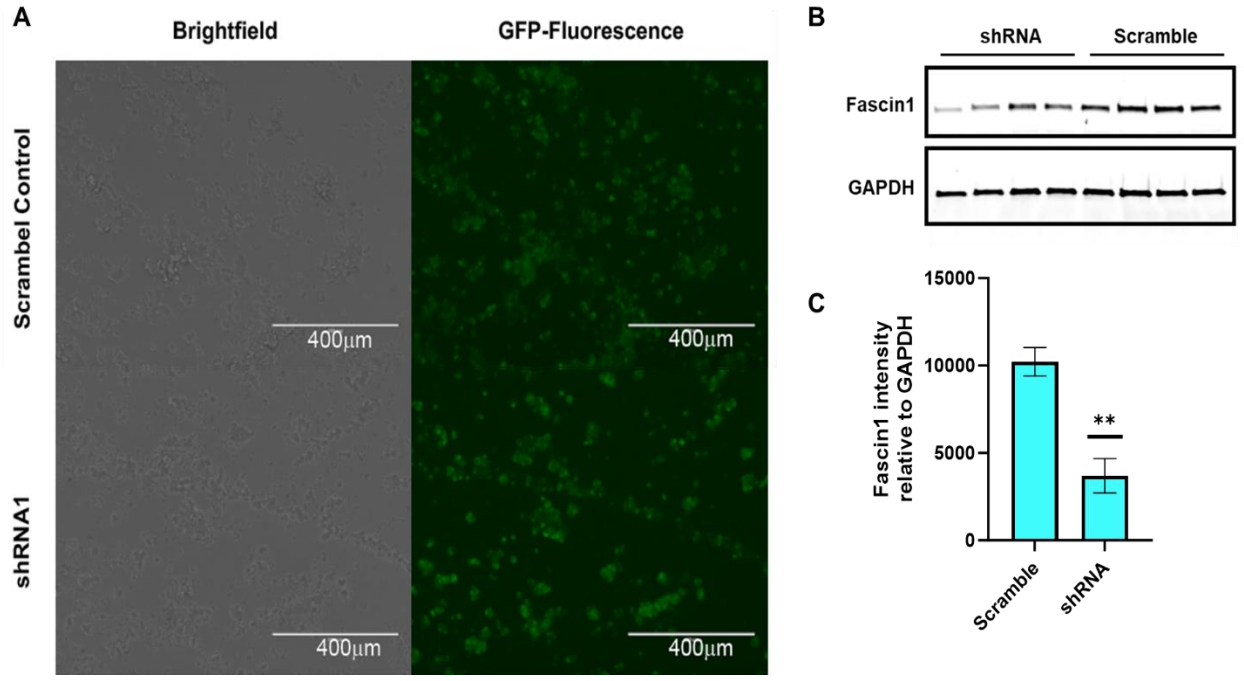


Figure 2.4: Verification of fascin knockdown in PC12 cells. **A)** Overall lentiviral infection levels of shRNA1 and scramble control verified by a GFP reporter gene. **B)** Quantitative western blot of fascin levels compared to a GAPDH Control. **C)** Graphical analysis of the fascin intensities relative to the GAPDH Control. Statistical analysis carried out by student *t*-test (**p-value ≤ 0.01).

2.6 Spine density analysis of primary neurons when fascin is knocked down

This work was done in collaboration with Dr. Lara Dozier from the Patrick lab. Cultured rat hippocampal neurons were transduced with AAV plasmids (with shRNA or scramble) at 7 DIV, then fixed and immunostained for fascin, GFP and MAP2 on 18 DIV. Images were taken with the same laser intensity and the analysis was blinded i.e., all the images were taken by Lara in the Patrick lab while I analyzed the images, unaware as to which images were treatment or control. Not until after the analysis was complete was the identity of each sample treatment revealed**.**

Neurons were analyzed through image analysis[75,76] (Figure 2.5A). Secondary dendritic shafts were selected using the straighten macro[77], then cropped to 30 µm segments. Dendritic spines along the dendritic shaft were measured manually and counted using a spine counting macro developed in the Patrick Lab, which records the length, width, and number of spines. In terms of spine morphology, we found a small but significant increase in the width of spines in cells with fascin knockdown compared to scramble control cells (Figure 2.5B). However, no significant difference in spine length was observed in cells with fascin knockdown compared to scramble control cells (Figure 2.5B). This result corroborated previous results in the Yang lab which showed BTA compounds do not significantly affect spine morphology. We found that fascin knockdown resulted in a significant decrease in spine density compared to cells with endogenous fascin expression levels (Figure 2.5C). This result was in contrast when primary hippocampal neurons were treated with BTA-EG_4 or BTA-EG_6, which led to significant increases in dendritic spine density (Figure 2.5C and 2.5D). We then further probed whether BTA compounds could recover the reduction in spine density seen with fascin

knockdown and found that BTA compounds were unable to increase spine density when fascin is knocked down (Figure 2.5C and 2.5D). This strongly suggests that the binding of BTA compounds to fascin is crucial for the observed increase in dendritic spine density of neurons exposed to these molecules.

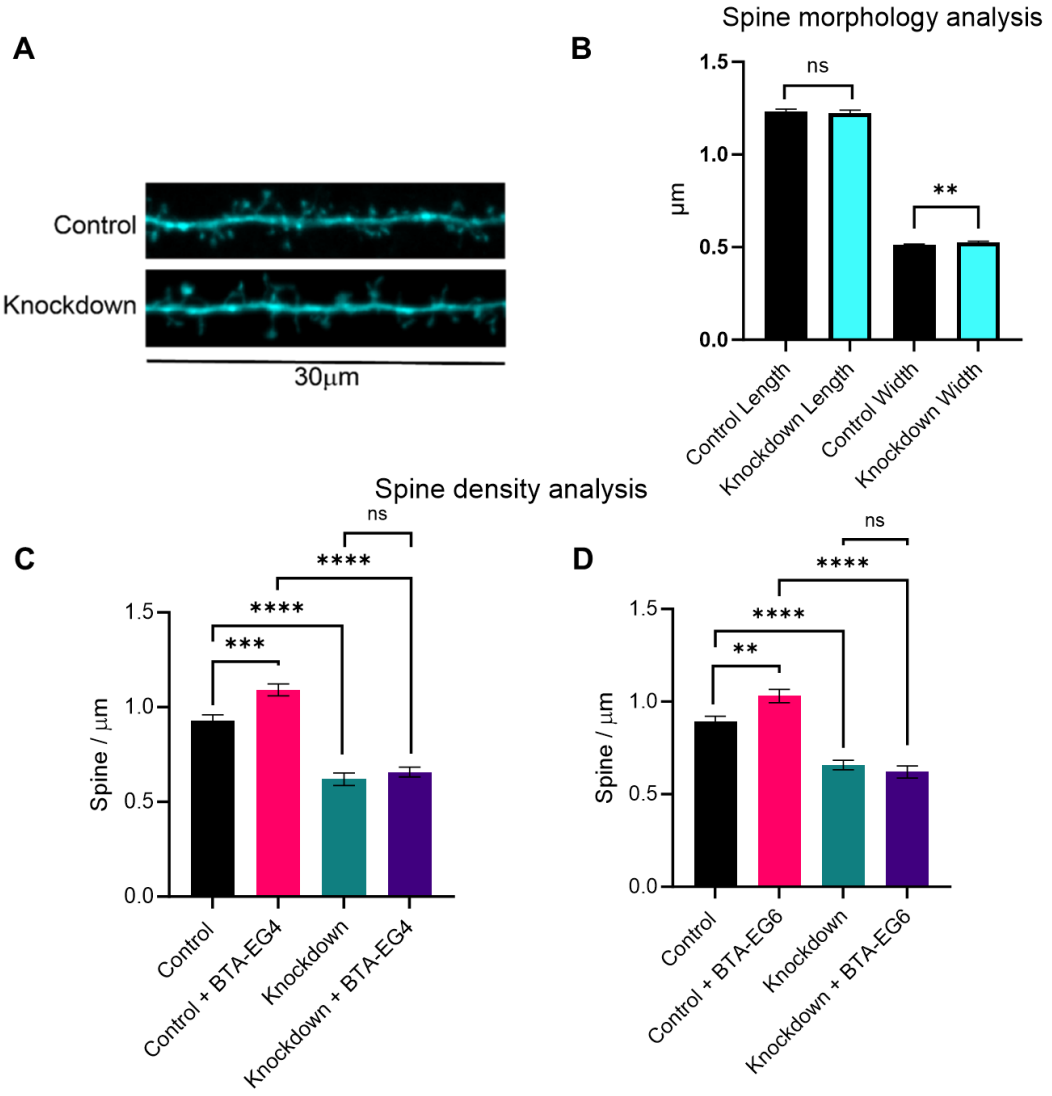


Figure 2.5: Analysis of spine density and morphology measurements upon treatment with plasmids in primary hippocampal neurons**. A)** Representative 30 μm dendritic segments selected for dendritic spine analysis. **B)** Spine morphology analysis of primary neurons after fascin knockdown. **C)** Spine density measurements in primary neurons upon treatment with AAV vectors in the presence of vehicle control (0.1% DMSO) and BTA-EG_4 (5μM). **D)** Spine density measurements in primary neurons upon treatment with AAV vectors in the presence of vehicle control (0.1% DMSO) and BTA-EG_6 (5 μM). Statistical analysis was performed using two tailed Welch's *t*-test (**p<0.1, ***p<0.01, ****p<0.001). *N* = 60 dendritic segments per treatment.

Additional experiments carried out by Dr. Kyle Berg in the Yang lab showed that treatment of primary neurons with BTA-EG_4 or BTA-EG_6 did not significantly alter fascin expression levels[68]. This result suggests that these molecules increase dendritic spine density by directly impacting the dynamic function of endogenous fascin rather than by influencing a proteome-level change in expression.

2.7 BTA compounds increase actin bundling activity of fascin

Results discussed in the above sections and previously reported in the Yang lab show that the treatment of primary neurons with BTA compounds has an opposite effect on spine density as compared to knockdown of fascin, and these molecules do not alter expression levels in primary neurons. Based on these observations, I was interested in exploring how targeting fascin with small molecules could affect spine dynamics without changing expression levels. We postulated that the small molecules could affect the interaction of fascin with other cellular proteins that are involved in spine regulation. Since fascin is primarily a structural protein involved in bundling actin[78], modifying how it binds to actin may lead to the phenotypic changes that we have seen in neurons in the presence of BTA compounds.

To assess the effect of BTA compounds on fascin's ability to bundle actin, I performed a slow speed actin bundling and sedimentation assay[35,79]. In this assay, actin, which is bundled by fascin, forms a gel-like material that can be pelleted upon centrifugation[78]. Unbundled actin remains in the supernatant (Figure 2.6).

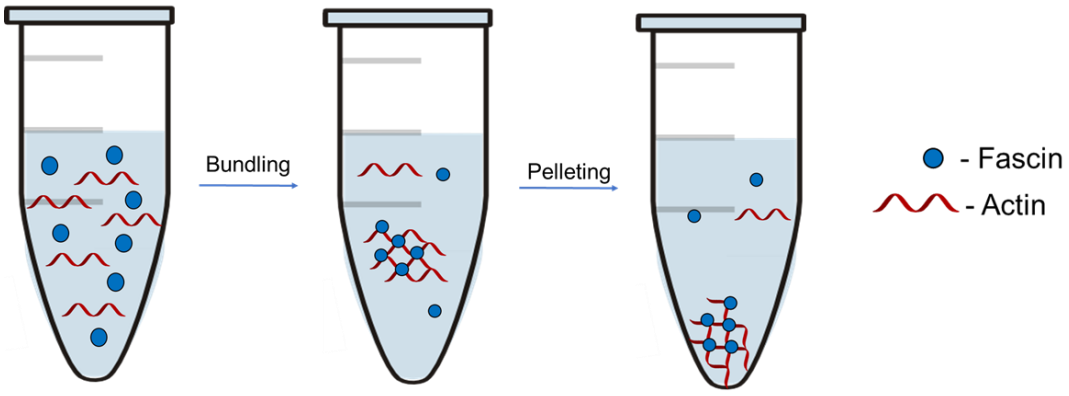


Figure 2.6: Schematic showing the polymerization of actin in the slow speed sedimentation assay. Fascin bundles free F-actin in solution. Once the bundles are formed, the fascin-actin complex can be pelleted by centrifugation.

First, I identified conditions where actin was not the limiting reagent by conducting the assay with a constant 20 µM concentration of actin while varying the fascin concentration. I determined that 0.4 µM fascin was the optimal concentration for significant bundling compared to controls, without saturating the actin in the pellet (Figure 2.7).

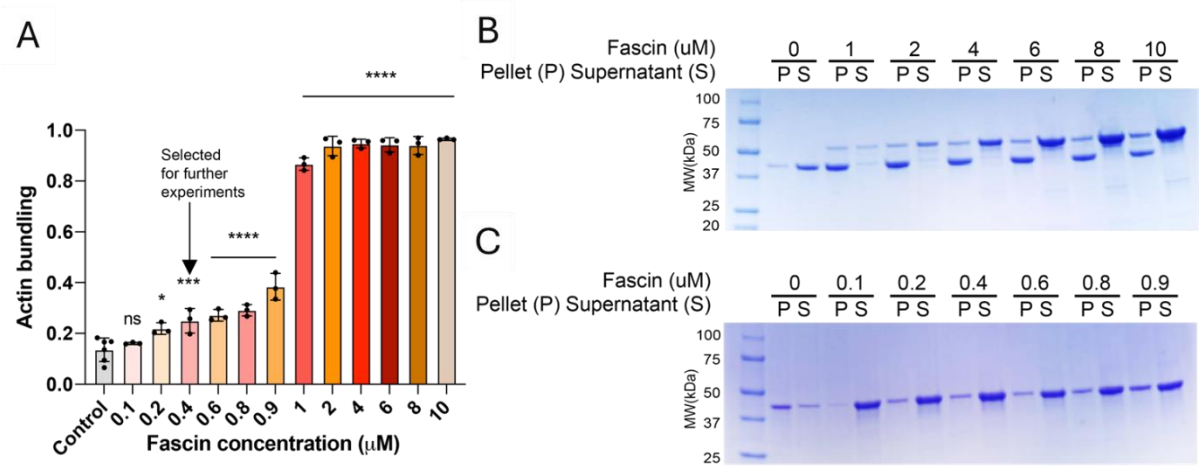


Figure 2.7: Data examining the actin bundling activity of fascin at varying concentrations of fascin. **A)** Graphical representation of the actin bundling activity of fascin at 10 µM actin and varying concentrations of fascin. Statistical analysis done by one-way ANOVA (*p<0.05, ***p<0.001, ****p<0.0001) N=3 for each experiment. **B)** Representative gel of actin bundling by fascin-1 (0-0.9 µM). **C)** Representative gel of actin bundling by fascin (0-10 µM).

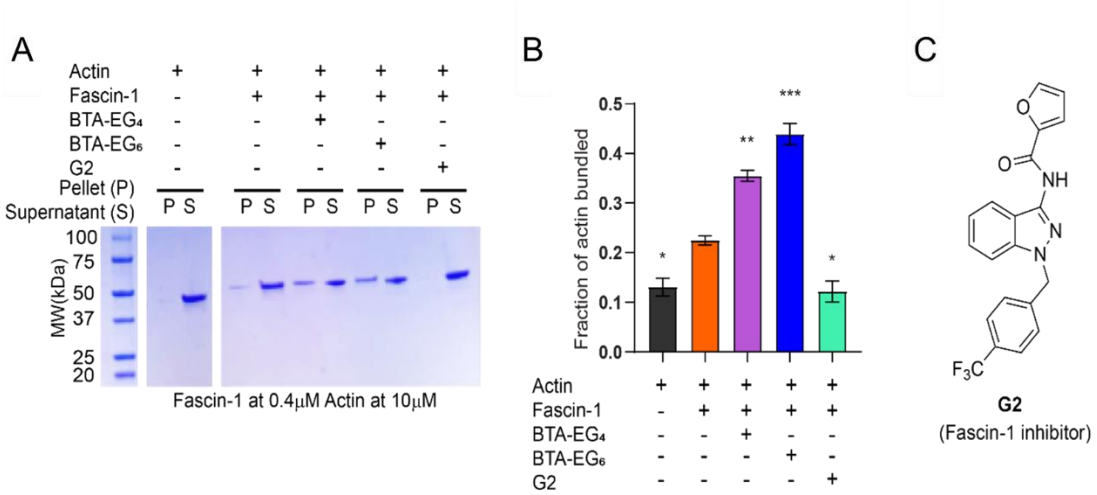


Figure 2.8: Examination of the effects of fascin ligands on the bundling of actin filaments. **A)** Representative gel of actin in bundles (P) versus unbundled (S). **B)** Quantification of the gel in (A) showing the fraction of actin filaments in bundles after various treatments. Statistical analysis was done by two tailed Welch's *t*-test (*p<0.05, **p<0.01, ***p<0.001) for N=3 per condition. **C)** Molecular structure of G2, a known inhibitor of fascin's bundling activity.

The experiment was then repeated with 0.4 μM fascin in the presence of BTA-EG$_4$, BTA-EG$_6$, and G2 (a known inhibitor of fascin's actin bundling activity)[35]. The results showed that actin bundling significantly increased when incubated with BTA-EG$_4$ or BTA-EG$_6$, while actin bundling was eliminated by G2 (Figure 2.8). These results strengthen the evidence that BTA-EG$_4$ and BTA-EG$_6$ enhance the interaction between fascin and actin, leading to increased actin bundling, while G2 effectively inhibits this process.

2.8 Conclusion

In summary, the experiments described in this chapter show that fascin knockdown in primary neurons led to a decrease in dendritic spine density and negated the capability of BTA molecules to promote spine density increases that were seen with endogenous levels of fascin. This is an important result as fascin has largely been disregarded in recent years as playing a role in the context of dendritic spine dynamics.

We also explored how targeting fascin with small molecules could affect spine density without altering expression levels. While there are a few previous reports of molecules that target fascin, all the molecules reported to date inhibit the actin-bundling activity of fascin[80–83]. We found that both BTA-EG_4 and BTA-EG_6 can enhance the actin-bundling activity of fascin.

2.7 Methods

PC12 cell culture

PC12 Cells were maintained in a 37º humidified incubator with 5% CO_2 in Modified Eagle's Medium (Gibco) supplemented with 10% heat inactivated horse serum (Gibco) and 5% FBS (Gibco).

Quantitative western blot

Quantitative western blots were accomplished by normalizing total protein concentration using the Pierce BCA assay and following the manufacturer's protocol. Identical quantities of total protein were loaded onto a 4-20% SDS-PAGE gel (BioRad) and run for 35 minutes at 190V. The protein was then transferred to an activated low fluorescence PVDF membrane (BioRad) using the TransBlot Turbo system (BioRad). Blots were incubated for 1hour at RT in 2% Membrane Blocking Agent (Cytivia) in Tris buffered Saline Solution with 0.1% Tween-20 (v/v) (TBST), followed by overnight incubation with primary antibody (1:10,000 dilution) in 2% Membrane Blocking Agent at 4ºC. The blot was then washed three times for 5 minutes each in TBST at RT. Secondary antibody (1:5000) was added to 2% Membrane Blocking Agent in TBST and allowed to

incubate at RT for 1 hour. The membrane was then washed three times for 5 minutes each in TBST at RT, rinsed in MilliQ water three times and then imaged using the Amersham 680 RGB (Cytivia).

Neuronal cell culture

Dissociated neurons from Sprague Dawley® one day old (P1) male and female rat pups were prepared and maintained as previously described[84–86].

Knockdown of fascin in primary neurons

Cultured rat hippocampal neurons were transduced at 7 DIV with 1µL of AAV virus, either Fascin-shRNA-GFP-AAV (Vector builder ID VB230227-1603ujx) or Scramble-shRNA-GFP-AAV (Vector builder ID VB230505-1423kns), diluted in 1:20 HBSS. After 11 days, neurons were fixed and immunostained for fascin, GFP, and MAP2. For untreated samples, cells were fixed at 19 DIV and immunostained with αGFP (Life Technologies A11122) antibody. For treated cells, 5µL of blinded sample was added to 1mL of conditioned neuronal media 24 hours prior to fixation.

Knockdown of fascin in PC12 cells

Cells were passaged 24 hours prior to infection and plated to be around 70% confluent upon infection. AAV packaged viral particles were added at a MOI of 10. Cells were harvested 3 days after infection using IP lysis buffer (Pierce) and following the manufacturer's protocol and supplemented with C0mplete EDTA free protease (Roche #11836170001) inhibitors following the manufacturer's protocol. Lysates were

normalized to 1 mg/mL total protein and separated via SDS-PAGE and transferred to a PVDF membrane. Fluorescence intensities of fascin normalized to GAPDH were analyzed using Image Studio Lite software (LI-COR).

Dendritic spine density and morphology analysis

Neurons were analyzed in a blinded fashion using ImageJ[87] (NIH). The secondary dendritic shafts were selected using a GFP reporter signal, avoiding any primary dendritic shafts and straightened using an ImageJ straighten algorithm[77], then cropped to 30µm in length. The spines along the shaft were manually analyzed to count the number of spines, and to measure the length and width of each spine as previously reported[27]. Data was collected in Microsoft Excel and statistical analyses were performed using GraphPad Prism.

Immunostaining of primary neurons

Primary neurons were fixed using 4% paraformaldehyde/sucrose solution in phosphate buffered saline solution with magnesium and calcium (PBS-MC) at RT for 10 minutes. Neurons were then permeabilized with 2% BSA and 0.25% Triton X-100 in PBS-MC at RT for 20 minutes, then blocked for 6 hours at 4°C in 5% BSA in PBS-MC. Primary antibodies for anti-fascin (Millipore MAB3582 1:1000), anti-MAP2 (Abcam5392 1:1000 or 1:5000), or anti-GFP (Life Technologies A11122 1:1000) were introduced in 2% BSA in PBS-MC and incubated overnight at 4°C. Secondary antibodies were added 1:1000 for 1 hour at RT, and 1x Hoechst stain (Sigma B2261) was added for the last 10 minutes. Neurons were imaged with a Leica DMI6000 inverted microscope with the following

specifications: A Yokogawa Nikon spinning disk confocal head. Orca ER high resolution black and white cooled CCD camera (6.45 µm/pixel at 1x). Plan Apochromat 63x/1.4 numerical aperture objective. An argon/krypton air-cooled laser for 405nm/140mW, 100mW/561nm, and 140mW/637nm.

Confocal microscopy imaging

PC12 cells were imaged on an EVOS FL (Life technologies) inverted microscope using either the Brightfield or GFP filter. Neurons were imaged with a Leica DMI6000 inverted microscope with the following specifications: A Yokogawa Nipkon spinning disk confocal head. Orca ER high resolution Black and white cooled CCD camera (6.45 um/pixel at 1x). Plan Apochromat 63x/1.4 numerical aperture objective. An argon/krypton air-cooled laser for 405nm/140mW1oomW 561/140mW 637nm lasers.

Slow speed actin sedimentation assay

The actin bundling activity of fascin was measured by a slow-speed centrifugation assay[79]. Monomeric rabbit G-actin (Cytoskeleton, Inc) was induced to polymerize at RT in F-actin buffer (20mM Tris-HCl, pH 8.0, 1mM ATP, 1mM DTT, 2mM $MgCl_2$, and 100mM KCl) to a final concentration of 10µM. Recombinant fascin protein was dissolved in polymerization buffer (2mM Tris, 1mM ATP, 1mM DTT, 2mM $MgCl_2$, 100mM KCl, pH 8.0) to a final concentration of 0.2-20 µM. Small molecules such as BTA-EG_6 or G2 (with 1% DMSO) (Xcessbio Biosciences) were both dissolved in polymerization buffer to a final concentration of 20 µM. Equal volumes of fascin solution were subsequently incubated with F-actin for 60 minutes at RT and centrifuged for 30 minutes at 10,000xg. Both

supernatant and pellet were dissolved in an equivalent volume of SDS sample buffer (Novex) and then run on 4-20% SDS-PAGE. The fraction of actin bundled was measured by quantifying the intensities of actin protein band in pellets compared to total actin.

2.7 Acknowledgments

I would like to acknowledge the constant support I received from Dr. Kyle Berg, Professor Gentry Patrick and Dr. Lara Dozier. Dr. Lara Dozier taught me primary neuronal culture techniques, imaging and spine counting skills. She also maintained and treated the primary neurons that we have used in this study. Dr. Kyle Berg helped me in designing the actin bundling assays and taught me how to work with PC12 cells. The work is in preparation for submission in a research article entitled “Nootropic Benzothiazoles Promote Dendritic Spine Formation by Targeting Fascin-1”.

Chapter 3 : Investigation of BTA binding site on fascin using *in silico* tools and mutagenesis studies

3.1 Introduction

The application of computer-aided methods for predicting ligand-protein interactions and complexes have become increasingly valuable for drug discovery[88]. Molecular docking has significantly advanced our understanding of the behavior of small molecules within the binding sites of target proteins. Molecular docking is frequently used in drug development to model and study biochemical pathways. Generally, the molecular docking process consists of two main steps: predicting the pose of the ligand and assessing the binding affinity[89]. The pose refers to the conformation, position, and orientation of the ligand within the binding site. Knowing the binding site beforehand enhances docking efficiency and guides follow up biochemical assays. The work in this chapter will focus only on BTA-EG_6 due to the poor solubility of BTA-EG_4.

3.2 Molecular docking

As discussed earlier, the crystal structure of fascin is reported by several groups, showing that this monomeric protein contains 4 β-trefoil domains, with domains 1,2 and 3,4 related by a 2-fold pseudo symmetry[38]. The actin binding regions have been identified along β-trefoils 1,2 and 1,4 with a possible third binding region located on β-trefoil 3[79]. Multiple studies have reported that small molecules bind to these sites and affect fascin's functionality[35,38,79].

I used computational tools to explore potential binding sites for BTA ligands on fascin. Using SiteMap[90] tool, I identified two likely binding sites (sites 1 and 2) on the

fascin structure (PDB ID: 1DFC) (Figure 3.1). Next, I conducted molecular docking studies where BTA-EG$_6$ and G2 (a known fascin inhibitor) were individually docked into these identified binding sites, resulting in four separate docking runs. Site 1, situated between β-trefoils 1 and 4, is adjacent to an actin-binding region of fascin and is close to Ser39 in

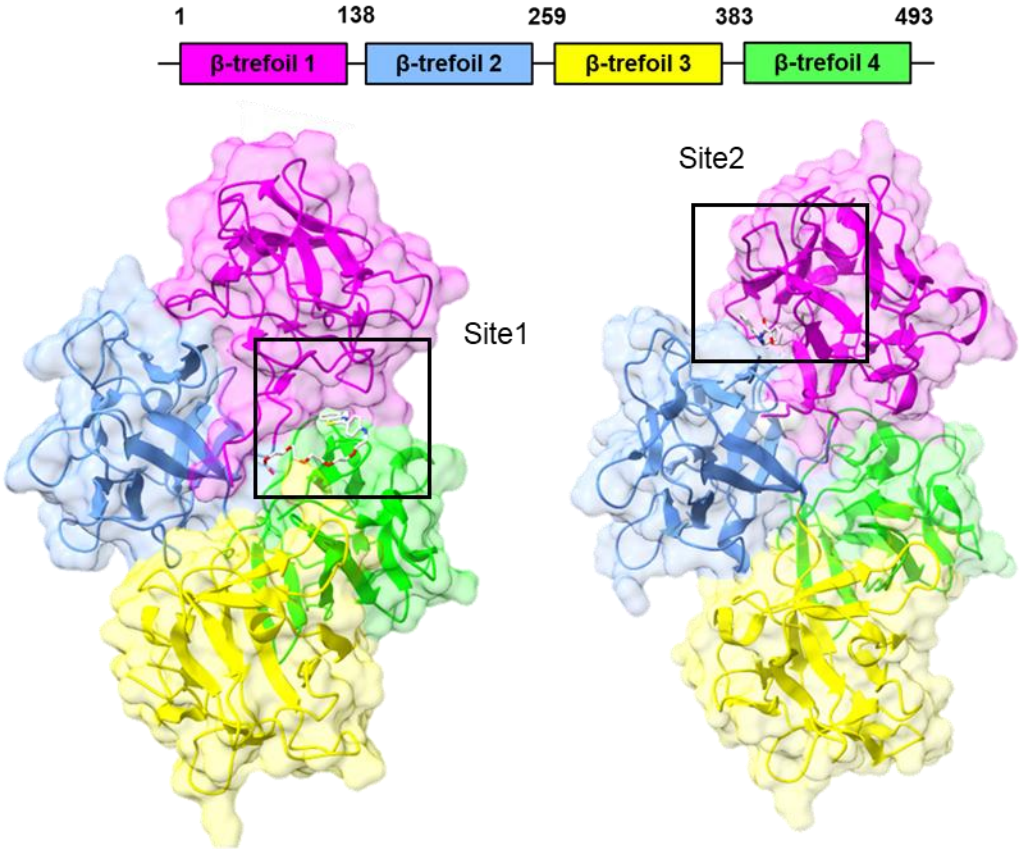


Figure 3.1: Results from SiteMap[90] tool. Two proposed binding sites (sites 1 and 2) on fascin for small molecules were identified (solid rectangle).

β-trefoil 1, a site regulated by phosphorylation[36]. Site 2, located between β-trefoils 1 and 2, has previously been noted as a binding site for G2 analogs[79,81].

In site 1, the top docking poses of BTA-EG$_6$ revealed interactions where the benzothiazole group interacts with hydrophobic residues like A137 and I45 in fascin, with the benzothiazole nitrogen forming a hydrogen bond with R389 (Figure 3.2 and Figure

3.3). Additionally, residue E492 was predicted to engage in multiple hydrogen bond interactions with the ethylene glycol tail of BTA-EG_6. Variations in the conformation of BTA-EG_6's oligo (ethylene glycol) chain were observed among the top poses, which remained flexible and exposed to solvent. For G2 in site 1, top poses indicated interactions where the benzene ring interacts hydrophobically with I45 and forms a hydrogen bond with E492 (Figure 3.2 and Figure 3.4).

Regarding site 2, top docking poses suggested that BTA-EG_6 could potentially establish hydrophobic interactions with residue I93, as well as cation-π and C-H-π interactions with residues R217 and E215, respectively (Figure 3.2 and Figure 3.5). Similarly, for G2 in site 2, top poses indicated hydrophobic interactions with I93. Molecular docking studies also suggested that G2 could form hydrogen bond and cation-π interactions with E215 and R217 in site 2, respectively (Figure 3.2 and Figure 3.6).

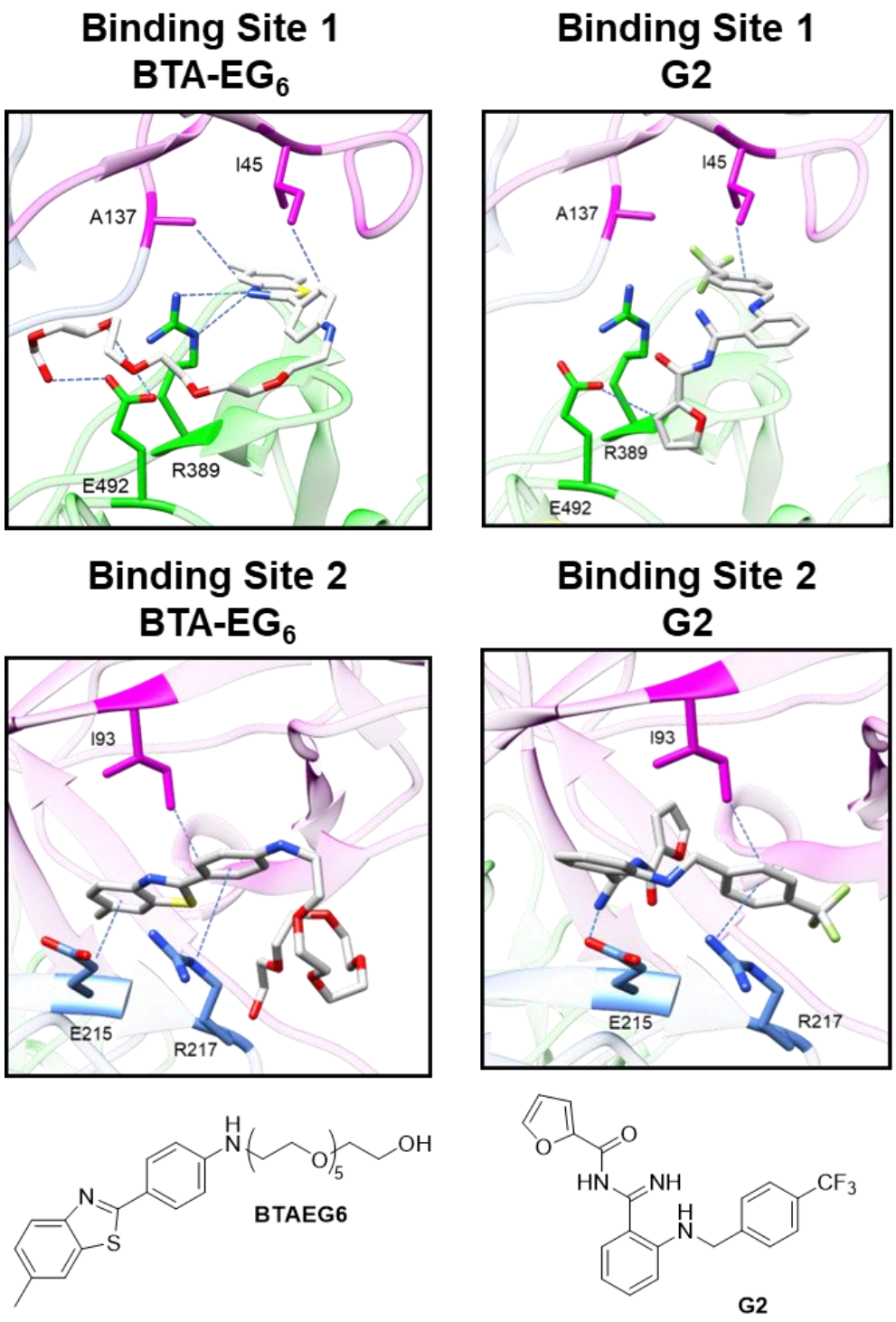


Figure 3.2: Results from molecular docking. Representative top docked poses of BTA-EG_6 and G2 bound to fascin at sites 1 and 2, respectively.

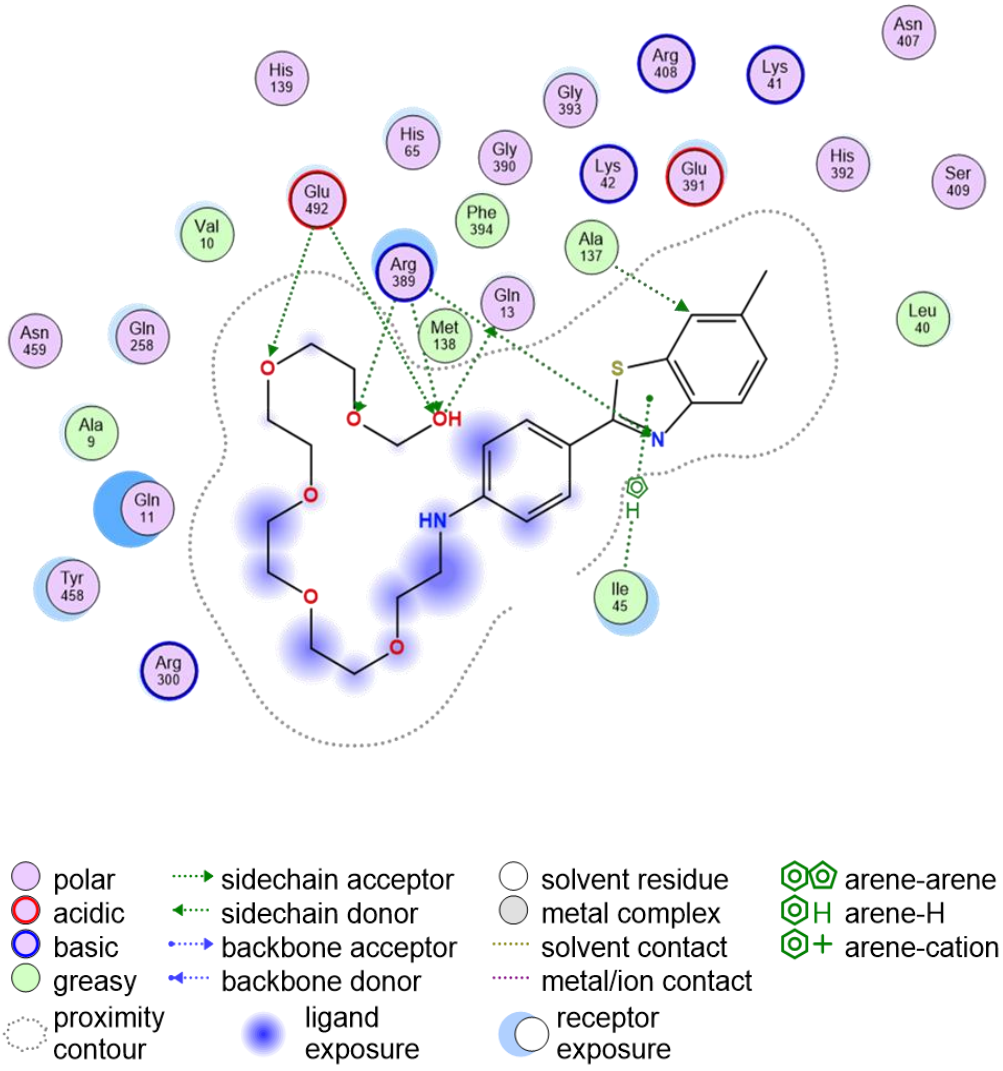


Figure 3.3: 2D interactions map between fascin and BTA-EG$_6$ at binding site 1 between β-trefoils 1 and 4.

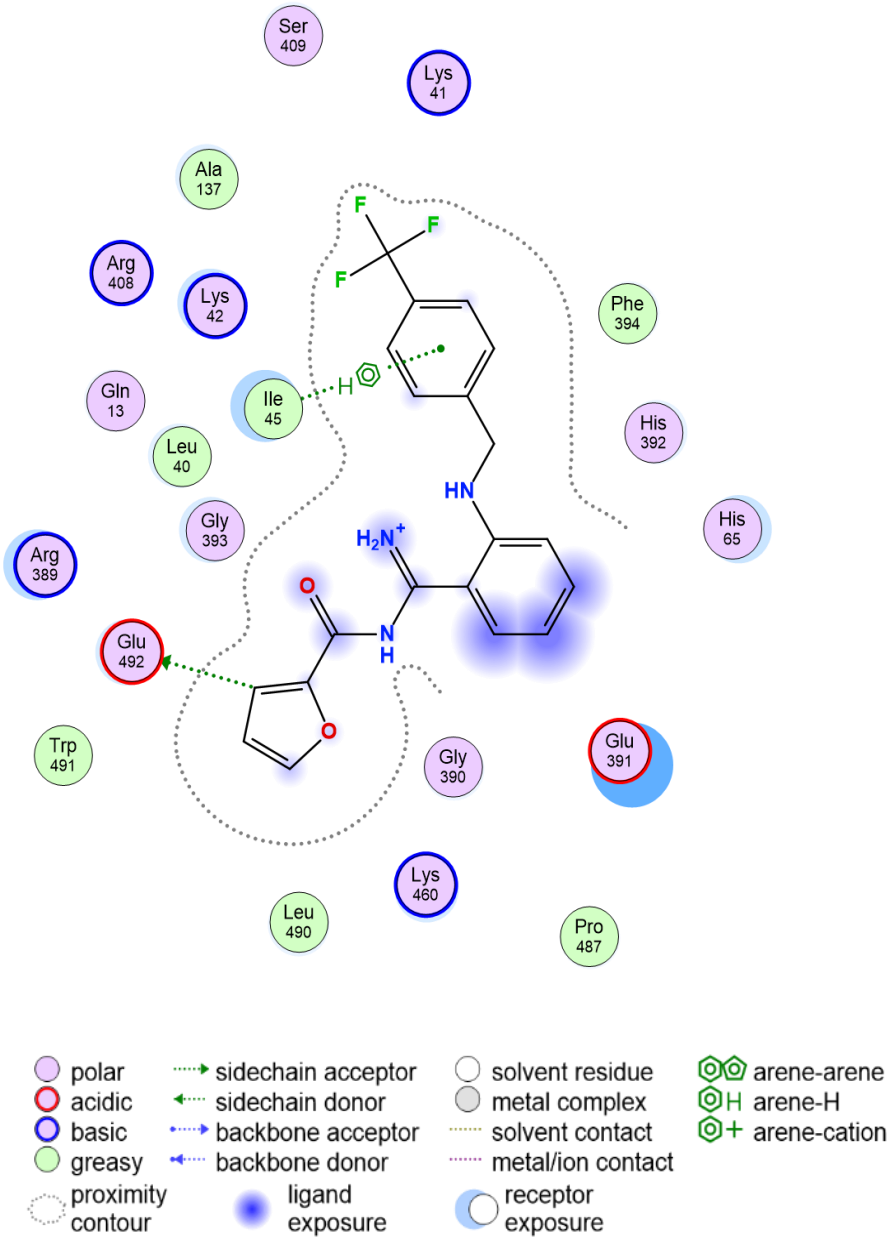


Figure 3.4: 2D interactions map between fascin and G2 at binding site 1 between β-trefoils 1 and 4.

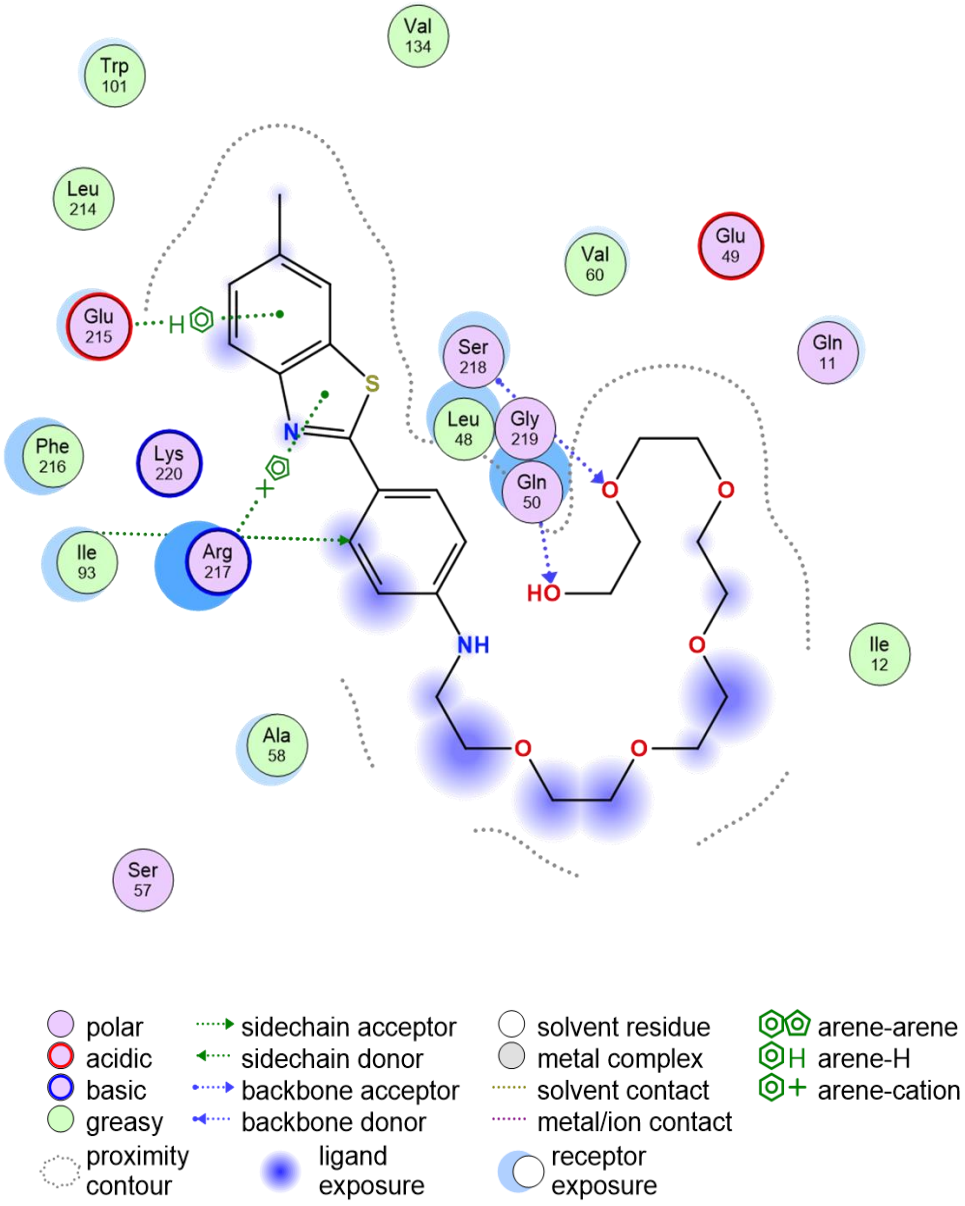


Figure 3.5: 2D interactions map between fascin and BTA-EG$_6$ at binding site 2 between β-trefoils 1 and 2.

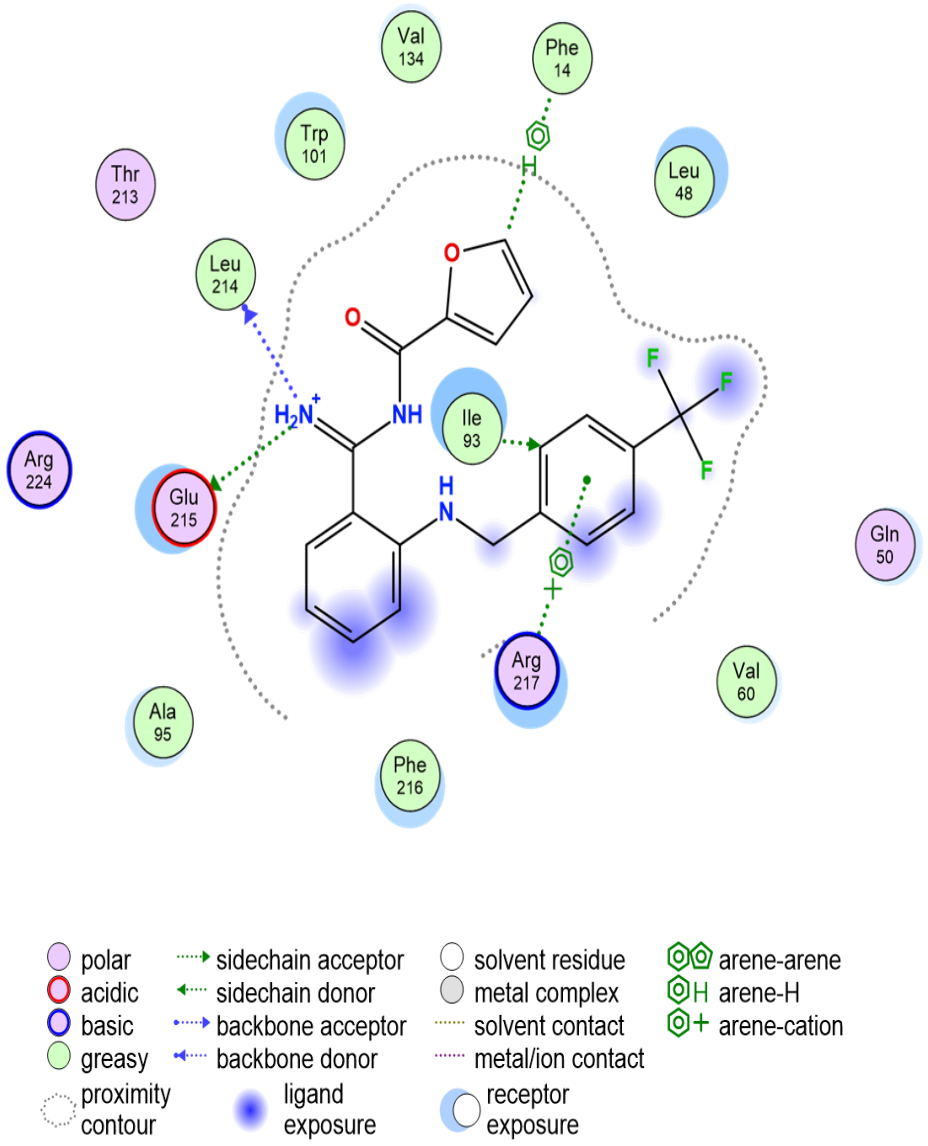


Figure 3.6: 2D interactions map between fascin and G2 at binding site 2 between β-trefoils 1 and 2

3.3 Mutational analysis

Next, to experimentally investigate and validate the binding mode of BTA-EG_6 with fascin, I identified specific residues for point mutations in both the binding sites discussed above. Changes in the binding affinity of the mutant fascin proteins with BTA-EG_6 can provide quantitative evidence to validate the *in silico* model. For this, I selected four residues in site 1 of fascin—A137, I45, E492, and R389—as candidates for site-directed mutagenesis studies based on their proposed involvement in binding to BTA-EG_6. Residues A137 and I45 are hydrophobic residues and are located within the cleft between β-trefoils 1 and 4. Mutations A137K and I45Q were introduced to potentially enhance binding by facilitating hydrogen bond and cation-π interactions between BTA-EG_6 and fascin at site 1. Residue E492 is suggested to participate in hydrogen bond interactions with both BTA-EG_6 and G2 at site 1, while R389 is proposed to be involved in hydrogen bonding interactions with BTA-EG_6. Therefore, fascin mutants E492A and R389A were designed to reduce these interactions and potentially decrease binding.

Similarly at site 2, I targeted three residues—I93, E215 and R217—for site-directed mutagenesis studies. Residue I93 is a hydrophobic residue buried within the cleft between β-trefoils 1 and 2. The mutation I93W was chosen to introduce a bulky group that could potentially disrupt the binding of BTA-EG_6 or G2 to site 2 on fascin. Residue E215 is predicted to form C-H-π and hydrogen bond interactions with BTA-EG_6 and G2, while R217 is predicted to be involved in cation-π interactions with both BTA-EG_6 and G2, respectively, at site 2. Therefore, fascin mutations E215A and R217A were designed to interfere with these interactions and potentially reduce the binding of either of the small molecule ligands to fascin at site 2.

3.4 Biochemical assays

3.4.1 Expression and purification of WT fascin and fascin mutant pr

To experimentally validate the hypotheses generated from our *in silico* molecular docking studies and to determine whether BTA compounds bind to site 1, site 2, or both on fascin, I first generated, recombinantly expressed and purified fascin proteins (both wildtype (WT) and mutant variants). The WT fascin was expressed as a fusion protein having a glutathione S-transferase (GST) tag along with a thrombin cleavage site on the N-terminal. The expression was carried out in *E. coli* under lower temperatures to aid in protein solubility. The pellet was harvested and then purified using an affinity column. The column was filled with glutathione Sepharose beads which have affinity for the GST-fusion protein. After extensive washes, the fusion protein (GST-fascin) could be eluted from the column using higher concentrations of glutathione. Alternatively, GST-fascin was subjected to an on-column cleavage using thrombin overnight.

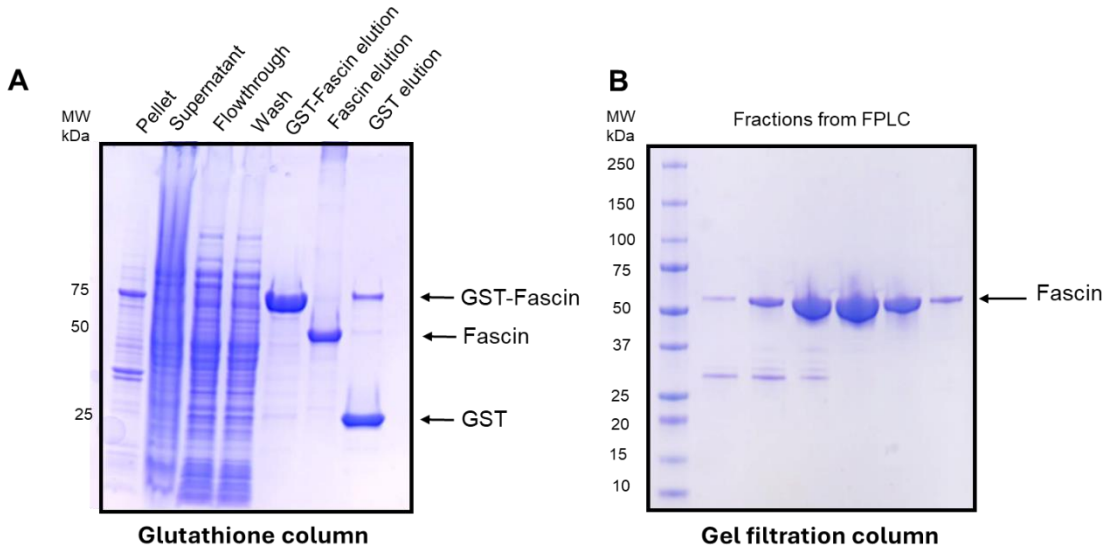


Figure 3.7: Purification of recombinantly expressed fascin fusion protein. **A)** Fractions representing major steps in the GST-fascin purification are shown on an SDS-PAGE and stained using a coomassie blue stain. **B)** Fractions from the gel filtration column containing cleaved fascin protein.

The cleaved fascin (protein of interest) was eluted from the column while the uncleaved GST-fascin and cleaved GST remained on the column still bound to the beads. The column was cleaned, and the remaining proteins still bound to the column (GST and GST-fascin) were eluted by using higher amounts of glutathione. The fractions containing fascin were pooled and concentrated before loading onto a S200 Superdex gel filtration column to remove other minor impurities. The clean fractions of fascin from the gel filtration column were collected and pooled together. Fascin was further concentrated using Amicon centrifugal units for downstream biochemical assays. The purity of the fractions containing fascin protein was assessed by running the protein fractions on an SDS-PAGE and staining with Coomassie Brilliant Blue stain (Figure 3.7). Protein identity was confirmed by western blotting using an anti-fascin antibody.

Once I optimized the expression and purification protocol for WT fascin, I designed primers for single point mutations and carried out site directed mutagenesis to obtain constructs of all 7 fascin mutant proteins I45Q, A137K, R389A, E492A, I93W, E215A and R217A. The identity of all fascin mutant proteins was confirmed by DNA sequencing. Fortunately, all the fascin mutant constructs expressed very similar to that of the WT fascin in *E. coli* and I followed similar purification steps mentioned for WT fascin above with minor modifications.

3.4.2 Circular Dichroism

Once I had purified both WT and mutant fascin proteins, I used Circular Dichroism (CD) to determine whether the expressed, purified proteins were properly folded and to determine if any mutations affected their conformation and stability. CD is a type of optical activity that arises due to the difference in the absorption of left-handed circularly

polarized light (L-CPL) and right-handed circularly polarized light (R-CPL) by a solution containing chiral molecules[91]. CD is commonly used to determine the secondary structure and folding properties of recombinantly expressed proteins[92]. The CD spectra of the proteins were analyzed in the far UV region (wavelengths between 195-260 nm). The spectra for all the proteins showed features typical of a β-sheet structure, which is characteristic of the fascin molecule that consists of 4 β-trefoils. The CD spectra for fascin mutants were similar to those of the WT protein (Figure 3.8), suggesting that the mutations did not adversely affect the proper folding of the proteins.

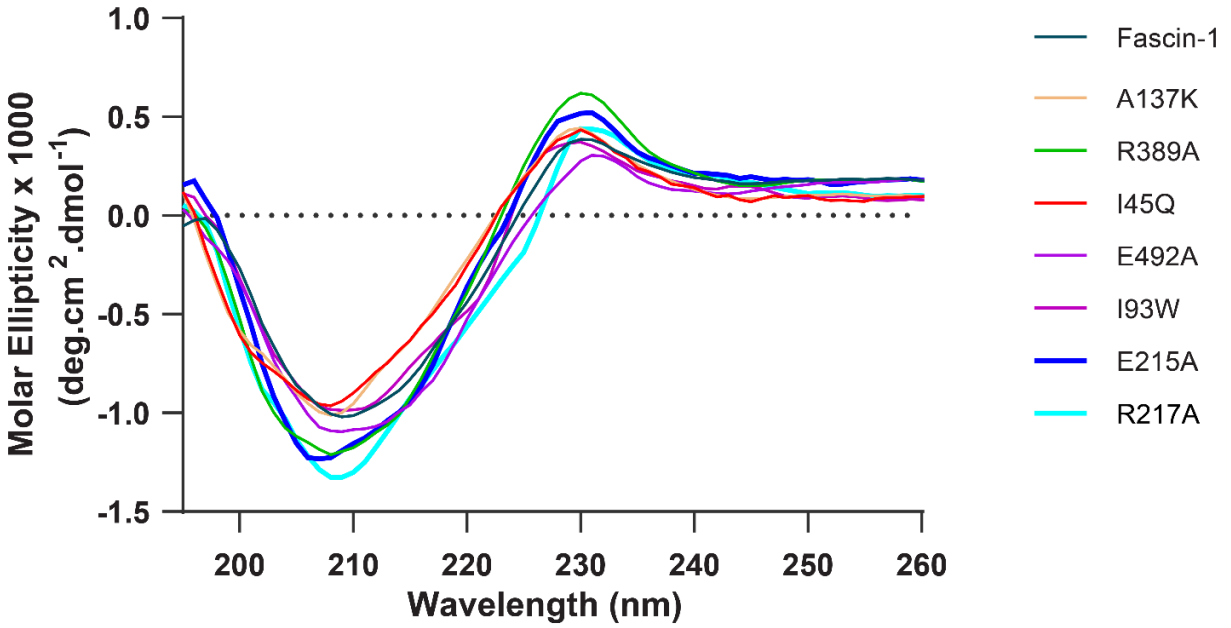


Figure 3.8: CD spectra of recombinantly expressed WT and mutant fascin proteins. The shape of the spectra is consistent with large content of β trefoil structure in fascin. The spectra of all the fascin mutant proteins align well with that of WT fascin with slight shifts.

3.4.3 Actin bundling assay

To test the functionality of WT and mutant fascin proteins, I carried out a slow speed sedimentation assay as previously discussed in Chapter 2[30,35,78]. Recombinant WT

fascin and its mutants were incubated with F-actin. In the absence of fascin, most of the actin was found in the supernatant. However, when actin was incubated with WT fascin or its mutants, the majority of the actin was found in the pellet, indicating successful actin bundling by both WT fascin and its mutant proteins (Figure 3.9).

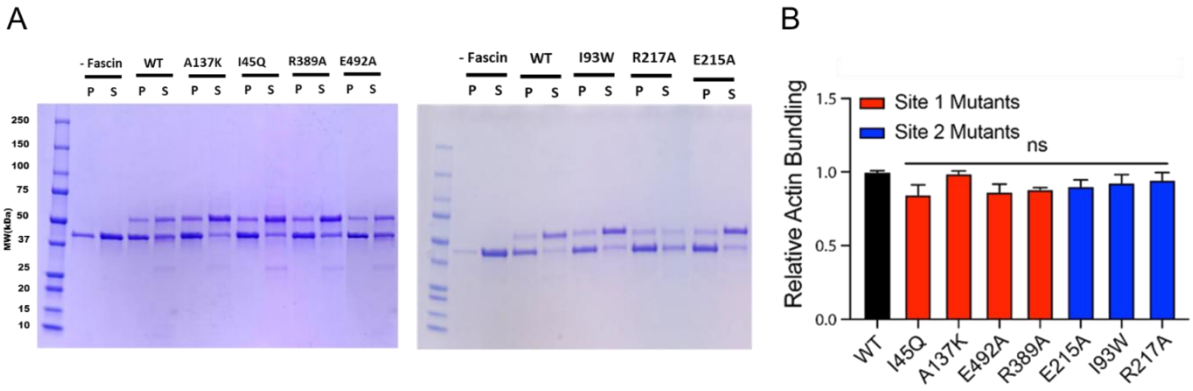


Figure 3.9: Analysis of the actin bundling capability of WT fascin and seven fascin mutant proteins. **A)** Representative SDS-PAGE gel from the actin bundling assay. **B)** Graphical analysis of amount of actin bundled by WT and fascin mutants. Statistical analysis was performed using a two tailed Welch's *t*-test. N=3 for each experiment.

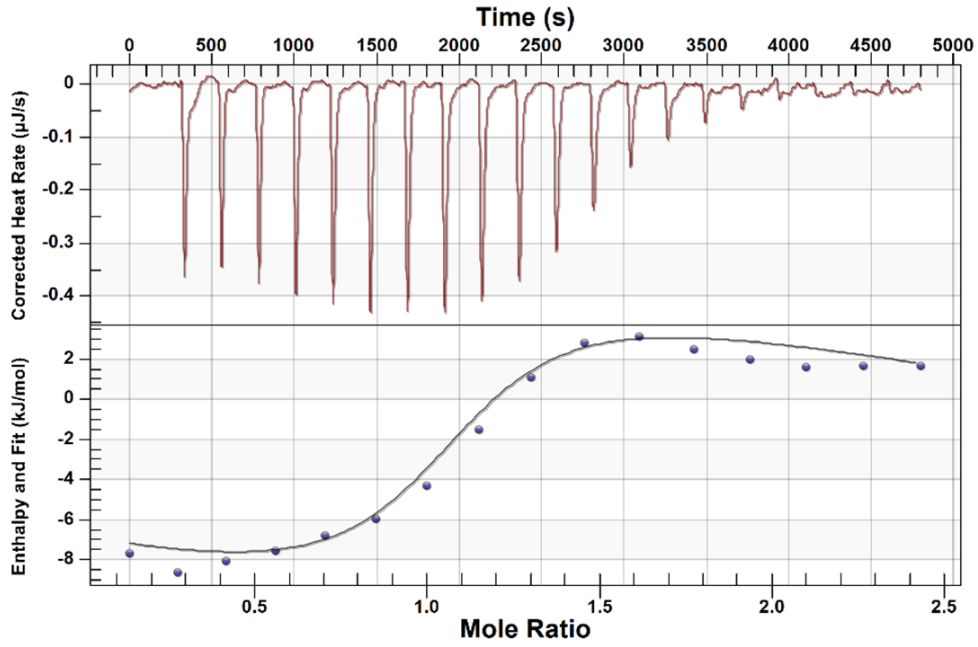
3.3.4 Isothermal Titration Calorimetry studies

Next, I conducted binding studies using isothermal titration calorimetry (ITC) to assess the binding affinity of BTA-EG$_6$ and G2 to WT fascin and mutant fascin proteins. ITC measures the heat generated or absorbed when molecules interact, providing insights into the thermodynamic parameters of such interactions, typically between small molecules and proteins in solution[93]. The ITC data revealed that BTA-EG$_6$ interacts directly with WT fascin having a dissociation constant (K_d) of ~ 5µM and to G2 with a K_d of ~10µM (Figure 3.10).

Consistent with our molecular docking predictions, BTA-EG$_6$ showed enhanced binding affinity to the site 1 fascin mutant proteins A137K and I45Q (Table 3-1 and Figure 3.11), while binding affinity was reduced for the site 1 fascin mutant proteins R389A and

E492A compared to WT fascin (Table 3-1 and Figure 3.11). In contrast, none of the site 1 mutations on fascin significantly affected the binding affinity of G2 compared to WT fascin (Table 3-2 and Figure 3.11). For site 2, we found that none of the mutations on fascin significantly altered the binding of BTA-EG_6 compared to WT fascin (Table 3-3 and Figure 3.11). However, all site 2 mutations on fascin diminished the binding of G2 compared to WT fascin (Tabel 3-4 and Figure 3.11).

A



B

Protein	Molecule	Kd (µM)	ΔH (kJ/mol)	ΔS(J/mol·K)	ΔG(kJ/mol)
WT Fascin-1	BTA-EG_6	4.86 ± 0.70	-20.9 ± 1.7	31.8 ± 7.2	-30.4 ± 3.9
WT Fascin-1	G2	9.29 ± 0.70	-24.9 ± 1.37	-28.8 ± 4.20	-16.3 ± 2.6

Figure 3.10: A) Representative binding isotherm from the titration of fascin with BTA-EG_6. **B)** Results from ITC measurements of BTA-EG_6 (1mM) and G2 (1mM) with WT fascin (100 µM). The experiments were carried out at 25˚C. The data represents measurements after subtraction of background (compound injected into buffer in the absence of fascin protein). N=3 for each experiment.

Table 3-1: Results from ITC measurements of site 1 fascin mutant proteins (100 μM) and BTA-EG_6 (1 mM). The experiments were carried out at 25˚C. The data represents measurements after subtraction of background (compound injected into buffer in the absence of fascin protein). N=3 for each experiment

	Mutant	Binding Affinity	Kd (μM)	ΔH (kJ/mol)	ΔS(J/mol·K)	ΔG(kJ/mol)
	WT Fascin-1	-	4.86 ± 0.70	-20.9 ± 1.7	31.8 ± 7.2	-30.4 ± 3.9
Site 1	I45Q	Increase	0.30 ± 0.07	-5.6 ± 1.0	107.0 ± 5.4	-37.5 ± 2.6
	A137K	Increase	0.75 ± 0.03	-11.6 ± 0.2	78.5 ± 1.2	-35.0 ± 0.6
	E492A	Decrease	17.50 ± 2.73	-45.7 ± 2.3	-61.9 ± 6.4	-27.3 ± 4.2
	R389A	Decrease	15.30. ± 2.51	-39.3 ± 2.9	-38.5 ± 8.7	-27.8 ± 5.5

Table 3-2: Results from ITC measurements of site 1 fascin mutant proteins (100 μM) and G2 (1 mM). The experiments were carried out at 25˚C. The data represents measurements after subtraction of background (compound injected into buffer in the absence of fascin protein). N=3 for each experiment.

	Mutant	Binding Affinity	Kd (μM)	ΔH (kJ/mol)	ΔS(J/mol·K)	ΔG(kJ/mol)
	WT Fascin-1	-	9.29 ± 0.70	-24.9 ± 1.37	-28.8 ± 4.20	-16.3 ± 2.6
Site 1	I45Q	No Change	7.56 ± 0.14	-25.8 ± 2.55	-23.5 ± 6.47	-18.7 ± 4.4
	A137K	No Change	7.84 ± 0.30	-23.9 ± 1.52	-21.4 ± 4.33	-17.5 ± 2.8
	E492A	No Change	6.40 ± 2.23	-27.4 ± 1.00	-25.4 ± 3.30	-19.8 ± 1.9
	R389A	No Change	7.91 ± 1.81	-24.3 ± 1.75	-23.0 ± 7.07	-17.4 ± 3.8

Table 3-3: Results from ITC measurements of site 2 fascin mutant proteins (100 μM) and BTA-EG_6 (1 mM). The experiments were carried out at 25˚C. The data represents measurements after subtraction of background (compound injected into buffer in the absence of fascin protein). N=3 for each experiment.

	Mutant	Binding Affinity	Kd (μM)	ΔH (kJ/mol)	ΔS(J/mol·K)	ΔG(kJ/mol)
	WT Fascin-1	-	4.86 ± 0.70	-20.9 ± 1.7	31.8 ± 7.2	-30.4 ± 3.9
Site 2	E215A	No Change	3.40 ± 0.58	-18.9 ± 1.5	41.4 ± 4.3	-31.2 ± 2.8
	I93W	No Change	4.41 ± 1.12	-20.8 ± 2.6	33.5 ± 10.5	-30.8 ± 5.7
	R217A	No Change	3.53 ± 0.48	-27.3 ± 1.8	13.0 ± 7.1	-31.2 ± 3.9

Table 3-4: Results from ITC measurements of site 2 fascin mutant proteins (100 μM) and G2 (1 mM). The experiments were carried out at 25˚C. The data represents measurements after subtraction of background (compound injected into buffer in the absence of fascin protein). N=3 for each experiment.

	Mutant	Binding Affinity	Kd (μM)	ΔH (kJ/mol)	ΔS(J/mol·K)	ΔG(kJ/mol)
	WT Fascin-1	-	9.29 ± 0.70	-24.9 ± 1.37	-28.8 ± 4.20	-16.3 ± 2.6
Site 2	E215A	Decrease	15.40 ± 1.22	-18.3 ± 2.92	-15.5 ± 8.67	-13.8 ± 5.5
	I93W	Decrease	34.76 ± 0.98	-10.7 ± 3.44	-11.5 ± 4.23	-7.2 ± 4.7
	R217A	Decrease	23.73 ± 1.18	-14.7 ± 2.29	-16.9 ± 6.40	-9.6 ± 4.1

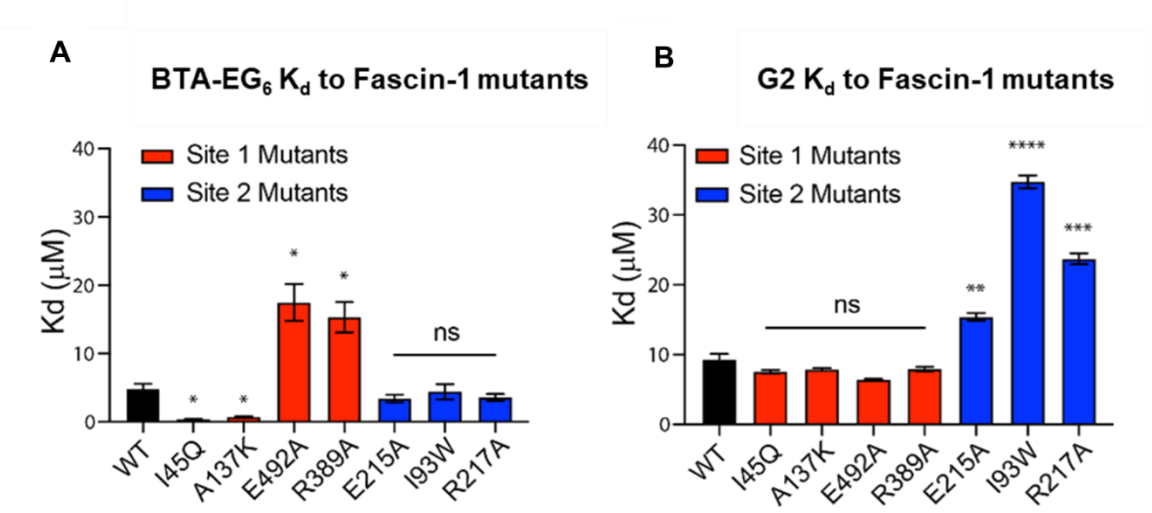


Figure 3.11: Graphical representation of binding affinities of site 1 and site 2 fascin mutants to **A)** BTA-EG$_6$ and **B)** G2. Statistical analysis was performed using a two tailed Welch's *t*-test (*p<0.05, **p<0.01, ***p<0.001, ****p<0.0001). N=3 for each experiment

Overall, these binding studies with the seven fascin mutant proteins strongly support the hypothesis that BTA compounds bind predominantly to site 1 on fascin, while G2 binds to site 2.

3.5 Conclusion

In this chapter, I was able to use molecular docking studies followed by site directed mutagenesis studies to propose a possible binding site of BTA-EG_6 on fascin. The binding studies with various fascin mutant proteins support the hypothesis that BTA molecules may be binding to site 1 on fascin while G2 is likely binding to site 2. The latter observation corroborates existing data that G2 analogs have been reported to bind to site 2 of fascin[79]. This distinction likely contributes to their opposing effects on fascin-mediated actin filament bundling, with BTA compounds enhancing the acting bundling activity, while G2 inhibiting the actin bundling activity, providing mechanistic insights into how these compounds interact with fascin and influence cellular functions.

3.6 Methods

Expression and purification of WT fascin

Fascin was grown by transforming the fascin pGEX-5X-2 plasmid into DE3-BL21 cells (NEB) following the manufacturer's instructions. Cells were plated on selection agar plates containing 100 µg/mL ampicillin. A colony was selected for growth overnight in 50 mL LB broth with 100 µg/mL ampicillin with shaking at 220 RPM and 37ºC. The culture was then transferred to a 1L culture containing YT broth (pre-warmed to 37ºC) and 100 µg/mL ampicillin. The culture was allowed to grow to an OD of 0.8-1.0 at which point the temperature was reduced to 17ºC and the culture was induced with 0.5mM IPTG. The culture was allowed to incubate overnight, and the bacteria were harvested by centrifugation at 3000xg for 30 minutes and frozen at -80ºC. Cells were lysed by sonicating on ice in resuspension buffer (20mM Tris-HCl pH 8.0, 150mM NaCl). The

lysate was centrifuged at 18,000xg for 30 minutes to remove the cell debris. The supernatant was then incubated for at least 2 hours with 5mL of glutathione Sepharose beads (Sigma #17075605) per liter culture at 4°C. After extensive washing with resuspension buffer, the beads were resuspended in thrombin cleavage buffer (20 mM Tris-HCl, pH 8.0, 150 mM NaCl, 2mM $CaCl_2$, 1mM DTT). Fascin was released from the beads by incubation overnight with 40–100U of thrombin at 4°C per liter culture. After elution, 0.2mM phenylmethylsulphonyl fluoride was added to inactivate the remnant thrombin activity. The fascin protein was further purified by loading onto a Superdex S200 size exclusion column. The clean fractions were collected and concentrated with Amicon 30 MWCO protein concentrator (Millipore) to greater than 10 mg/mL. The purity of recombinant fascin proteins was determined by SDS-PAGE and the identity was confirmed by western blot using anti-fascin antibody (MAB3582).

Site directed mutagenesis of fascin

Q5®Site-directed mutagenesis kit (New England BioLabs) was used to introduce point mutations in fascin. Both forward and reverse primers for specific mutations were designed and PCR was carried out using standard conditions as per manufacturer's specifications. The identity was confirmed by DNA sequencing.

Expression and purification of fascin mutants

The same protocol for expression and purification as that for WT fascin was followed. Protein purity was assessed visually by SDS-PAGE and protein identity was confirmed by western blot using an anti-fascin antibody (MAB3582).

Circular Dichroism (CD)

CD spectra of WT and fascin mutant proteins were collected in the range of 195-300 nm using a Jasco J-810 spectropolarimeter. All samples were prepared in Tris buffer (2mM Tris, pH 7.4, 1mM DTT, 2mM $MgCl_2$) and the experiments were performed at 25°C. The CD spectra were normalized with respect to protein concentration (0.5µM) and the pathlength of the cuvette used (0.1 cm).

Molar ellipticity was calculated using the following formula and averaged across 3 scans:

[θ](molar ellipticity)= MW × 100 ×θ / c × d (deg· cm^{2}·$dmol^{-1}$)(c in mg/ml; d in cm)

[θ](mean residue ellipticity)=MRW × θ / 10c × d (deg.cm^{2}.$dmol^{-1}$)

MRW (mean residue weight) = M/(N-1) (approx.110 ± 5 Da)

Slow speed actin sedimentation assay

F-actin bundling activity by fascin was measured by a slow-speed centrifugation assay as described previously in Chapter 2 of this dissertation.

Isothermal Titration Calorimetry

Calorimetric measurements were carried out using a Low Volume ITC instrument (TA Instruments). The ligand (BTA-EG_6 or G2) was titrated to the protein solution (fascin or fascin mutant proteins) present in the 350µL sample cell. All measurements were carried out at 25°C. The protein was dialyzed in 50mM HEPES buffer (pH 7.5), 150mM NaCl to a concentration of 100µM. The ligand solution contained 1mM of the small molecule (BTA-EG_6 or G2) dissolved in the same buffer as the protein. Data was analyzed using the NanoAnalyze software (TA Instruments) for fitting points to the independent

binding model. Experimental heats of the protein-small molecule titration were corrected for heats of dilution of the ligands into buffer alone.

Computational docking studies

All steps for the docking experiments were carried out using Schrodinger suite 2019-20. The crystallographic structure of fascin was retrieved from RCSB Protein Data Bank, PDB ID: 1DFC[37]. The protein was prepared using Maestro's Protein Preparation Wizard[94]. The SiteMap tool[90] was used to identify two ligand binding pockets on fascin. The receptor grids were then generated at the center of mass of the pocket residues and were made large enough to contain the binding site of the protein and the surrounding surface regions. Site 1 included residues 22, 27, 29, 39, 41, 68, 398, 408, 471, 488; and site 2 included residues 11, 14, 16, 48, 49, 50, 58, 60, 62, 93, 95, 101, 103, 134, 213, 214, 215, 216, 217, 218, 219. Ligands were constructed in Maestro[94] and LigPrep[95] was used to prepare the ligand for molecular docking. Each generated ligand was docked into both binding sites using Glide[96] with extra precision docking and default parameters to generate 100 poses for the ligand-receptor complex. The poses were clustered together using a cutoff RMSD value of 2 Å. The ligand interaction tool of the Molecular Operating Environment (MOE) software[97] was used to study the expected interactions between ligand and protein residues in the binding sites. All the docked pose images were generated using Chimera[98] and 2D interactions maps were obtained from MOE.

3.7 Acknowledgements

I would like to acknowledge the support from Dr. Zied Gaieb, Dr. Christian Seitz and Professor Rommie Amaro for providing me the resources and teaching me all the *in silico* methods for my work. I would like to thank Dr. Kyle Berg for his help in training me on recombinant protein expression and purification methodology and for his general advice with data analysis. I would like to thank Dr. Geoffray Leriche for his assistance in carrying out the initial binding studies using ITC. The work is in preparation for submission in a research article entitled “Nootropic Benzothiazoles Promote Dendritic Spine Formation by Targeting Fascin-1”.

Chapter 4 : Structural studies of fascin and BTA-EG_6 to identify key residues in their binding complex

4.1 Introduction

The development of a compound that enhances memory and learning in mice, potentially addressing symptoms of neurodegenerative diseases, represents a significant scientific and medical advancement. Understanding the precise interaction between a compound and its specific protein target can provide insights into its mechanism of action[99]. This knowledge is crucial for developing new compounds with higher binding affinity, which could serve as improved candidates for clinical trials[99]. This chapter focuses on gathering direct evidence for critical residues involved in the binding of BTA-EG_6 to fascin by techniques such as protein crystallography and protein NMR. By correlating structural data with functional assays and computational models, this study will contribute significantly to the field of drug discovery and development, particularly in the context of understanding protein-ligand interactions that are crucial for neuronal function and plasticity.

4.2 Previous work in the Yang lab

Previously in Yang lab, Dr. Kevin Sibucao carried out photoaffinity labeling studies to identify fascin as the target of BTA molecules[29]. In the previous chapter, I have confirmed and quantified the binding affinity of BTA-EG_6 to fascin by ITC to be ~5μM. I have also identified a potential novel binding pocket for BTA ligands on fascin which may influence the type of activity that is observed upon binding of BTA compounds to fascin. In collaboration with Dr. Kyle Berg from the Yang lab, I build on these findings to provide additional structural evidence as to the binding pocket of BTA-EG_6 with fascin.

4.3 X-ray crystallography of fascin and BTA-EG$_6$

The first method attempted for this analysis was X-ray crystallography which relies on the diffraction of an X-ray beam to reveal the 3-D structure of the electron clouds within the crystal lattice[100]. X-ray crystallography provides a high atomic resolution of protein structure and is generally not limited by protein size and can reveal direct interactions between protein and ligand[101]. This allows us to visualize the spatial arrangement of a ligand within the binding site at an atomic resolution[102]. Some limitations of X-ray crystallography are that a single crystal must be achieved with a single lattice. It also provides a more static snapshot rather than dynamic information[103]. In some cases, the conditions used to induce crystal formation may not accurately mimic the native conditions of the protein[104,105].

Since crystallization conditions for fascin are already published[38,79,81,106], Dr. Kyle Berg was able to obtain a high-resolution 2.1Å structure of fascin[68]. Unfortunately, despite many efforts, when attempting to crystallize fascin in the presence of BTA-EG$_6$, he was not able to yield clear electron density for the compound.

To further this study, I attempted the soaking method to get a co-crystal of fascin and BTA-EG$_6$. This technique introduces small molecules or ligands to the already formed protein crystals for structural analysis[107,108]. The apo structure was first grown using a hanging drop method[109] based on conditions previously established in literature and by Dr. Kyle Berg in the Yang lab. Fascin was concentrated to approximately 14 mg/mL in a protein buffer containing 20 mM Tris, 40 mM KBr, and 0.5 M EDTA at pH 8.0. The best-quality crystals were observed in conditions containing 18% PEG 4000, 100 mM HEPES pH 8.0, 3% isopropanol, and 1 mM DTT. Once crystals were obtained, they were

transferred into a solution containing BTA-EG$_6$ and included cryoprotectants like glycerol and PEG 4000 to prevent ice formation during flash freezing. The crystals were left to incubate allowing ligand molecules to diffuse into the crystal lattice and bind to the protein followed by flash freezing using liquid nitrogen. The crystals were then subjected to X-ray diffraction to determine the atomic structure. Unfortunately, I still could not see the presence of BTA-EG$_6$ in the crystal lattice (Figure 4.1).

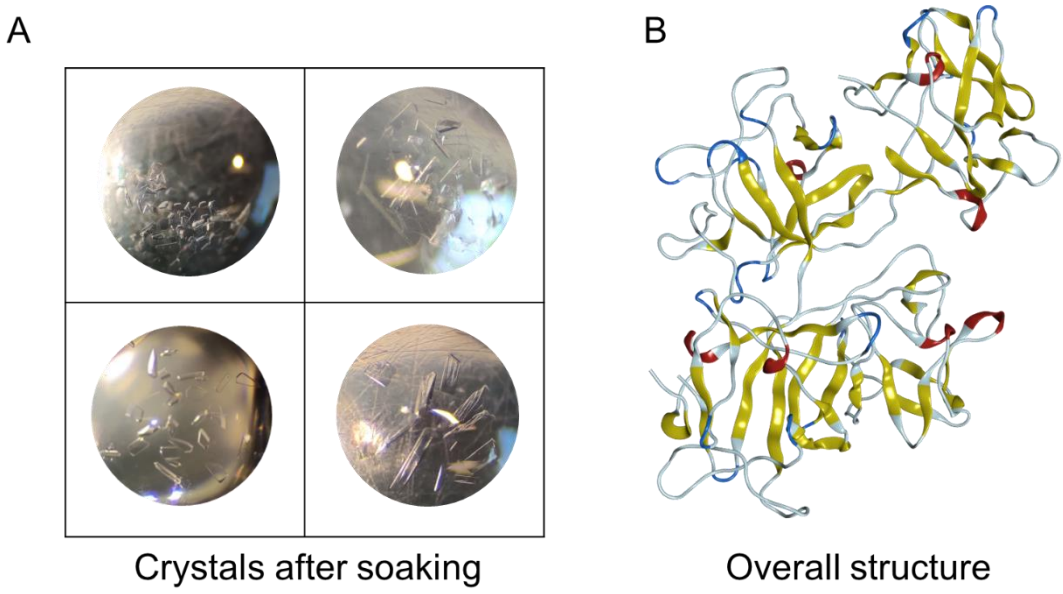


Figure 4.1: X-ray crystallography of fascin using soaking method. **A)** Images of crystal droplets after soaking with BTA-EG$_6$ **B)** Overall image of the 2.6Å structure of fascin after soaking with BTA-EG$_6$. The electron density of BTA-EG$_6$ was not seen in this structure.

Potential reasons for not seeing the molecule in the co-crystal structure might be due to the competitive binding of PEG from the crystallization conditions to the binding site of BTA-EG$_6$, or exclusion of BTA-EG$_6$ by the crystal lattice. Structural data from a related study suggested that PEG molecules can occupy the binding site near Arginine 389[38] (Figure 4.2), which is in the same vicinity where we have proposed our molecules to bind, potentially interfering with BTA-EG$_6$ binding. Despite these challenges, along with

Dr. Kyle Berg, I explored alternative crystallization conditions without PEG, screening numerous conditions without success. I also looked at buffer exchanging the crystal to go from PEG to a non-PEG environment but that also did not work. Consequently, we turned to protein NMR as an alternative method to gain structural insights into the interaction between BTA-EG_6 and fascin.

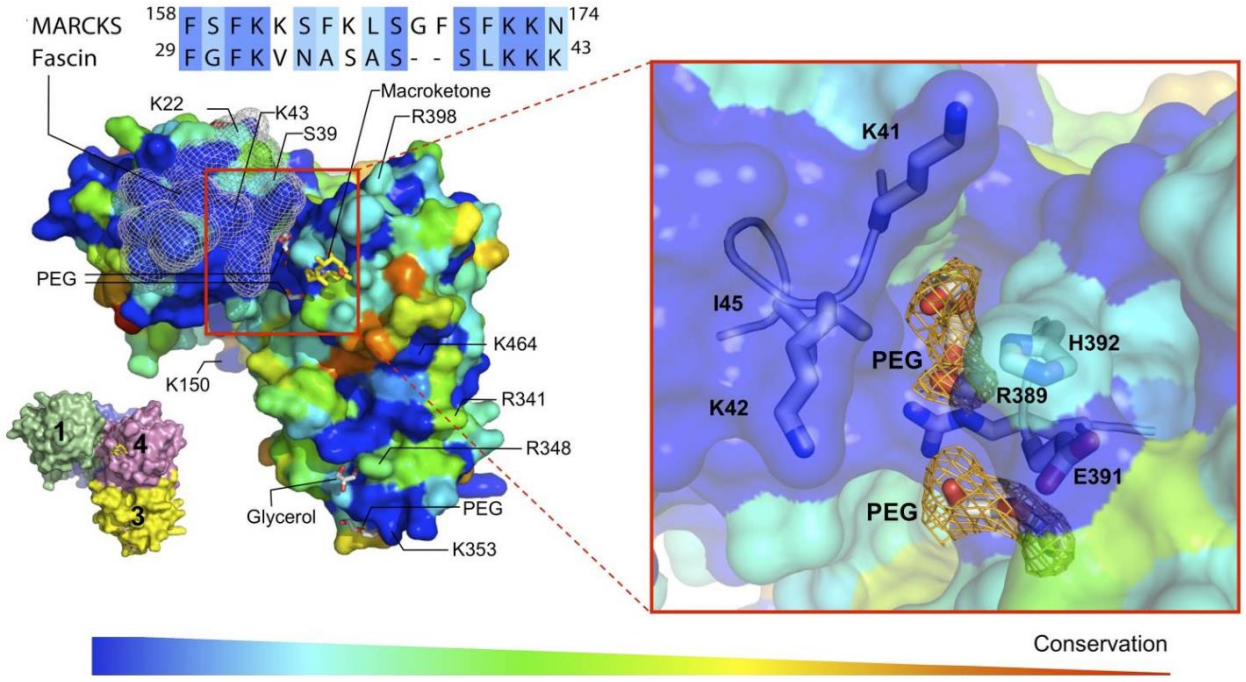


Figure 4.2: Surface representation of the actin-binding site in β trefoil 1 colored by residue conservation (*left*) and an enlarged view (*right*) showing molecules of PEG bound in the cleft formed at the interface between β trefoil domains 1 and 4. Residue conservation decreases from blue to red as indicated by the bar at the bottom of the figure. Reproduced from Jansen *et al*[38].

4.4 Introduction to protein NMR

Protein NMR is a dynamic technique, showing protein flexibility and conformational changes[110]. Compared to X-ray crystallography it can be non-destructive and non-invasive to the sample in solution[111]. Protein NMR can reveal different conformations and fluctuations in the protein's structure and interactions within the protein[110]. In terms of

drawbacks, data interpretation can be complex, especially for larger proteins. And the signal-to-noise ratio requires a large amount of pure protein. In general, protein NMR is typically more challenging for proteins ≥30kDa[112,113]; fascin (~55kDa) falls into this category.

Solution protein NMR relies on detecting the amide N-H signals along the backbone of the polypeptide chain of the protein[114]. Each N-H signal corresponds to a single amino acid, except for prolines which lack the N-H common to most amino acids, and the starting methionine which can be absent due to processing during expression[115]. For a protein like fascin with 493 amino acids, 15 prolines, and a starting methionine, the expected number of observable N-H peaks is 477. To appear in NMR spectra, the amide nitrogen must be enriched with the proper atomic spin[114], typically achieved by isotopically enriching nitrogen-15 (^{15}N) and carbon-13 (^{13}C), rather than their predominant natural forms (^{14}N and ^{12}C, respectively). Hydrogen-1 (^{1}H) signals, however, do not require isotopic enrichment and are often suppressed using deuterium (^{2}H) to reduce background noise from ubiquitous ^{1}H signals[114].

Each isotope provides distinct NMR signals, observable in one-dimensional spectra. Two-dimensional and three-dimensional NMR experiments further correlate nuclei that are spatially close to each other. For instance, heteronuclear single quantum coherence (HSQC) spectroscopy correlates N-H amide peaks[114], while three-dimensional experiments like HNCA and HNCACB correlate N-H (HN) with α-carbon (CA) and β-carbon (CB) signals of amino acids, respectively[116–118]. These experiments leverage unique chemical shifts of α and β carbons across amino acids to identify correlations between N-H peaks and specific amino acids.

Transverse relaxation optimized spectroscopy (TROSY) experiments are particularly beneficial for large proteins like fascin, offering enhanced signal and resolution[119]. A combination of these NMR techniques could potentially provide comprehensive data to elucidate the binding site of BTA-EG_6 to fascin.

4.5 Previous studies in the Yang lab – 2D solution NMR of WT fascin

Based on literature precedence, it was considered impractical to employ solution NMR technique for fascin due to its size (~55kDa), which typically leads to overlapping peaks[111–113]. But despite potential challenges, Dr. Kyle Berg was able to obtain the TROSY-HSQC spectrum for fascin which exhibited excellent resolution for a protein of this size[68]. The spectrum revealed 463 out of the expected 477 peaks of fascin, indicating 97% coverage (Figure 4.3). This high coverage and resolution were particularly impressive for a protein of this size.

Subsequently, Dr. Kyle Berg conducted follow up TROSY-HSQC experiments under the same conditions with the addition of 600 µM BTA-EG_6 (a 2:1 ratio of small molecule to protein) to probe for spectral perturbations indicative of BTA-EG_6 binding sites. Overlaying this spectrum with the apo protein spectrum (Figure 4.4) revealed approximately 50-60 peaks exhibiting clear chemical shift differences[68]. These shifts likely corresponded to the amino acid residues which are influenced by being in the proximity of BTA-EG_6, suggesting either direct binding interactions or conformational changes that were induced upon compound binding.

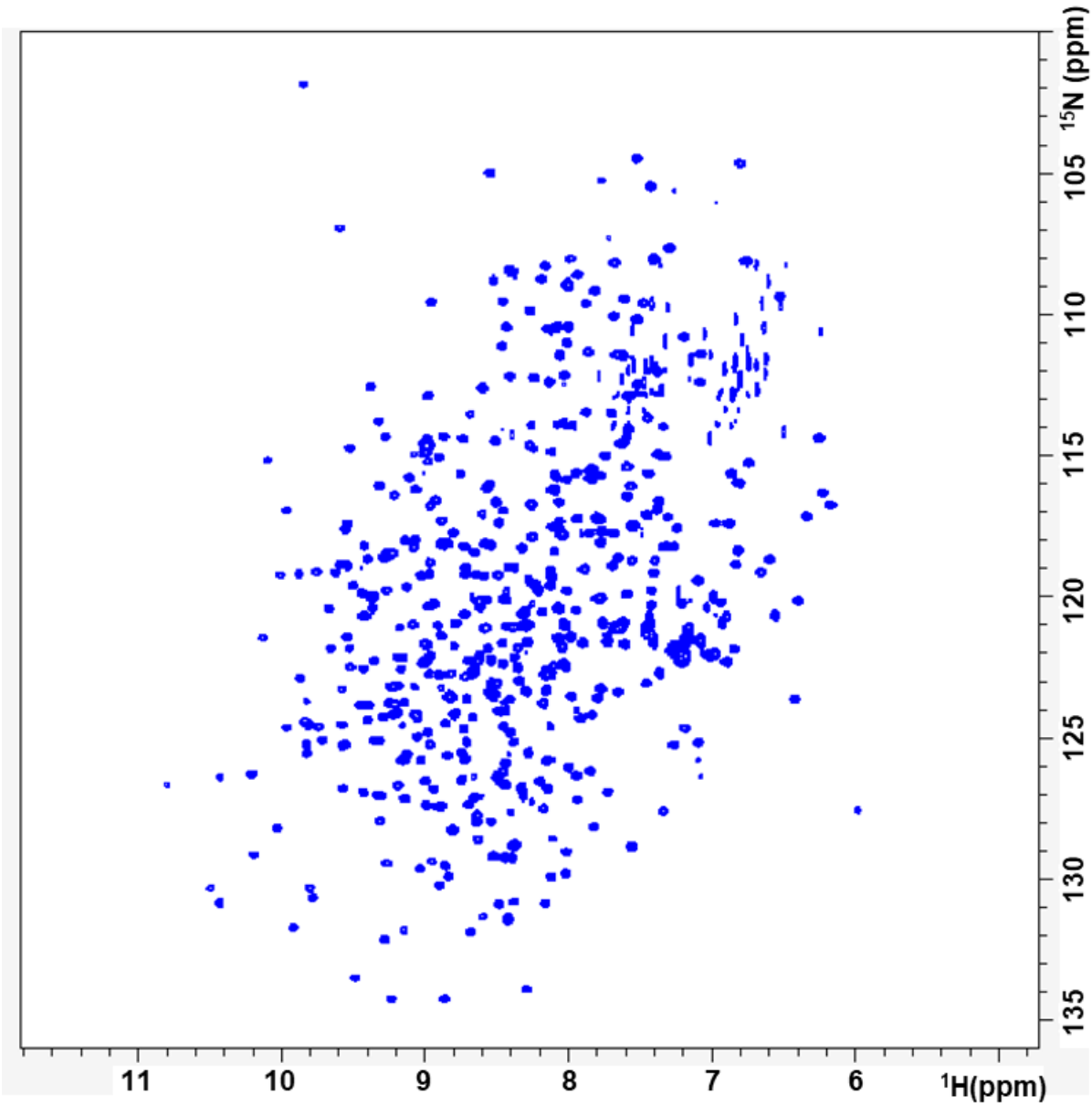


Figure 4.3: TROSY-HSQC of fascin in solution. 463 out of 477 expected peaks were visualized for 97% coverage. (Data from Dr. Kyle Berg's dissertation[68]).

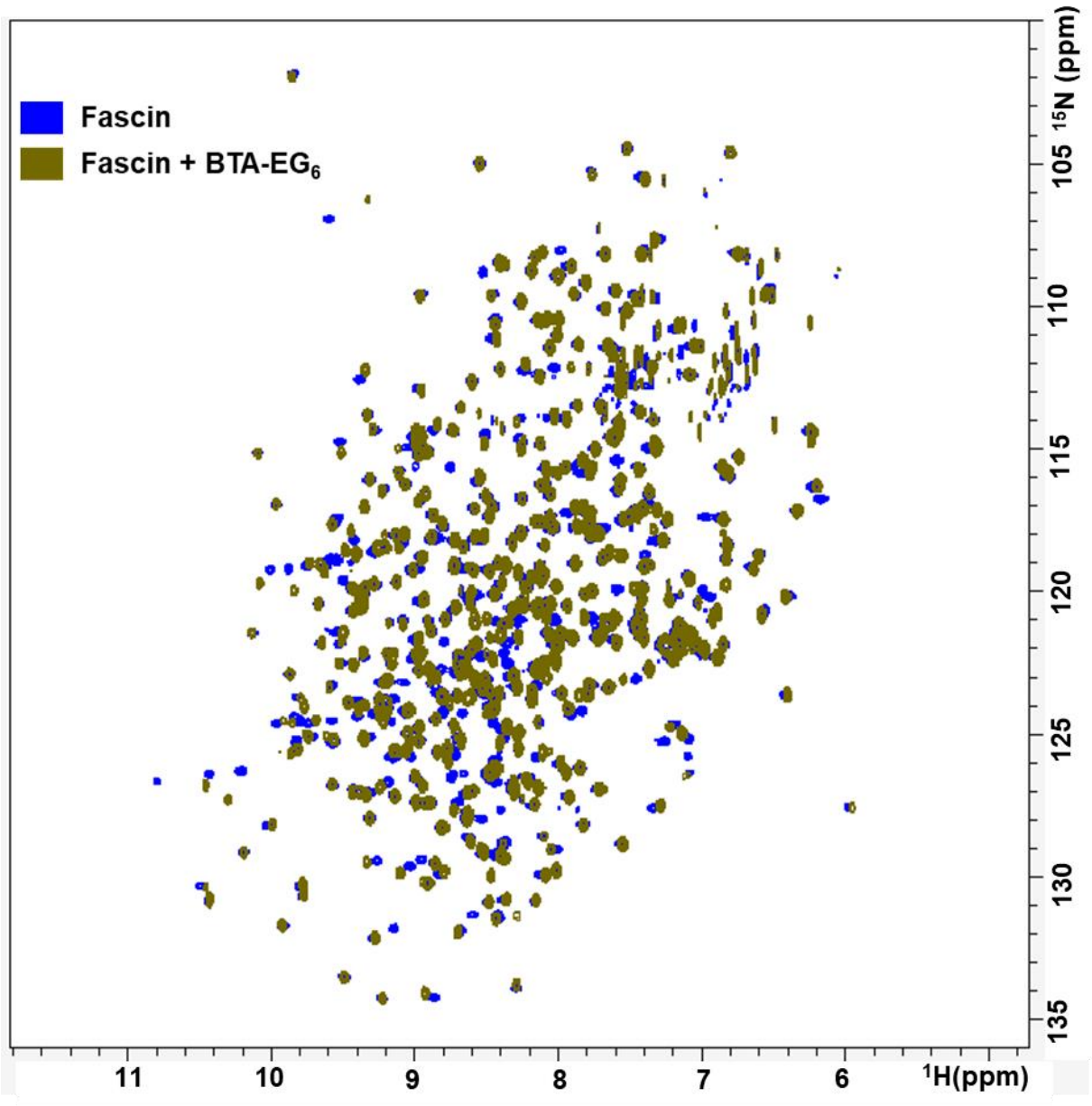


Figure 4.4: TROSY-HSQC of fascin (blue) overlayed with TROSY-HSQC of fascin with BTA-EG_6 added (olive green) (Data from Dr. Kyle Berg's dissertation[68]).

Assigning peaks, however, proved to be difficult and follow up 3D NMR experiments such as HNCACB[116], CBCAHN[116] and HN(CO)CA[120] did not provide sufficient signal quality at the fascin concentration being used. Due to the size of fascin there were many overlapping peaks, and only some peaks were successfully assigned in less crowded regions of the spectrum while densely packed regions presented difficulties. This prompted a shift in strategy to identify key residues in the binding pocket.

4.6 Site directed mutagenesis

Since fully assigning the residues of full-length fascin proved challenging with the methods previously used in the Yang lab, I redirected my efforts toward identifying key

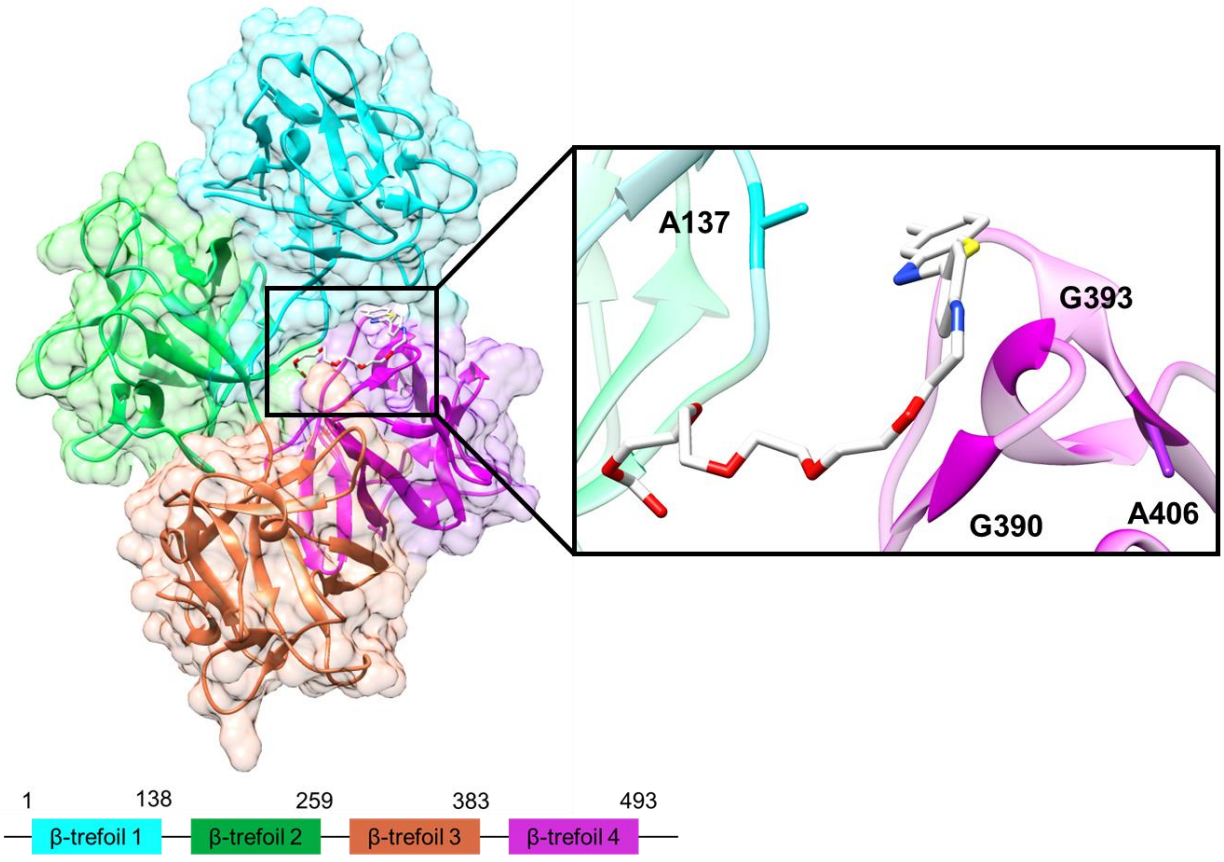


Figure 4.5: Proposed binding site of BTA-EG$_6$ with fascin between β trefoils 1 (cyan) and 4 (purple). Residues A137, A406, G390 and G393 were chosen for point mutations.

residues involved in the binding of BTA-EG_6 by other methods. For the next set of analysis, Dr. Kyle Berg and I collaborated with Dr. Sang Ho Park, Dr. Xuemei Huang and Professors Stanley Opella and Galia Debelouchina, experts in protein NMR at UCSD. Together with them, I identified residues to target in the binding pocket based on the model that I had proposed in the previous chapter for the fascin-BTA-EG_6 complex. I mainly focused on Alanine and Glycine residues: A137, G390, G393 and A406 (Figure 4.5), that are in proximity of the proposed binding pocket of fascin and are expected to interact with BTA-EG_6.

Since I had previously generated fascin mutant A137K and found that the construct expressed well and in good quantities, I went through and tested different point mutation for the residues G390, G393 and A406. Finally, I decided on mutations G390S, G393S and A406S for further analysis. These mutations enabled me to express and purify fascin mutant proteins in enough quantities to perform the solution NMR experiments. After confirming that all fascin mutant proteins were properly folded and were functionally active like WT fascin, I carried out binding studies of these mutant proteins with BTA-EG_6 using ITC.

As previously discussed, fascin mutant A137K bound significantly better to BTA-EG_6 as compared to WT fascin. On the contrary, mutation G390S significantly disrupted the binding interaction between fascin and BTA-EG_6. The other two mutations A406S and G393S, both influenced the binding affinity to BTA-EG_6 compared to that of WT fascin, but they were not found to be statistically significant (Figure 4.6). After confirming that these fascin mutant proteins were still binding to BTA-EG_6, I was ready to express them as uniformly labeled proteins for TROSY-HSQC NMR experiments.

A

Mutant	Binding Affinity	Kd (μM)	ΔH (kJ/mol)	ΔS(J/mol·K)	ΔG(kJ/mol)
WT Fascin	-	4.8 ± 0.7	-20.9 ± 1.7	31.8 ± 7.2	-30.4 ± 3.9
A406S	No Change	3.4± 0.7	-12.3 ± 0.9	63.4 ± 1.5	-31.2 ± 0.5
A137K	Increase	0.75 ± 0.03	-11.6 ± 0.2	78.5 ± 1.2	-35.0 ± 0.6
G393S	No Change	5.8 ± 1.5	-13.6 ± 1.6	54.5 ± 3.9	-29.9 ± 0.6
G390S	Decrease	7.6 ± 0.4	-9.3 ± 0.7	66.7 ± 1.9	-29.2 ± 0.1

B

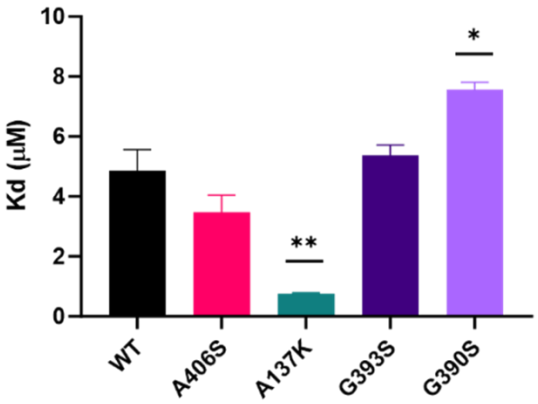


Figure 4.6: A) Binding affinity data for WT fascin and fascin mutants with BTA-EG$_6$. **B)** Graphical representation of the binding affinities of WT fascin and fascin mutants. Each mutant was compared to WT fascin. Statistical analysis was performed using a two tailed Welch's *t*-test (*p<0.05, **p<0.01, n=3 for each.)

4.7 Identification of peak belonging to G390

To identify the peak corresponding to residue G390, I expressed and purified 15N uniformly labeled mutant protein G390S for two-dimensional NMR analysis using TROSY-HSQC. As G390 is forming the loop region in the β trefoil 4 domain of fascin (Figure 4.5), I anticipated that the mutations would cause shifts in the chemical environment of nearby residues. I overlaid the spectrum obtained for the uniformly labeled G390 fascin mutant protein with that of the uniformly labeled spectrum of WT fascin

(previously obtained by Dr. Kyle Berg[68]) and found that about 50-60 peaks showed visible chemical shifts in the fascin mutant spectrum of G390S as compared to the WT fascin spectrum (Figure 4.7).

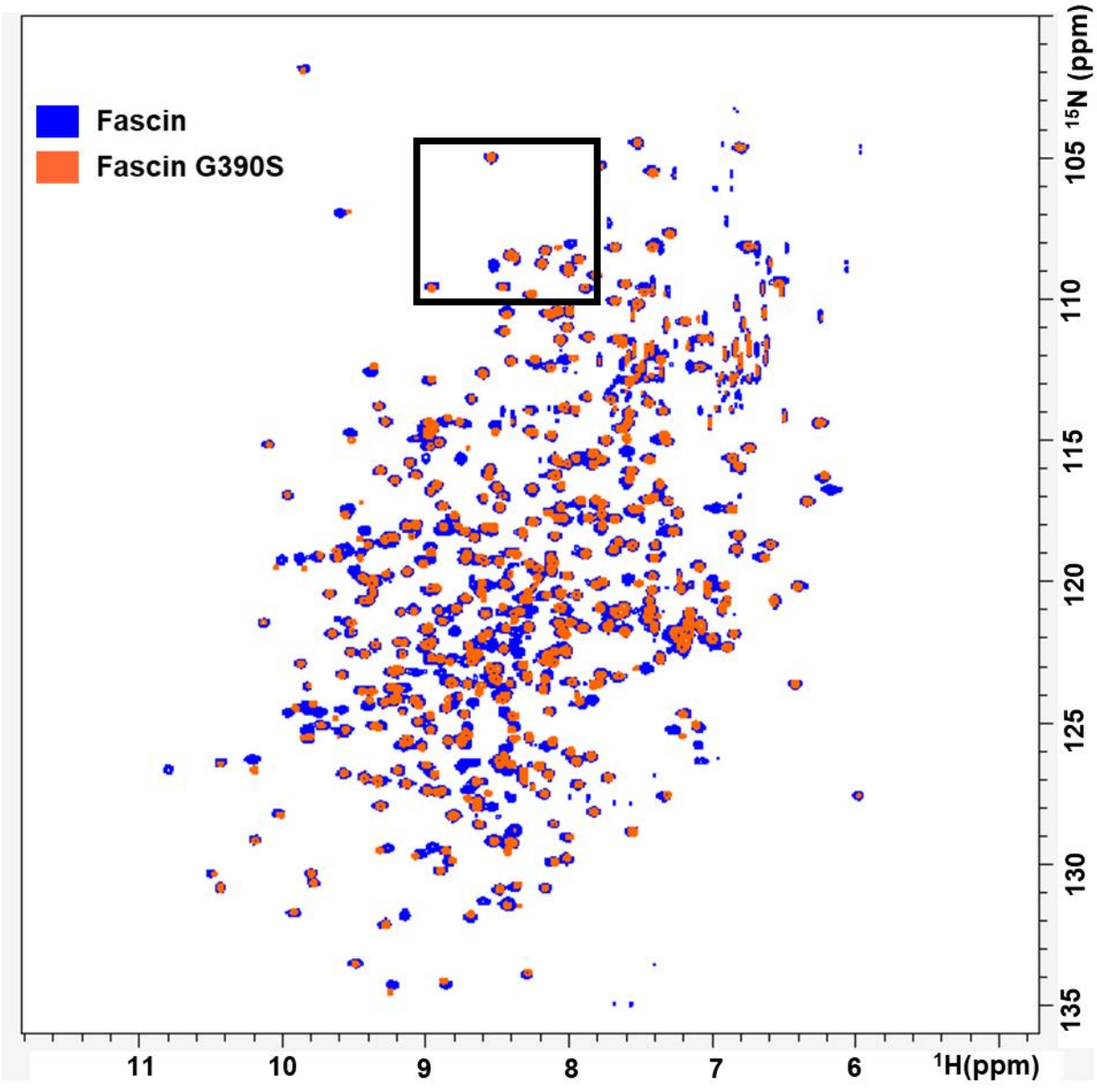


Figure 4.7: TROSY-HSQC of uniformly labeled WT fascin (blue) overlayed with TROSY-HSQC of uniformly labeled fascin mutant G390S (orange).

Next, I expected that the peak corresponding to the point mutation G390S to disappear in the uniformly labeled spectrum of G390S without a corresponding new peak nearby. On closer inspection and comparison to the WT spectrum, I was able to identify the disappearance of G390 peak in the G390S mutant spectrum (Figure 4.8A), clearly indicating the identity of this peak in the WT fascin spectrum.

To further confirm the identification of this peak as a glycine, I referred the 3D HNCA spectrum of WT fascin (previously obtained by Dr. Kyle Berg[68]). Selective labeling of glycine residues was unnecessary for peak identification because glycine residues exhibit a distinct characteristic α-carbon chemical shift[121]. Glycine's unique α-carbon chemical shift averages around 45 ppm, whereas other amino acids with a β-carbon adjacent to the α-carbon show an average α-carbon chemical shift which ranges from 53-63 ppm[121]. Analyzing the HNCA spectrum of WT fascin and correlating N-H peaks to α-carbon, I identified the peak in contention that disappeared in the G390S mutant spectrum to be a glycine residue with a chemical shift of 43.0 ppm (Figure 4.8B).

Subsequently, I compared the original spectra obtained by Dr. Kyle Berg at the same chemical shift values between WT fascin and WT fascin in presence of BTA-EG_6 overlaid (Figure 4.8C) to investigate if the peak G390 showed chemical shift changes upon BTA-EG_6 binding. Indeed, I observed a chemical shift perturbation for the peak G390 in the presence of BTA-EG_6 (Figure 4.8C), suggesting the involvement of residue G390 in the binding pocket of BTA-EG_6 to fascin.

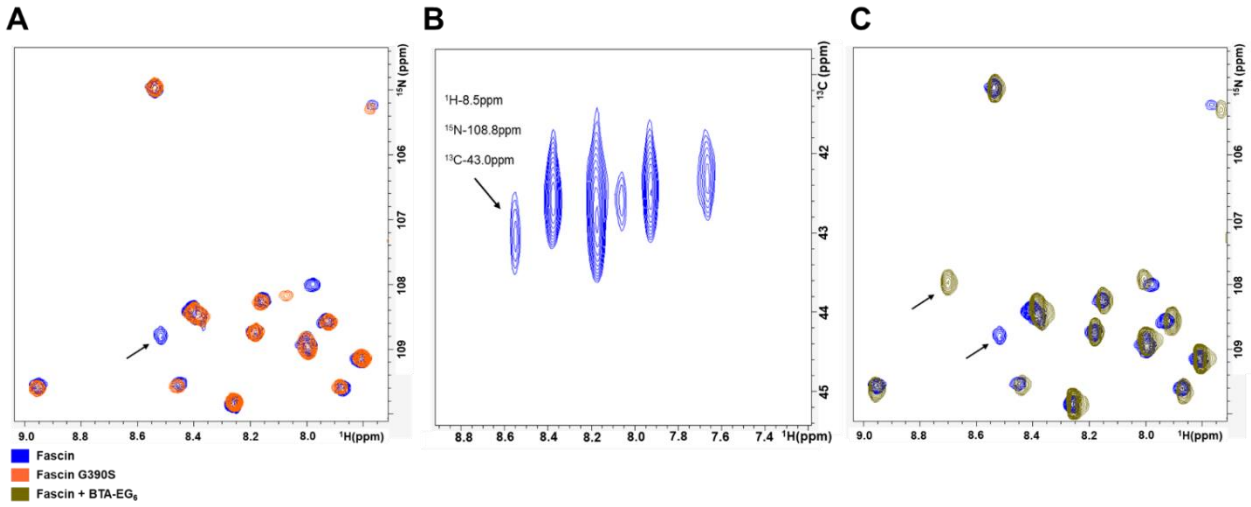


Figure 4.8: Identification of peak corresponding to residue G390. **A)** Zoomed in overlay of TROSY-HSQC of uniformly labeled WT fascin (blue) with the TROSY-HSQC of uniformly labeled G390S fascin mutant (orange). **B)** Overlay of TROSY-HSQC of uniformly labeled WT fascin (blue) and TROSY-HSQC of uniformly labeled WT fascin in presence of BTA-EG_6 (olive green). Arrows indicate that peak G390 disappears in (A) and shows a chemical shift upon binding to BTA-EG_6 in (B)

4.8 Identification of peak belonging to G393

Similar experiments and analysis as that for G390 were carried out for the identification of glycine residue G393. First, I carried out the expression and purification of uniformly labeled 15N mutant protein G393S for two-dimensional NMR analysis using TROSY-HSQC. G393 is also in the same loop region as G390 (Figure 4.5), hence I anticipated that the mutation would cause shifts in the chemical environment of nearby residues. On overlaying the spectrum obtained for the uniformly labeled G393 fascin mutant protein with that of the uniformly labeled spectrum of WT fascin (previously obtained by Dr. Kyle Berg[68]), visible chemical shifts of about 50-60 peaks were again

seen in the fascin mutant spectrum of G393S as compared to that of the WT spectrum (Figure 4.9).

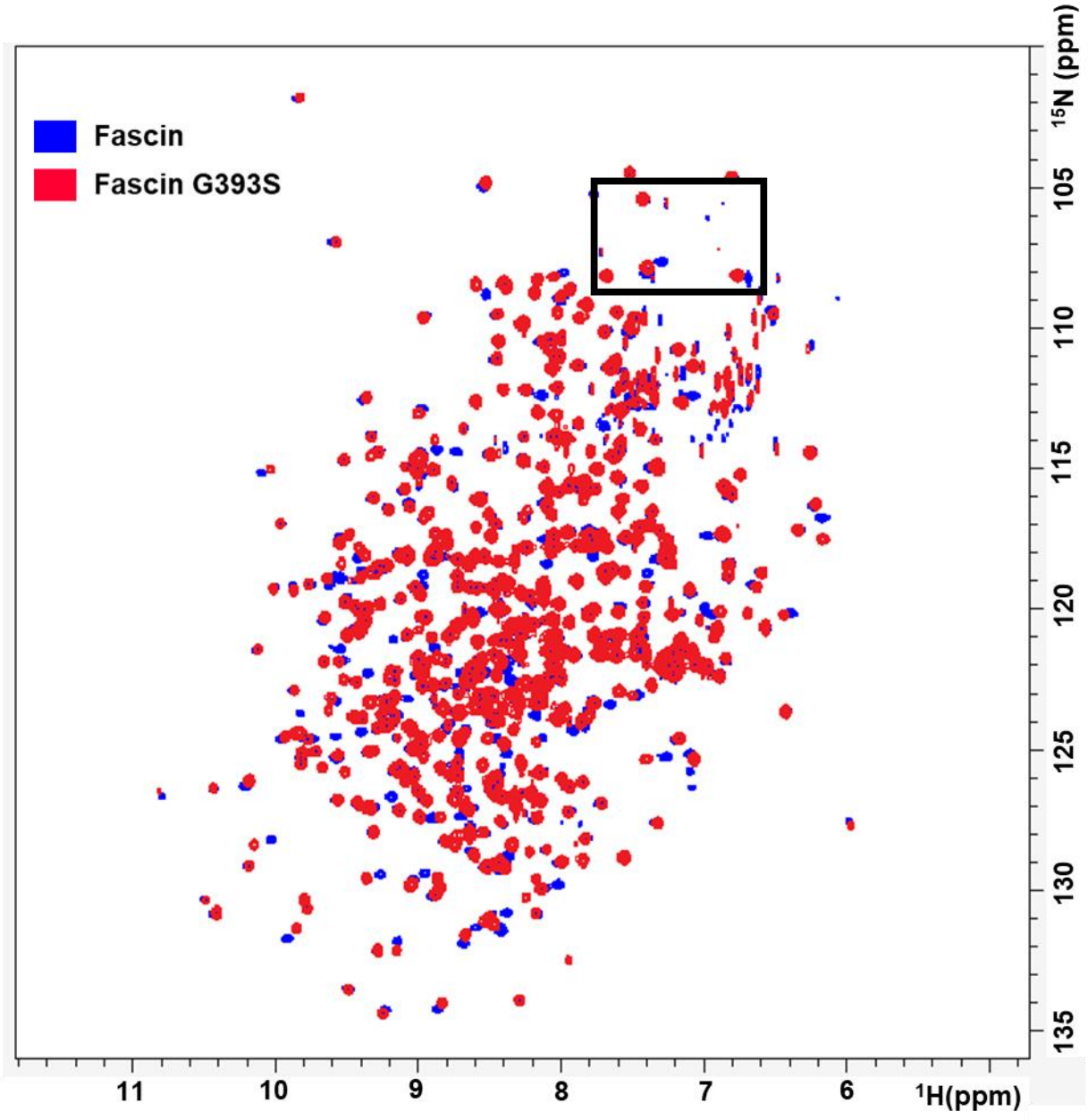


Figure 4.9: TROSY-HSQC of uniformly labeled WT fascin (blue) overlayed with TROSY-HSQC of uniformly labeled fascin mutant G393S (red).

Next, I was able to identify the disappearance of peak corresponding to residue G393 in the G393S mutant spectrum (Figure 4.10A), clearly indicating the identity of this peak

in the WT fascin spectrum. Referencing the HNCA 3D spectrum of WT fascin (previously obtained by Dr. Kyle Berg[68]), correlating N-H peaks to α-carbon, I identified the peak in contention that disappeared in the mutant spectra of G393S to be a glycine residue (Figure 4.10B). Finally, I compared the original uniformly labeled spectra obtained by Dr. Kyle Berg at the same chemical shift values between WT fascin and WT fascin with BTA-EG_6 overlaid (Figure 4.10C) to reveal that there was an observed chemical shift perturbation for the peak G393 in the presence of BTA-EG_6 (Figure 4.10C), suggesting the involvement of residue G393 in the binding pocket of BTA-EG_6 to fascin.

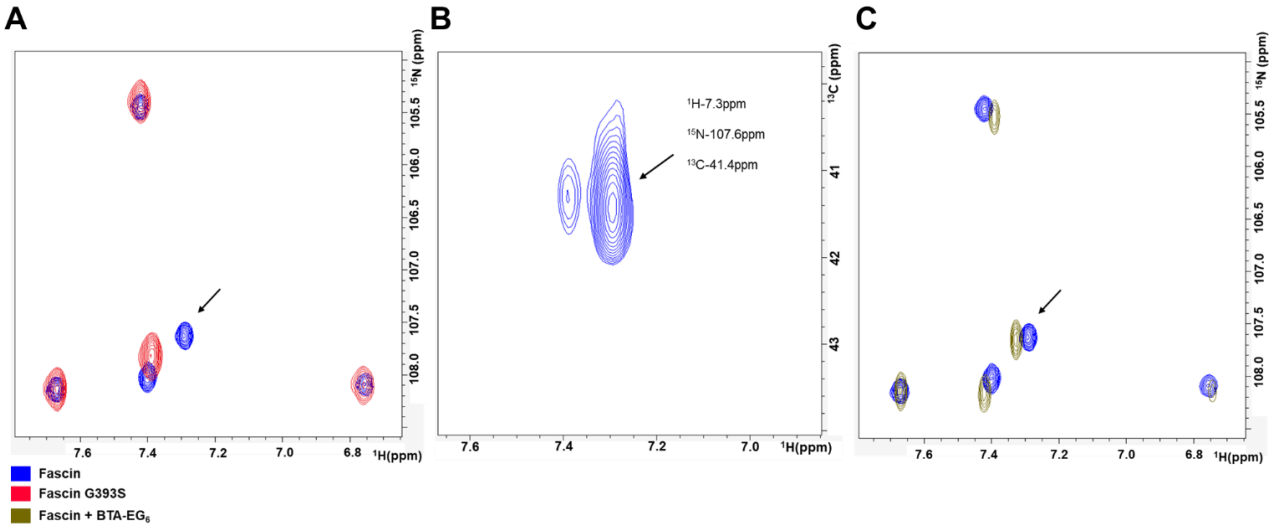


Figure 4.10: Identification of peak corresponding to G393. **A)** Zoomed in overlay of the TROSY-HSQC for uniformly labeled WT fascin (blue) with the TROSY-HSQC of uniformly labeled G393S fascin mutant (red). **B)** Overlay of TROSY-HSQC of uniformly labeled WT fascin(blue) and WT fascin in the presence of BTA-EG_6 (olive green). Arrows indicating that peak G393 disappears in (A) and shows a chemical shift upon binding to BTA-EG_6 in (B).

4.9 Selective labeling of Ala residues

After identifying the peaks corresponding to residues G390 and G393 in the WT fascin spectrum, I focused on identifying the Ala residues. Unlike glycine residues, alanine

lacks a uniquely distinctive signature average chemical shift that could be used to identify it from the rest of the amino acids[121,122]. Hence, I used the selectively labeled alanine spectrum of WT fascin which was previously obtained by Dr. Kyle Berg[68]. He labeled alanine residues by growing bacteria in media spiked with 15N-labeled alanine and other unlabeled amino acids prior to induction. The resultant two dimensional TROSY-HSQC spectrum of alanine-labeled WT fascin overlapped well with uniformly labeled WT fascin (Figure 4.11). 45 out of 49 expected alanine residues (92% coverage) were identified in the protein sequence[68]. This facilitated comparisons of WT fascin spectrum and the spectra obtained from uniformly labeled fascin mutants A406S and A137K.

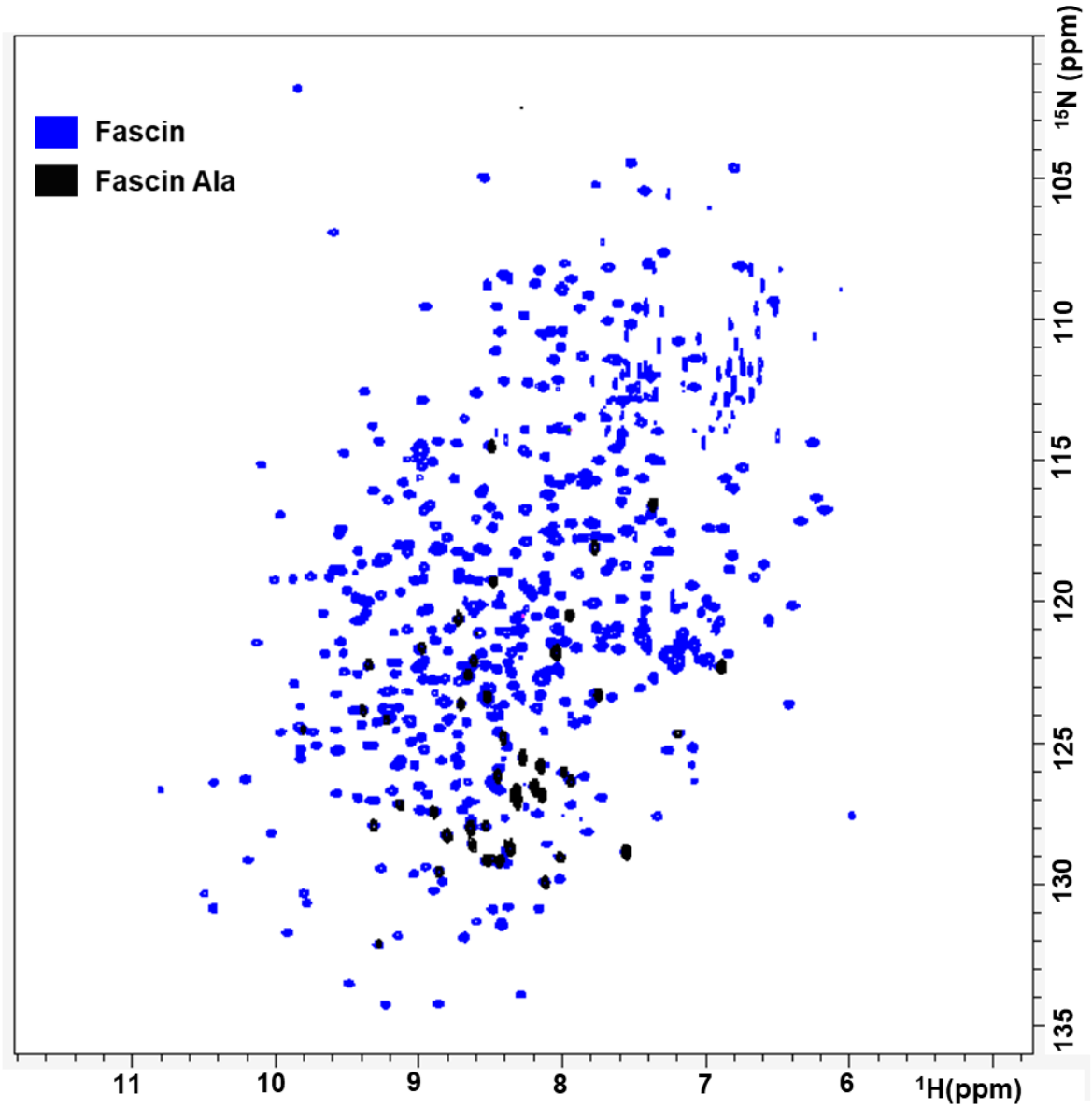


Figure 4.11: TROSY-HSQC of uniformly labeled WT fascin (blue) overlayed with TROSY-HSQC of alanine labeled WT fascin (black). (Data obtained from Dr. Kyle Berg's dissertation[68]).

4.10 Identification of peak corresponding to A137

I expressed and purified uniformly 15N uniformly labeled fascin mutant protein A137K for two-dimensional NMR analysis using TROSY-HSQC. For A137K, I mutated a small

hydrophobic residue (Ala) to a charged polar residue (Lys), anticipating that this change would create perturbations in the binding pocket. When overlaying the spectrum of uniformly labeled mutant protein A137K with the uniformly labeled WT fascin spectrum (previously obtained by Dr. Kyle Berg[68]), I again observed good convergence, with approximately 60 peaks showing non overlapping chemical shifts (Figure 4.12).

As with the glycine mutations, the disappearance of the peak corresponding to mutation A137 in the mutant spectrum would be the clearest indication of the identity of the peak corresponding to residue A137 in the original WT fascin spectrum. Overlaying the uniformly labeled spectrum of WT fascin with that of the spectrum obtained of uniformly labeled A137K mutant, I identified a peak that disappeared in the A137K spectrum (Figure 4.13A). By comparing this with the alanine-labeled spectrum of WT fascin, I confirmed that the missing peak was indeed an alanine residue and concluded that the missing peak corresponded to A137 (Figure 4.13B). Subsequently, I overlaid the uniformly labeled spectrum of WT fascin with that of uniformly labeled spectrum of WT fascin in presence of BTA-EG_6 and observed a chemical shift in the peak when incubated with BTA-EG_6 (Figure 4.13C), providing us of evidence of the involvement of residue A137 in the binding pocket of BTA-EG_6.

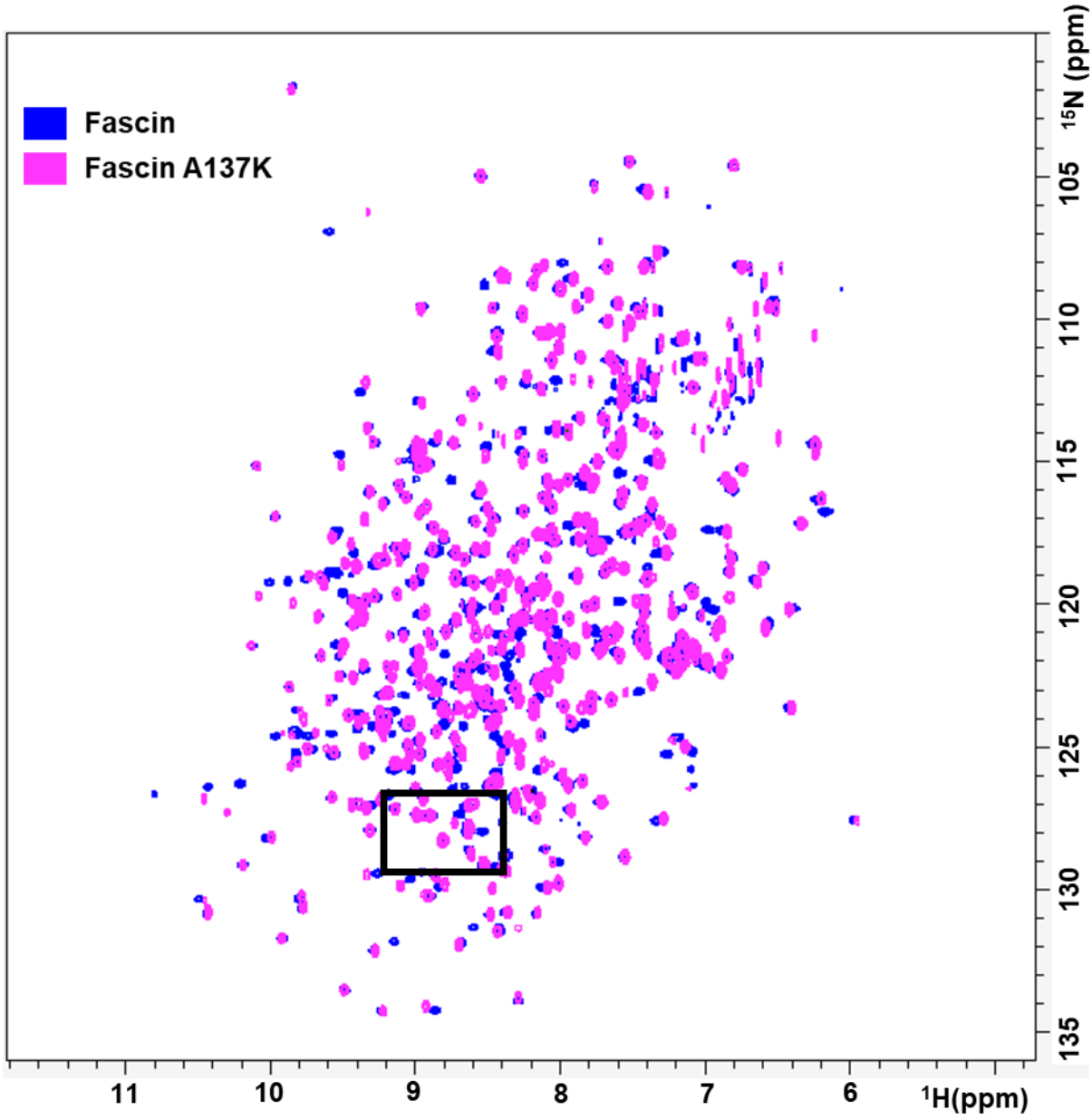


Figure 4.12: TROSY-HSQC of uniformly labeled WT fascin (blue) overlayed with TROSY-HSQC of uniformly labeled fascin mutant A137K (pink).

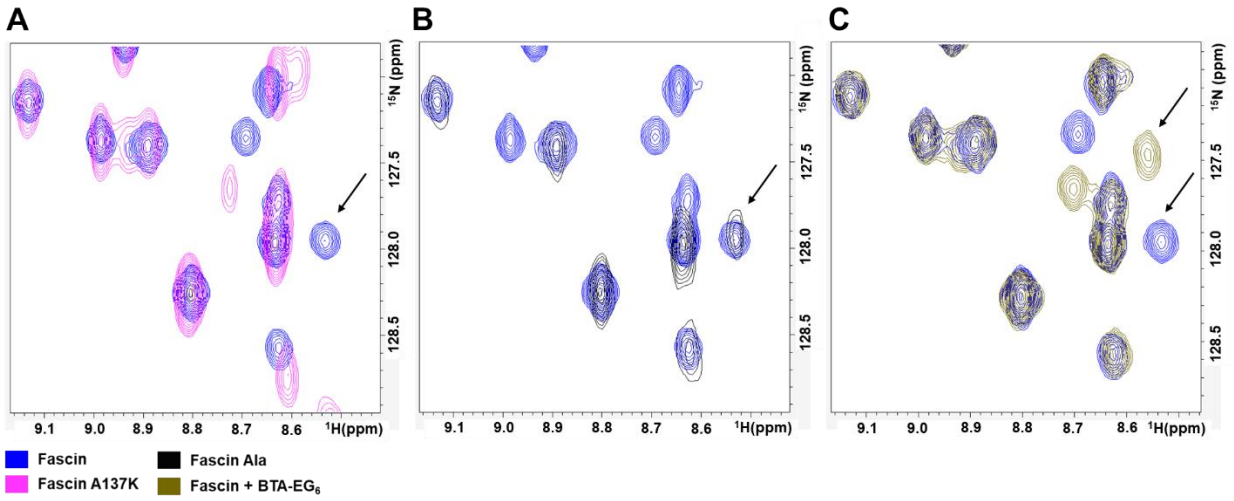


Figure 4.13: Identification of peak corresponding to A137. **A)** Zoomed in overlay of the TROSY-HSQC for uniformly labeled WT fascin (blue) with the TROSY-HSQC of uniformly labeled fascin mutant A137K (pink) **B)** Overlay of uniformly labeled WT fascin (blue) with alanine labeled WT fascin (black). **C)** Overlay of uniformly labeled WT fascin (blue), Ala labeled WT fascin (black) and uniformly labeled WT fascin in presence of BTA-EG_6 (olive green). Arrows indicate peak A137 disappears in (A) and is identified as an Alanine residue in (B) which shows a chemical shift upon binding to BTA-EG_6 in (C)

4.11 Identification of peak corresponding to A406

The same set of experiments and analysis for the identification of A137 was carried out for the identification of the peak corresponding to A406. Firstly, I expressed and purified uniformly 15N uniformly labeled fascin mutant protein A406S for two-dimensional NMR analysis using TROSY-HSQC. A406 is also located in a flexible beta turn region in proximity with glycine residues G390 and G393 (Figure 4.5), and I expected the A406S mutation to cause some perturbations in the chemical shifts of nearby residues.

When overlaying the spectrum of uniformly labeled mutant protein A406S with that of uniformly labeled WT fascin spectrum (previously obtained by Dr. Kyle Berg[68]), there

was good overlap between the spectra, with approximately 60 peaks showing non overlapping chemical shifts (Figure 4.14).

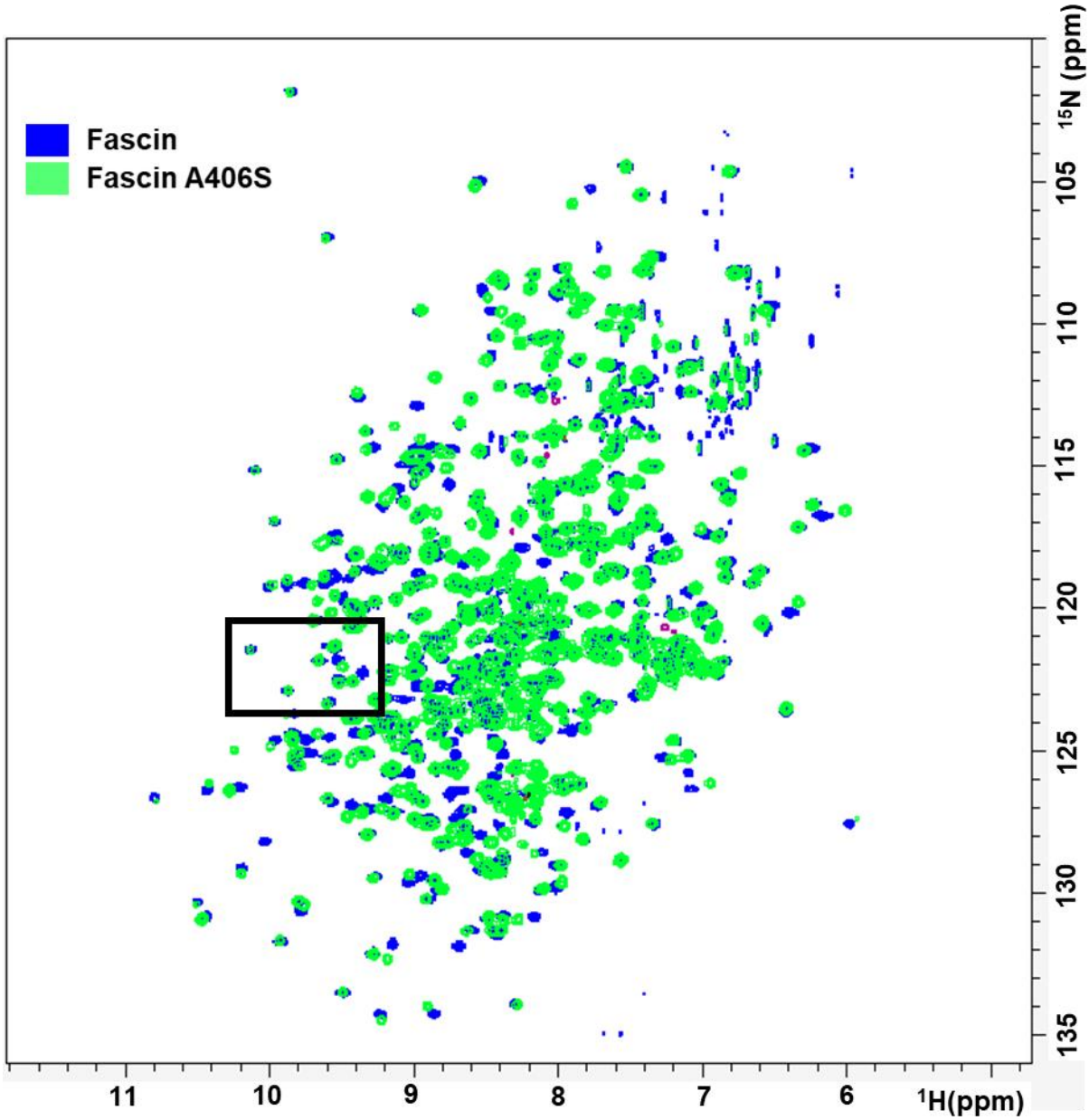


Figure 4.14: TROSY-HSQC of uniformly labeled WT fascin (blue) overlayed with TROSY-HSQC of uniformly labeled fascin mutant A406S (green).

Overlaying the uniformly labeled spectra of WT fascin and the fascin mutant A406S, I identified a peak that disappeared in the A406S spectrum (Figure 4.15A). By

comparing this with the alanine-labeled spectrum of WT fascin, I concluded that the missing peak was indeed an alanine and corresponded to residue A137 (Figure 4.15B). Subsequently, I overlaid the uniformly labeled spectra of fascin with and without BTA-EG_6 and observed a chemical shift in the peak in the presence of BTA-EG_6 (Figure 4.15C), supporting the idea that residue A406 is involved in or is near the binding pocket of BTA-EG_6 on fascin.

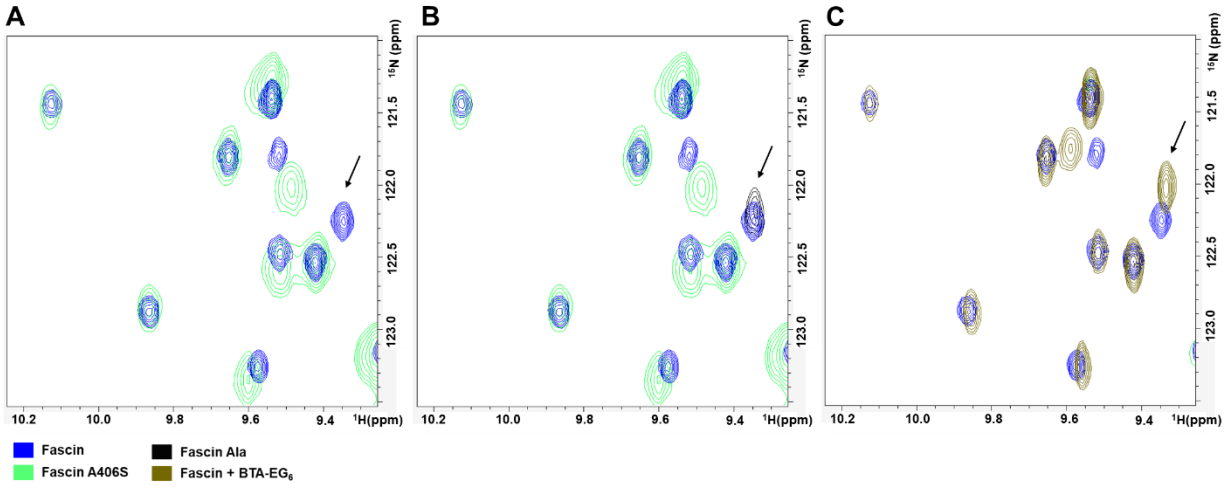


Figure 4.15: Identification of peak corresponding to A406. **A)** Zoomed in overlay of the TROSY-HSQC of uniformly labeled WT fascin (blue) with the TROSY-HSQC of uniformly labeled A406S fascin mutant (green) **B)** Overlay of uniformly labeled WT fascin (blue), uniformly labeled A406S (green) and alanine labeled WT fascin (black). **C)** Overlay of uniformly labeled WT fascin (blue), and uniformly labeled WT fascin in presence of BTA-EG_6 (olive green). Arrows indicate peak A406 disappears in (A) and is identified as an alanine residue in (B) which shows a chemical shift upon binding to BTA-EG_6 in (C**).**

4.12 Conclusion

Obtaining a protein NMR spectrum for a protein of ~55kDa is novel and paves the way for future analyses. The identification of residues G390, G393, A406 and A137 provides insights into their involvement in the binding pocket of BTA-EG_6 with fascin, as

previously suggested. These experiments set the stage for further investigations for BTA-EG_6 binding and for the complete assignment of the WT fascin spectrum. Such findings are pivotal for future research on therapeutic strategies targeting fascin in neurodegenerative disorders and cancer, offering an alternative to crystallization for structural determinations of therapeutic binding.

4.13 Methods

Expression and purification of unlabeled WT and mutant fascin proteins

Site directed mutagenesis was carried out to create fascin mutants as discussed in Chapter 3. The expression and purification of WT fascin and fascin mutant proteins was also carried out as discussed previously in Chapter 3. After affinity columns, the protein was passed through S200 size exclusion chromatography column in protein buffer (20mM Tris, 40mM KBr, and 0.5M EDTA pH 8.0) for crystallography or NMR buffer (40mM HEPES, 90mM 1mM TCEP NaCl pH 6.0) for protein NMR studies. The protein was then concentrated using a 30kDa cutoff (Millipore) to the desired concentration.

Crystallography of WT fascin

Crystals for diffraction were obtained by mixing 2µL of 14mg/mL fascin in protein buffer (20mM Tris, 40mM KBr, and 0.5M EDTA pH 8.0, 2mM BTA-EG_6) with 2µL crystallization buffer (14-24% PEG 4000 100mM HEPES pH 8.0, 1mM DTT) on a glass coverslip and sealed over a well containing 1mL crystallization buffer. Crystals were allowed to form over the course of 3 days. Crystals were exchanged into cryo buffer (crystallization conditions plus additional glycerol for a final concentration of 30%

cryoprotectant) to inhibit ice crystal formation upon flash-freezing, collected in loops and frozen in liquid nitrogen. Crystals were sent to the synchrotron at Argonne National Lab. Diffraction data collection was performed by remote control of the beamline at that location. Data was reduced with XDS package utilities[123], molecular replacement was performed with PHASER[124], then iterative refinement and building was performed with Coot[125] and phenix.refine[126].

Expression of uniformly 15N labeled WT and mutant fascin proteins for TROSY-HSQC NMR experiments

Plasmids were transformed into DE3-BL21 cells using the manufacturer's protocol. A colony was selected for growth for 5hrs in 2-3mL LB broth with 100 µg/mL ampicillin with shaking at 220rpm and 37°C. 200µl of the culture was then transferred into a 50mL culture containing M9 or Mengli mimimal media containing 1g of either 15N labeled ammonium chloride or ammonium sulfate and 8g of unlabeled glucose. The culture was then transferred to a 1L culture containing Mengli media (prewarmed to 37°C) and 100 µg/uL ampicillin. The culture was allowed to grow to an OD of 0.8-1.0 at which point the temperature was reduced to 17°C and culture was induced with 0.5 mM IPTG. The culture was allowed to incubate overnight, and the bacterial pellet was harvested by centrifugation at 3000xg for 30mins and frozen at -80°C. Purification proceeded as described previously.

NMR experiments

All protein NMR experiments were recorded at 37°C on Bruker Avance Neo 800MHz spectrometers equipped with TXO 1H/13C/15N cryoprobes. 1H/15N TROSY-HSQC data was recorded with 2k and 256 complex points. The NMR data were processed with NMRPIPE and analyzed with Bruker Topspin 4[127].

4.14 Acknowledgements

I would like to thank Professor Kevin Corbett for his support and helping me understand factors effecting protein crystallography and allowing us to send out protein crystals along with the Corbett lab to be diffracted at the beamtime in Argonne National Labs. I would like to thank Dr. Xuemei Huang for teaching me how to run my protein samples on the 600mHz and 800mHz NMR spectrometer. I would also like to thank Dr. Stanley Opella, Dr. Sang Ho Park and Dr. Kyle Berg for their help in aspects involving selective labeling expression and protein NMR analysis. This work is being prepared to be submitted titled “Investigations of the 55kDa protein fascin-1 and its small molecule binders by solution NMR”.

Chapter 5 : Screening and development of small molecules that bind to fascin

5.1 Introduction

Fascin, an actin bundling protein, is implicated in numerous cellular processes, including the formation of filopodia and invadopodia[39,62]. Several compounds, such as G2 and its analogs, have been reported to target fascin and inhibit its actin-bundling [79,81–83]. However, till date, very few ligands are reported to have an agonistic effect on fascin's actin bundling activity– among these are the oligo derivative of Benzothiazole Anilines (BTA).

Previous research in the Yang lab demonstrated that the BTA compounds improve memory and learning in both WT mice and transgenic mouse for AD[20,28]. These behavioral improvements were accompanied by significant increases in dendritic spine density in hippocampal neurons[27,28]. Similar increases in dendritic spine density were observed with other BTA derivatives such as BTA-EG_6, BAM-1, BAM2, BAM3-EG_6[27]. This contrasts with G2, which showed no effect on dendritic spine density in primary neurons. This functional and mechanistic uniqueness suggests distinct binding sites which could lead to differences in the mechanism of action for these BTA compounds upon binding to fascin.

In the present study, in collaboration with Dr. Geoffray Leriche (in the Yang lab), we generated and synthesized a library of BTA analogs with different functional scaffolds (Figure 5.1) to explore their binding affinity and specificity towards fascin, with the aim of identifying compounds that could serve as effective therapeutic agents.

5.2 Thermal shift assay for screening BTA analogs

To screen the synthesized library of BTA analogs, I employed a thermal shift assay. This method measures the melting temperature of a protein (Tm), which is the temperature at which there is 50% denaturation. Protein denaturation is monitored via an increase in fluorescence of SYPRO orange dye which binds to hydrophobic residues that get exposed as the target protein unfolds[128]. Compound binding to the target protein possibly leads to increased stability and an increase in the melting temperature. The library of 13 BTA analogs that share components with BTA-EG_6, allowed us to assess the effects of different structural changes and their impact on binding to fascin. Thioflavin T was used as a negative control for this study.

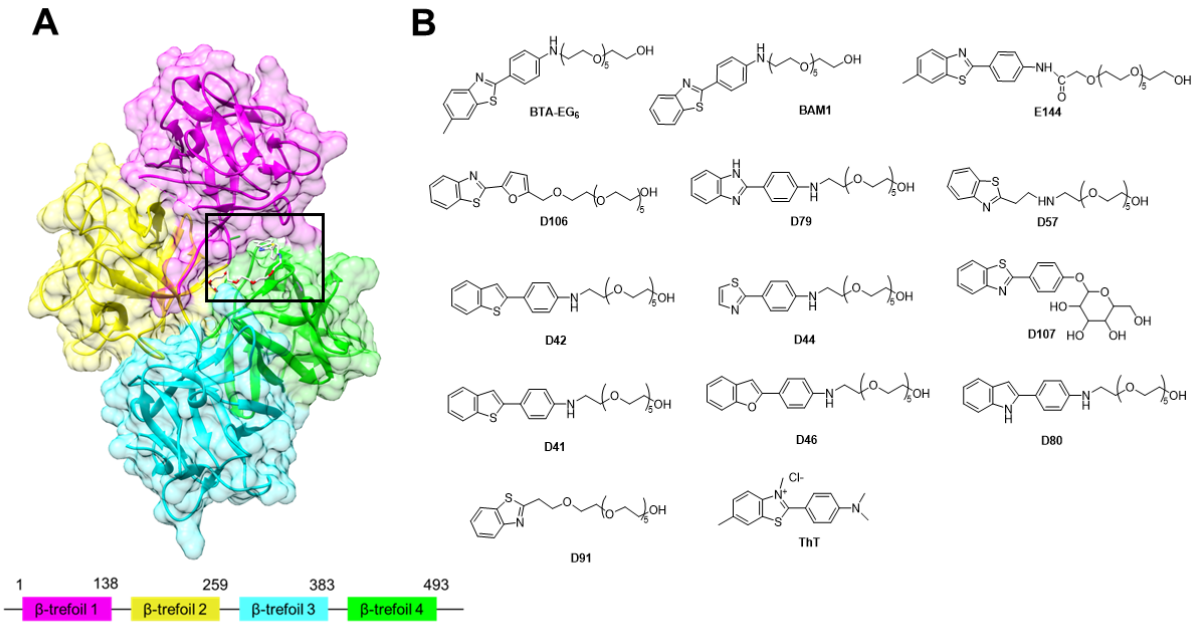


Figure 5.1: A) Docked pose of BTA-EG_6 to the site between β trefoil 1 and 4 of fascin. **B)** Library of compounds used in the thermal shift screening assay.

An average Tm value of 60.2°C ± 0.3°C. was obtained for unbound fascin as reference for determination of the change in Tm upon compound binding. The results of the thermal shift assay with the library of 15 compounds (including BTA-EG_6 and ThT) are summarized in Table 5-1.

Table 5-1: Results from the thermal shift screening assay.

Compound	Conc. (mM)	Tm (°C)
Free fascin	-	60.2 ± 0.3
BTA-EG_6	1	62.7 ± 0.2
BAM-1	1	61.5 ± 0.1
E144	1	64.2 ± 0.1
D90	1	53.2 ± 0.2
D106	1	60.7 ± 0.1
D79	1	61.7 ± 0.3
D57	1	60.5 ± 0.1
D42	1	61.8 ± 0.2
D44	1	60.1 ± 0.2
D107	1	60.2 ± 0.1
D41	1	63.2 ± 0.3
D46	1	63.1 ± 0.2
D80	1	63.6 ± 0.3
D91	1	60.9 ± 0.1
ThT	1	60.6 ± 0.2

Some compounds resulted in distorted thermal unfolding profiles from which reliable Tm values could not be extracted, probably due to compound interference with the SYPRO orange fluorescence signal used in the assay, highlighting the need for additional assays to confirm binding. Within those that could be analyzed, I only looked

at molecules that had a similar or greater effect on Tm than what was observed with BTA-EG_6. Among these hits, molecule E144 resulted in the highest significant increase in Tm along with molecules D41, D42 and D80, suggesting specific binding to fascin and greater stabilizing effect on fascin's Tm (Figure 5.2).

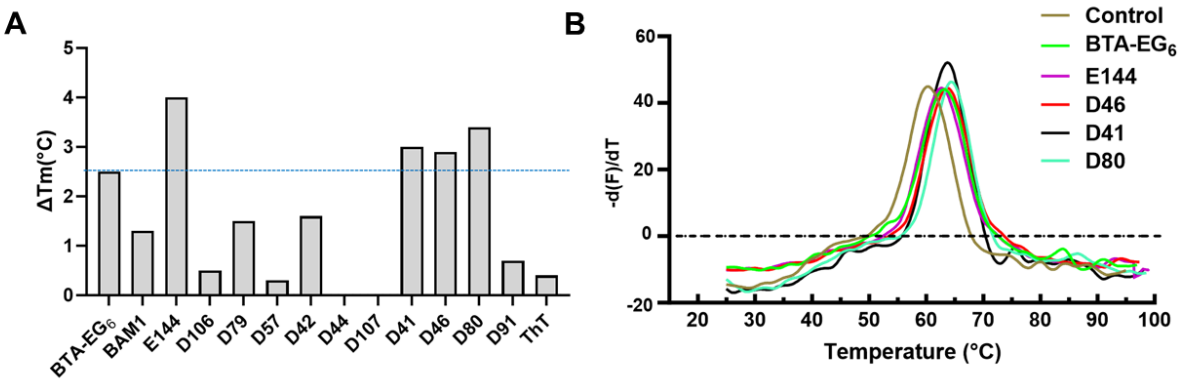


Figure 5.2: A) Summary of changes in Tm of fascin induced by the presence of small molecules. **B)** First derivative of the thermal denaturation profiles (average from 4 runs) of selected hits from the thermal shift screening assay.

5.3 Binding studies with hits from the thermal screening assay

To investigate the relationship between Tm and binding affinity (K_d), and to further validate the binding of identified hits, I carried out ITC studies similar to what was discussed in the previous chapters. Among the four tested compounds, only E144 displayed a significantly better binding affinity to fascin compared to BTA-EG_6 (Figure 5.3) Compound D80 also showed an improved binding affinity, although it was not statistically significant. The binding interactions of these compounds with fascin revealed a higher entropic contribution compared to BTA-EG_6, indicating a potential difference in the binding mode. Further ITC studies with compounds D42, D79 and BAM1, which were initially screened out, confirmed that they had lower binding affinities compared to BTA-

EG_6. The correlation between Tm and binding affinity (K_d) was robust (Figure 5.3C), supporting the use of thermal shift assays as a preliminary screening tool for binding/stabilization events.

A

Molecule	Binding Affinity	Kd (μM)	ΔH (kJ/mol)	ΔS(J/mol·K)	ΔG(kJ/mol)
BTA-EG_6	-	4.8 ± 0.7	-20.9 ± 1.7	31.8 ± 7.2	-30.4 ± 3.9
D80	No Change	3.9 ± 0.3	-5.4 ± 1.2	85.3 ± 5.6	-30.8 ± 1.2
E144	Increase	1.5 ± 0.5	-6.3 ± 0.9	90.2 ± 6.4	-33.1 ± 0.7
D46	Decrease	6.4 ± 0.4	-5.4 ± 0.8	81.3 ± 4.6	-29.6 ± 1.2
D41	Decrease	7.2 ± 0.5	-5.7 ± 1.1	79.3 ± 3.6	-29.3 ± 2.3
D42	Decrease	8.5 ± 0.5	-9.5 ± 1.5	65.2 ± 4.9	-28.9 ± 2.1
D79	Decrease	12.6 ± 0.2	-12.1 ± 2.1	53.2 ± 6.4	-27.9 ± 1.5
BAM1	Decrease	14.7 ± 0.7	-17.8 ± 2.5	32.8 ±2.4	-27.5 ± 1.4

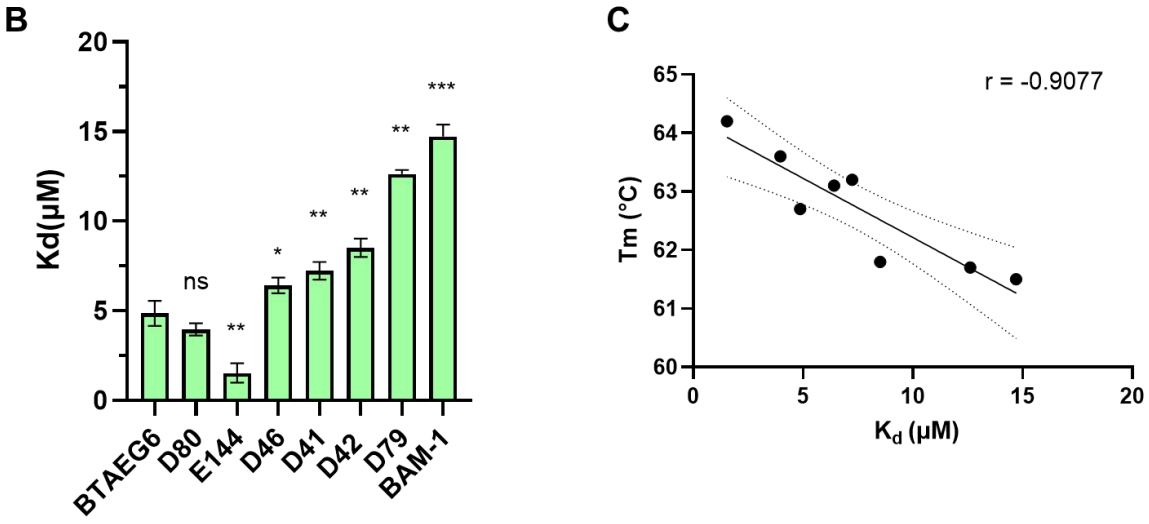


Figure 5.3: A) Summary of binding affinity data for all the BTA analogs with fascin as calculated by ITC measurements. **B)** Graphical representation of binding affinities of selected small molecules to fascin. **C)** Correlation graph between Tm and K_d data. Statistical analysis was performed using a two tailed Welch's *t*-test. (*p<0.05, **p< 0.01, ***p<0.001, n=3 for each molecule)

5.4 Molecular docking studies

Molecular docking studies were conducted to understand the binding interactions of BTA analogs E144, D80, D41 and D46 with fascin and to compare their conformational poses with that of BTA-EG$_6$. The top docked poses for each molecule looked very similar to that of BTA-EG$_6$. BTA-EG$_6$ has been proposed to interact with residue R389 via an H-bond and form hydrophobic contacts with residues A137, G393 and I45 (Figure 5.4A). Similar contacts were seen for compound E144 with an additional contact being formed with H65 and the benzene ring which could possibly account for its higher binding affinity to fascin (Figure 5.4B). Similarly, D80 had contacts with R389, I45, A137 and G393 but the contact with H65 was not seen in this case (Figure 5.4C). Top poses of D41 (Figure 5.4D) and D46 (Figure 5.4E) show the loss of interaction with R389 which may explain their lower binding affinity with fascin compared to that of BTA-EG$_6$.

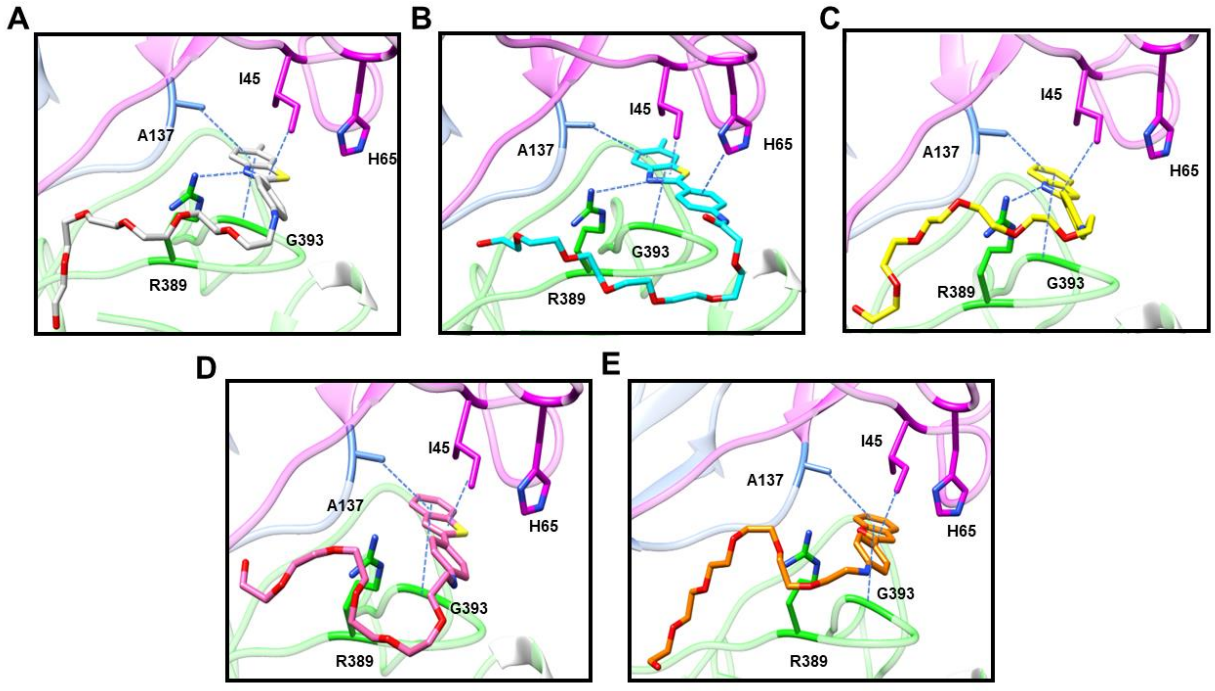


Figure 5.4: Results from molecular docking of BTA analogs to the proposed binding site on fascin between β trefoil 1 and 4. **A)** BTA-EG$_6$ (white) **B)** E144 (cyan) **C)** D80 (yellow) **D)** D41 (pink) **E)** D46 (orange)

5.5 *In vitro* and *in vivo* activity of BTA analogs

I then assessed the functional effects of these compounds by carrying out a slow speed sedimentation assay to measure the actin bundling activity of fascin in the presence of identified BTA analogs – E144, D80, D41 and D46. As discussed previously, BTA-EG_6 was found to increase the actin bundling activity of fascin. Similarly, all the four BTA analogs also significantly enhanced fascin's actin bundling activity, surpassing the effects observed with BTA-EG_6 (Figure 5.5). In contrast, other molecules – D42, D79 and BAM-1 did not exhibit significant changes in actin bundling of fascin compared to the control samples (no molecule).

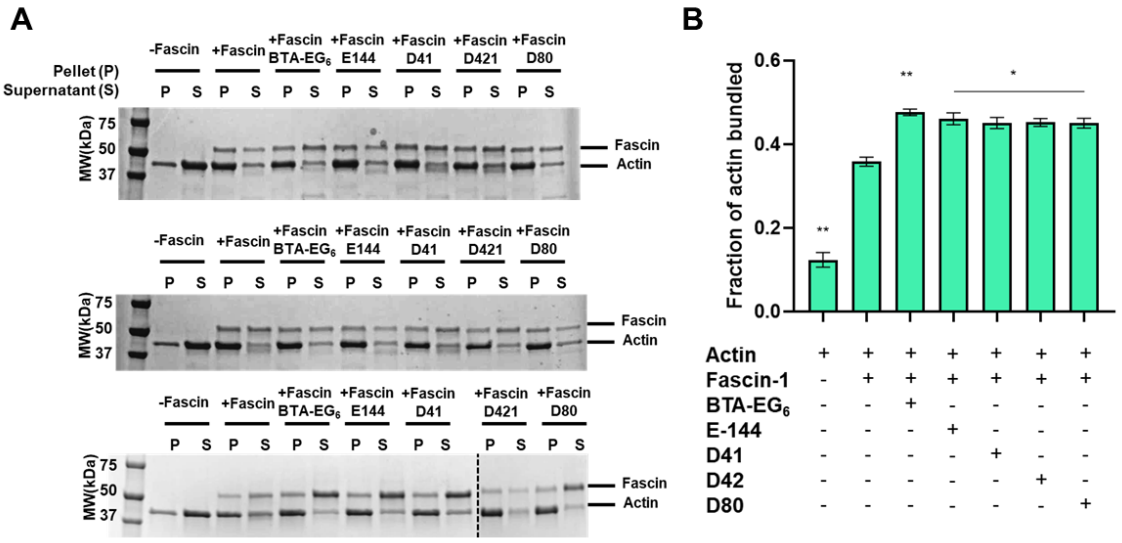


Figure 5.5: Investigation of the effects of BTA analogs on the bundling of actin filaments. **A)** Representative gels of actin in bundles (P) versus unbundled (S). **B)** Quantification of the gel in (a) showing the fraction of actin filaments in bundles after various treatments. Statistical analysis was done by two tailed Welch's *t*-test (*p<0.05, **p<0.01) for n=3 and reflect comparisons of actin bundling with respect to fascin and actin alone (without any compound).

Next, in collaboration with Dr. Lara Dozier of Patrick lab, we carried out spine density analysis of primary hippocampal neurons in the presence of these compounds to

assess. We wanted to assess if the effects seen *in vitro* would be translated into the phenotype observed with BTA-EG$_6$. Lara treated (molecule or control) and fixed the neurons while I took images and analyzed them in a blinded fashion. Not until the analysis was complete was the identity of each sample treatment revealed.

Neurons were analyzed through image analysis as previously described[87]. Secondary dendritic shafts were selected using the straiten macro[75], then cropped to 30 µm segments. Dendritic spines along the dendritic shaft were measured manually and counted using a spine counting macro developed in the Patrick Lab. Previously, we found that BTA-EG$_6$ significantly increases the spine density in primary neurons. Of these 4 molecules, only D80 and E144 significantly increased spine density, mirroring the effects of BTA-EG$_6$. Other molecules such as D46, D41, D42 and D79 did not show any difference in spine density when compared to the control (no treatment) samples. Only BAM1 showed a significant increase in spine density compared to the control sample, a result previously reported in the Yang lab[27] (Figure 5.6).

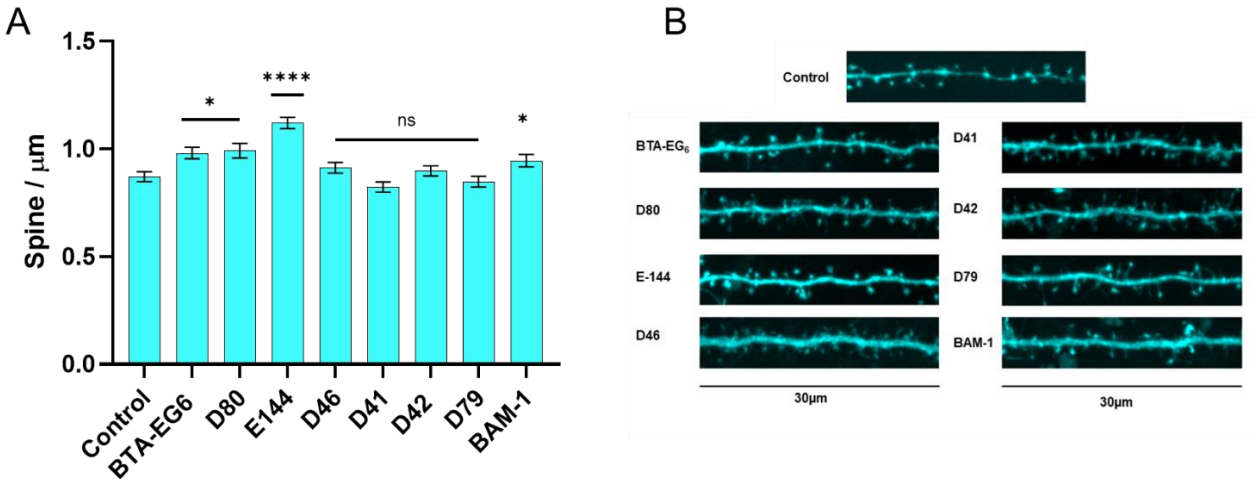


Figure 5.6: A) Spine density measurements in primary neurons upon treatment with BTA analogs. **B)** Representative 30 µm dendritic segments selected for dendritic spine analysis. Statistical analysis was performed using two tailed Welch's *t*-test (*p<0.5, ****p<0.001). *N* = 60 dendritic segments per treatment.

5.6 Conclusion

In summary, this chapter details the identification and characterization of several BTA analogs with different structural scaffolds that bind to fascin and enhance its actin bundling activity. Among these analogs, only E144 emerged as a particularly promising candidate, demonstrating superior binding affinity and functional activity compared to BTA-EG_6. These findings not only support the existence of a novel binding site on fascin for BTA compounds but also provide a foundation for the development of therapeutic agents targeting fascin in neurodegenerative diseases.

5.7 Methods

Expression and purification of WT fascin

The expression and purification of WT fascin was carried out as previously discussed in Chapter 3 of this dissertation.

Isothermal Titration Calorimetry

Calorimetric measurements were carried out using a Low Volume ITC instrument as described previously in Chapter 3 of this dissertation.

Computational docking studies

All steps for the docking experiments were carried out using Schrodinger suite (2019-20), as previously described in Chapter 3 of this dissertation. The images of docked posed were generated using Chimera[98].

Slow speed actin sedimentation assay

F-actin bundling activity by fascin in the presence of BTA analogs was measured by a slow-speed centrifugation assay as described previously in Chapter 2 of this dissertation.

Spine density analysis

Spine density analysis including preparation, maintenance of primary neurons and analysis was carried out as previously described in Chapter 2 of this dissertation.

Thermal shift assay

Thermal shift assay was performed using a Biorad C1000 Touch Thermal Cycler CFX96 RTPCR system in a 96-well format as described previously[82]. A total of 25µL reaction mixture was set up containing 2µM fascin in 20 mM HEPES, 150 mM NaCl, 1mM DTT, at pH 7.4, in the presence of SYPRO orange (1,000-fold dilution from the commercial stock [Invitrogen]). The indicated compounds, prepared at 10 mM were added to each well to a final concentration of 1mM. The reaction was carried out in replicates of 4 per compound, along with internal controls which contained only free protein. The PCR plates were covered and subsequently shaken, centrifuged, incubated for 2 min at 20ºC inside the RT-PCR machine, and heated from 20ºC to 100ºC at a 1ºC/min scan rate.

5.8 Acknowledgements

I would like to thank Dr. Lara Dozier and Professor Gentry Patrick for their invaluable support for the spine density work. Dr. Lara Dozier maintained and treated the primary neurons used in this study. Special thanks to Professor Seth Cohen for giving me access to their thermal cycler instrument. This work is in preparation for submission in a research article entitled “Screening and development of small molecules that target Fascin-1”.

Part II: Design novel AMPKβ1 selective activators for IBD

Chapter 6 : Introduction

6.1 Inflammatory Bowel Disease

Inflammatory bowel disease (IBD) is a chronic, relapsing condition of the gastrointestinal (GI) tract[129] that encompasses two main types: Crohn's disease[130] and ulcerative colitis[131]. Globally, the prevalence of IBD has been increasing, posing significant health challenges. IBD is characterized by prolonged inflammation of the GI tract, which leads to symptoms such as severe abdominal pain, persistent diarrhea, fatigue, and weight loss[132]. While Crohn's disease can affect any part of the GI tract, often in a patchy distribution, ulcerative colitis is typically limited to the colon and rectum [131,132].

The etiology of IBD is not fully understood; however, it is believed to result from a complex interplay of genetic predisposition, environmental factors such as diet, smoking, and antibiotic use, and dysregulation of the immune system[129]. Genetic studies have identified several risk factors associated with IBD, indicating a hereditary component, while environmental factors could trigger or exacerbate the condition in genetically predisposed individuals[129].

IBD significantly impacts patients' quality of life due to its chronic and often unpredictable nature. The economic burden of IBD is substantial, involving both direct healthcare costs and indirect costs related to lost productivity[133]. Current therapies for IBD aim to induce and maintain remission, alleviate symptoms, and improve quality of life. These include amino salicylates (5-ASA)[134], corticosteroids[135], immunosuppressants like azathioprine[136] and methotrexate[137], and biologics such as infliximab[138] and adalimumab[139], which target specific components of the immune response. Despite these

options, many patients with complications or those who do not respond to medical therapy opt for surgery. Surgery can be curative for ulcerative colitis (total colectomy) but is not curative for Crohn's disease, as it can recur elsewhere in the GI tract [140,141]. Despite these therapeutic options, many patients experience incomplete response or adverse effects, with approximately 40% of patients becoming unresponsive within a year[142,143], highlighting the need for new therapeutic targets and more effective treatments.

6.2 Identification of AMPK as a target for IBD

Our collaborators in Pradipta Ghosh's lab at the Department of Cellular and Molecular Medicine are addressing the challenge of drug discovery for IBD by focusing on drugs that augment or protect the intestinal barrier using advanced artificial intelligence (AI) methodologies[144]. Disruption of the gut barrier has been implicated in the pathogenesis of multiple chronic illnesses that are characterized by chronic gastrointestinal inflammation – this includes IBD, a complex, multi-factorial, autoimmune disorder of the gut with diverse components[145–150].

The Ghosh lab used an AI-assisted approach which involved comprehensive unbiased transcriptome analysis of RNA sequencing (RNA-seq) data collected from human IBD patients and experimental models to uncover key molecular targets implicated in the pathogenesis of IBD[144]. They identified genes that were significantly upregulated or downregulated in IBD compared to healthy controls. They used AI algorithms, including machine learning models, to analyze these data, prioritizing genes based on their relevance to disease progression and potential as therapeutic targets[144]. The resultant models integrated various layers of biological information, including gene expression,

interaction networks, and functional annotations. This integrative approach led to the identification of a previously unknown target PRKAB1, the gene encoding the AMPKβ1 subunit, as a crucial regulator of gut barrier function and inflammation in IBD[144] (Figure 6.1).

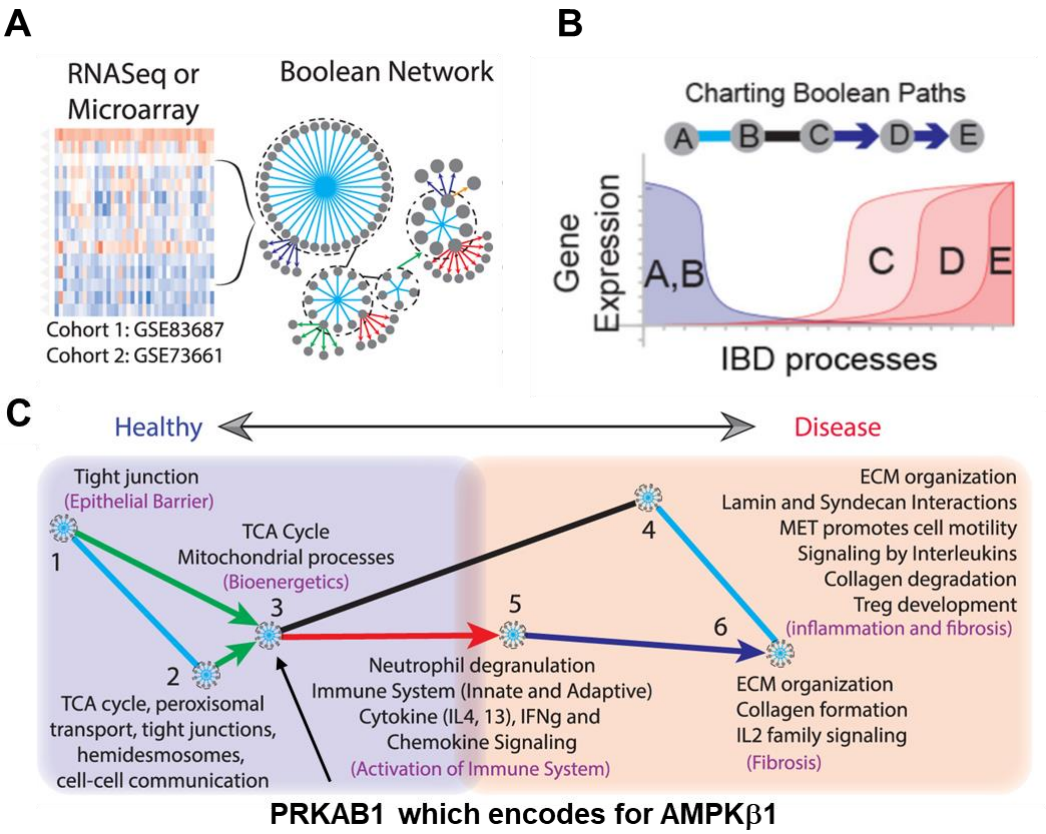


Figure 6.1: A) Boolean Network Explorer (*BoNE*) used to analyze two IBD datasets and form Boolean clusters containing genes having similar expression profiles. **B)** Schematic illustrating how Boolean cluster relationships are used to chart disease paths (top); and individual gene expression changes along a Boolean path, illustrating gene expression dynamics within the normal to IBD continuum (bottom). **C)** Reactome pathway analysis of each cluster to identify the signaling pathways and cellular processes that are enriched during IBD progression. Figure reproduced from Sahoo *et. al*[144].

6.3 AMPK – master regulator of cell homeostasis

AMP-activated protein kinase (AMPK) is a key regulator of cellular homeostasis [151]. It is a highly conserved heterotrimeric serine/threonine kinase composed of three subunits:

a catalytic α subunit and two regulatory subunits, β and γ. Each subunit has multiple isoforms (α1, α2; β1, β2; γ1, γ2, γ3), which allows for a variety of possible combinations, adding to the complexity and functional specificity of the enzyme [151,152].

The N-terminal region of the α subunit contains the kinase domain, which is responsible for the enzyme's catalytic activity. This domain includes the critical threonine residue (Thr172) whose phosphorylation is essential for AMPK activation[152] (Figure 6.2). The β subunit features a central Glycogen Binding Domain (GBD), which allows AMPK to associate with glycogen particles, potentially regulating its activity in response to cellular energy levels[151,152]. The γ subunit is characterized by four cystathionine beta-synthase (CBS) domains that create binding sites for AMP, ADP, and ATP, which regulate AMPK activity by promoting conformational changes[152]. The binding of AMP or ADP to the γ subunit promotes a conformational change that enhances the phosphorylation of Thr172 on the α subunit by upstream kinases such as LKB1 or CaMKK2 thereby activating AMPK[152] (Figure 6.2). This binding also inhibits the action of protein phosphatases that would otherwise dephosphorylate and inactivate AMPK[151,152].

AMPK activation promotes catabolic pathways that generate ATP, such as fatty acid oxidation and glycolysis, while inhibiting anabolic processes that consume ATP, like lipid and protein synthesis (Figure 6.2). During cellular stress, AMPK activation ensures energy balance and survival by optimizing energy production and reducing energy expenditure. AMPK is activated by an increase in the AMP/ATP ratio, which occurs during cellular energy stress, such as hypoxia, exercise, or glucose deprivation[151,152]. In addition to promoting Thr172 phosphorylation, AMP binding also causes a direct allosteric activation of AMPK, further increasing its activity.

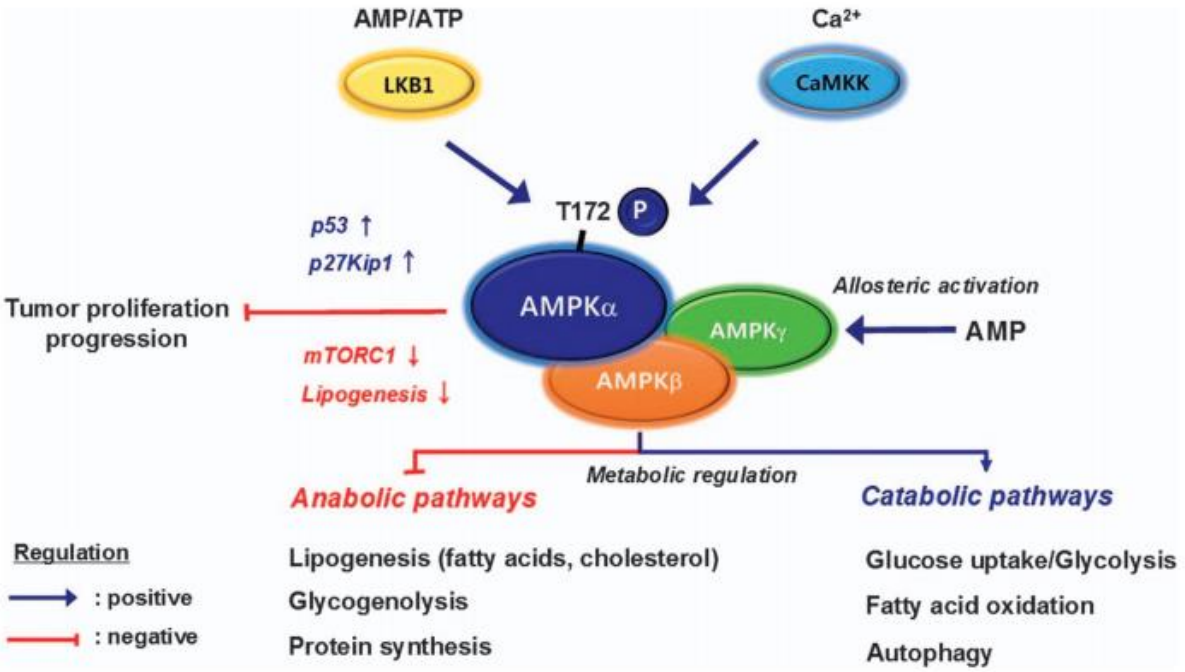


Figure 6.2: Summary of the physiological roles of AMP-activated protein kinase (AMPK). Figure reproduced from Kim *et al*[152].

6.4 AMPK – role and function in stabilization of the gut barrier

AMPK's role (or the role of its agonists) in protecting and stabilizing the gut barrier has been evaluated and well established in several murine models of colitis[153–158] and adoptive T-cell transfer model[159]. In the context of IBD, AMPK's functions extend beyond energy regulation to include critical roles in maintaining gut barrier integrity and modulating inflammatory responses. AMPK activation inhibits the NF-κB signaling pathway, which is a key mediator of inflammatory responses[160]. This results in reduced production of pro-inflammatory cytokines (e.g., TNF-α, IL-6, IL-1β). By dampening the inflammatory cytokine production, AMPK helps in mitigating chronic inflammation associated with IBD [161].

AMPK enhances the assembly and function of tight junction proteins, which are crucial for maintaining the integrity of the intestinal epithelium. This prevents the leakage of luminal antigens and bacteria that can trigger immune responses. Improved tight junction integrity under AMPK activation reduces gut permeability, thereby protecting the gut barrier and preventing the onset of inflammation[162].

AMPK induces autophagy, a cellular process that degrades and recycles damaged organelles and proteins. This process is protective in intestinal epithelial cells, reducing inflammation and maintaining cellular homeostasis. Enhanced autophagy under AMPK activation helps in preserving the barrier function by removing damaged cells and promoting epithelial cell survival[163,164].

The detailed structural understanding of AMPK, its activation mechanisms, and its role in cellular energy homeostasis provide a solid foundation for developing novel therapeutic strategies for conditions like IBD. The identification of PRKAB1 gene as a therapeutic target underscores the potential of AMPK modulation in IBD treatment.

6.5 Overview of approach and methodology

By targeting AMPK, particularly the β1 subunit, this study aims to harness the multifaceted roles of AMPK to develop novel therapeutics for IBD that not only address inflammation but also could possibly restore and maintain gut barrier integrity. Effects of repairing the gut epithelial barrier through AMPKβ1 activation have already been tested, observed, and validated by our collaborators in the Ghosh lab with a known, β1-specific agonist, PF-06409577[144].

The work carried out in this part of the dissertation aims to design and develop novel molecular candidates with improved potency that could enhance AMPK activity,

especially through selective activation of the AMPKβ1 subunit. The two methodologies being discussed in this part of the dissertation for developing AMPKβ1 selective activators are:

i) **Synthetic route**: This route involved the design and synthesis of novel compounds based on a pharmacophore model specific to AMPKβ1. The pharmacophore model uses existing crystallographic data of known binders of AMPK to assess the binding pocket of AMPK and design molecules that selectively bind to and activate the AMPKβ1 subunit, possibly enhancing its beneficial effects on gut barrier function and inflammation control.

ii) ***In silico* route**: This route leverages computational methods to identify potential AMPKβ1 selective activators from large libraries of commercially available small molecule ligands. This approach is efficient and cost-effective, allowing for the rapid identification of promising candidates or different scaffolds for further experimental validation.

By combining these methodologies, we seek to develop highly selective AMPKβ1 activators that can effectively treat IBD. The synthetic route would allow for the tailored design of new molecules, while the *in silico* screening provides a high-throughput approach to identify promising candidates from existing compound libraries.

Chapter 7 : Development and screening of AMPKβ1 selective ligand

7.1 Introduction

Several small molecule AMPK ligands have been previously reported[152,165,166]. One of the activators of the α1β1γ1 isoform of AMPK is PF-06409577 (hereafter referred as PF) with an *in vitro* EC_{50} in the nanomolar range and weakly active on others isoforms α1β2γ1, α2β2γ1, and α2β2γ3 of AMPK[167]. Availability of a co-crystal structure of AMPKβ1 bound to PF[167] and the evidence that PF compound helps in repairing the gut epithelial barrier through AMPKβ1 activation[144] (previously reported in the Ghosh lab), made PF compound a good candidate to be used as a starting point for the design and synthesis of potent and selective AMPK-targeting agents for the treatment of IBD. The focus of this study is to explore new design criteria for increasing the potency and aqueous solubility of the ligand without losing the selectivity to AMPKβ1. Selectivity is crucial to minimize off-target effects and maximize therapeutic efficacy. In this study, I have employed computational and experimental techniques to discover and validate potential drug candidates for AMPKβ1 activation.

7.2 Development of a pharmacophore model for AMPK ligands

Understanding the structure of AMPK is crucial for the design of selective activators and inhibitors. Structural insights can guide the development of small molecules that can modulate AMPK activity by targeting specific subunits or regulatory sites. To gain insights into the molecular determinants of AMPK ligands that lead to good selectivity and binding, I first developed a pharmacophore model. A pharmacophore is a theoretical representation of the spatial arrangement of features in a molecule that are

necessary for its biological activity[168]. It serves as a template to identify the key features required for binding and selectivity to the target active site. This model is crucial in drug discovery as it incorporates information from existing co-crystal structures of the receptor proteins with various ligands and provide detailed insights into the binding interactions between the target protein and its activators or inhibitors.

The co-crystal structure AMPKβ1 bound to PF compound revealed several non-covalent contacts between the PF compound and amino acid residues K29, K31, and D88 within the binding pocket that can be utilized for specific binding to this AMPK isoform (Figure 7.1). On closer inspection, I also found other untapped residues such as R83, N48 which could be utilized for novel compounds to increase the binding interaction to AMPKβ1.

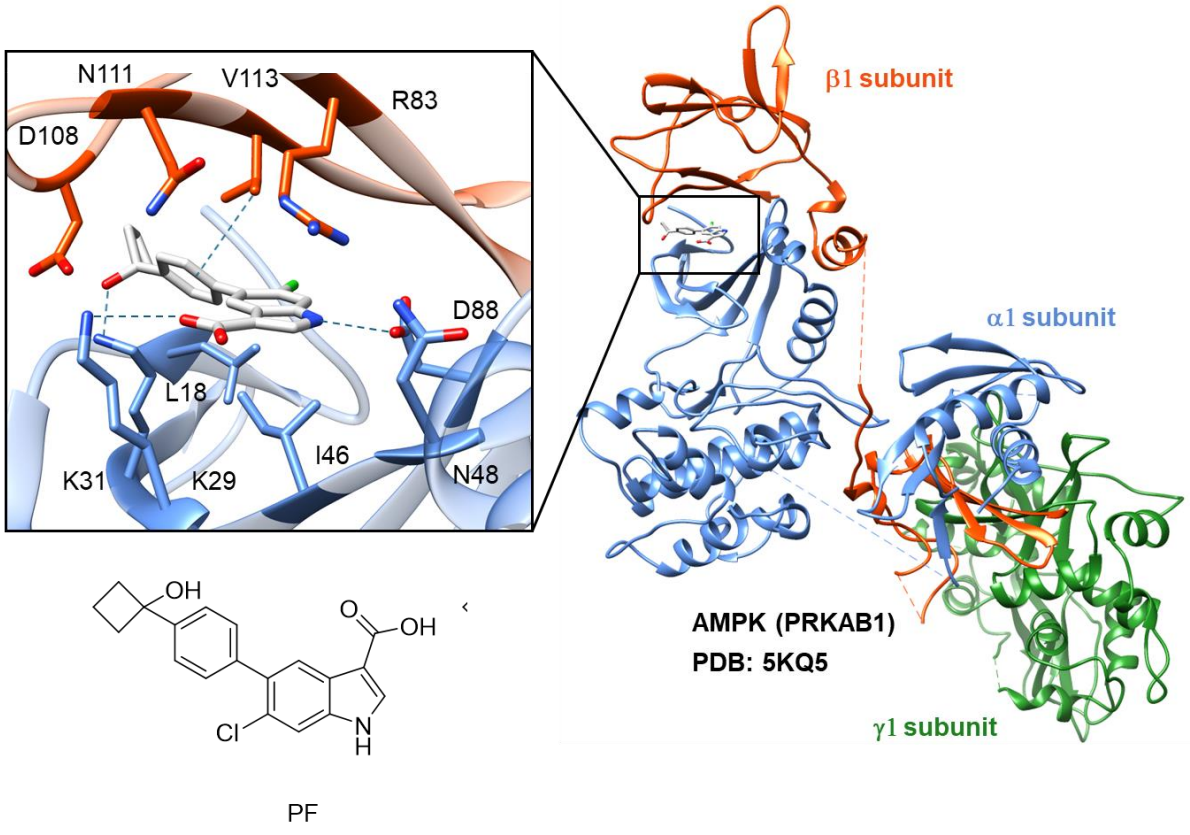


Figure 7.1: Analysis of binding site of PF compound in the crystal structure of AMPKβ1 PDB: 5KQ5[167].

To develop a pharmacophore model for AMPK, I analyzed other existing X-ray co-crystal structures of AMPK in complex with known and selective β1/β2 ligands[167,169,178–180,170–177]. I investigated the binding site to identify critical residues and interactions such as hydrogen bonds, hydrophobic contacts, and electrostatic interactions. Next, for known AMPK ligands[152,166,181](selected based on their reported activity towards AMPK) whose co-crystal structures were not available, I carried out molecular docking studies to provide insights into their binding modes with AMPKβ1 isoform. These ligands served as additional reference for the pharmacophore model.

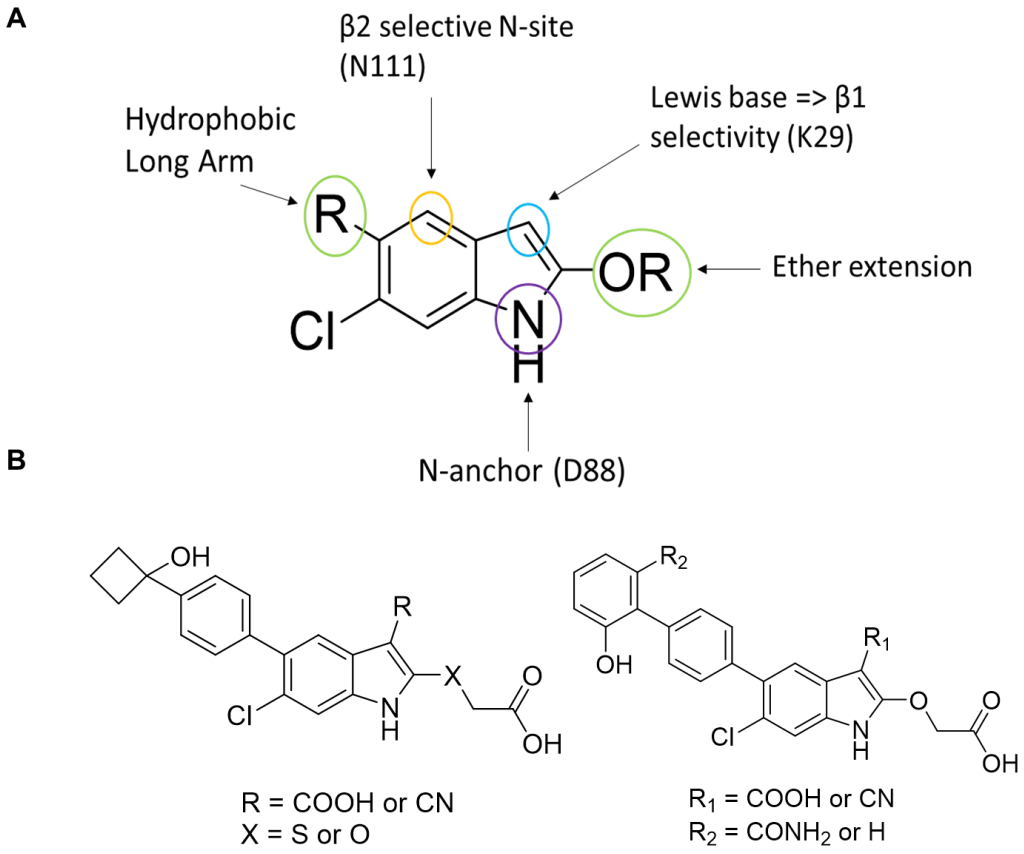


Figure 7.2: A) Pharmacophore model for AMPK ligands **B)** Proposed series of compounds based on the computationally designed pharmacophore model.

The resulting pharmacophore model highlighted several essential features: i) a Lewis base site necessary to interact with residue Lys29 which is proposed to be a crucial interaction for β1 binding and selectivity; ii) an anchor residue Asp88 which is proposed to be a crucial residue necessary for binding to both β1/β2 isoforms; iii) a β2 selective site at Asn111 iv) a hydrophobic long arm and an ether extension side, either of which could be modulated to obtain different scaffolds and series of molecules of different lengths and sizes (Figure 7.2A).

Based on the pharmacophore model, in collaboration with another graduate student in the Yang lab, Joseph Sawires, we proposed two sets of molecules with modifications on the indole ring and the hydrophobic long arm (Figure 7.2B). We hypothesized that some of these molecules could have improved binding due to new contacts in the binding pocket with other untapped residues.

7.3 Design and synthesis of novel compounds targeting AMPKβ1

In collaboration with Jospeh Sawires, based on the pharmacophore model, I designed novel analogs of the PF compound (Figure 7.3A). Molecular docking studies of these analogs of the compound with AMPKβ1 suggested that compounds containing a nitrile group at R_1 instead of a carboxylic acid (hereafter referred as PF-CN) could also make use of the same amino acid contacts within the binding pocket as seen with the PF compound (Figures 7.3B and 7.3C). Furthermore, these studies also predict that putatively unutilized arginine (R83) and asparagine (N48) residues located within the binding pocket of AMPKβ1 could be used to further increase binding of ligands by derivatization of compounds PF or PF-CN at R_2 with small substituents (such as a

propanediol group, referred hereafter as compound **1**) that can form hydrogen bonds with R83 and N48 (Figure 7.3D). Such substitutions were also expected to also increase aqueous solubility compared to no substitution at R_2.

Joseph Sawires synthesized compounds PF and PF-CN in the Yang lab but encountered some difficulties in the synthetic route for compound **1**. Since compound **1** is still being synthesized in the Yang lab, I will focus the discussion on compounds PF (used as a positive control) and PF-CN, as well as compounds not derived from PF (discussed in the following sections) for the remainder of this dissertation.

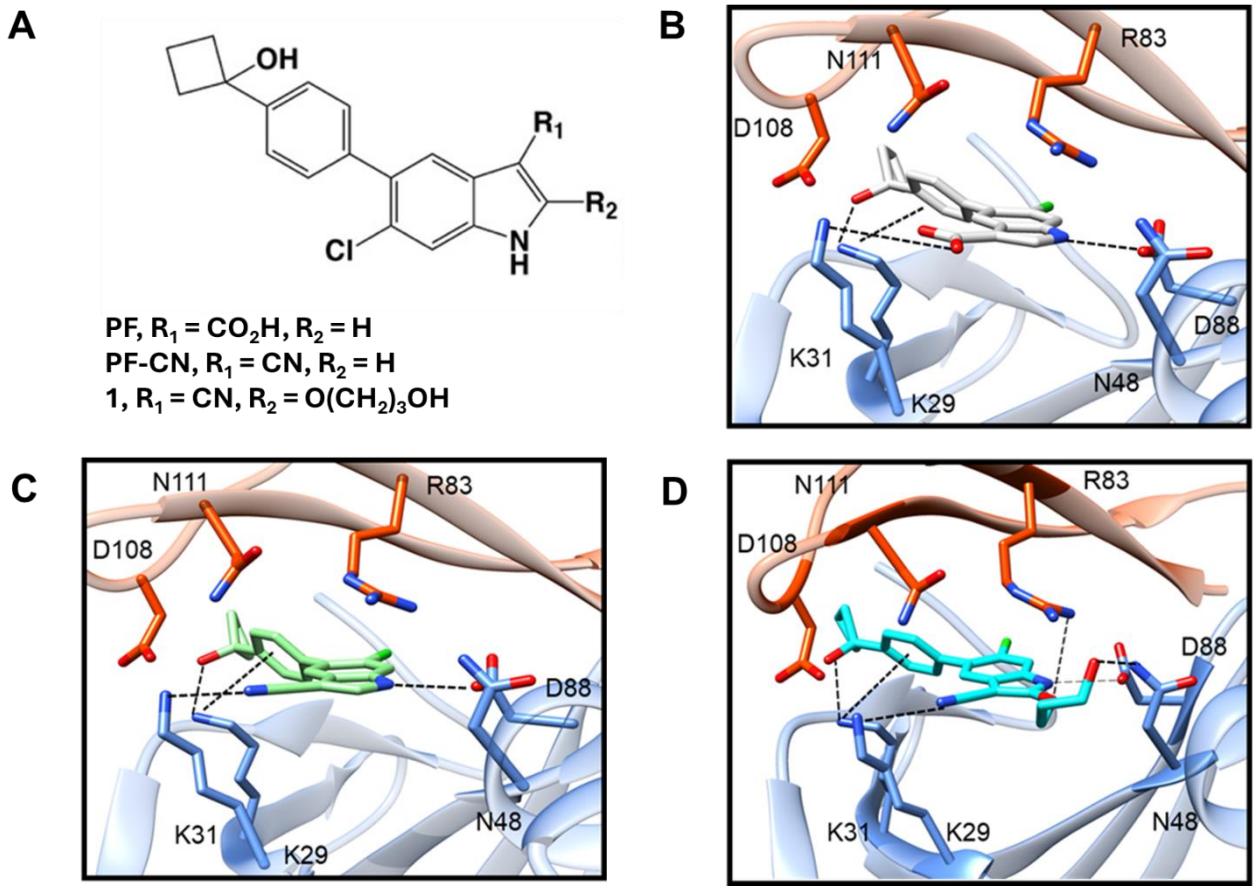


Figure 7.3: Results from molecular docking studies of ligands bound to $\alpha 1\beta 1\gamma 1$ isoform of AMPK. **A)** Chemical structures of PF, PF-CN and compound **1**. **B-D)** Docked poses of compounds PF (white), PF-CN (green) and compound **1** bound to AMPKβ1, respectively.

7.4 *In silico* virtual screening of ligands from NCI datasets

In parallel to developing and synthesizing novel compounds in the Yang lab, I used *in silico* tools to screen other potential lead compounds for AMPKβ1 binding and activation. The method of high throughput virtual screening (HTVS) leverages computational methods to screen ligands from large libraries of commercially available compounds[182,183]. This approach is efficient and cost-effective, allowing for the rapid identification of promising candidates for further experimental validation.

7.4.1 Dataset Selection

The National Cancer Institute (NCI) maintains extensive diversity datasets of commercially available ligands[184]. These datasets are a valuable resource for drug discovery, containing information on the chemical structures and biological activities of thousands of compounds. Compounds in the NCI datasets are filtered based on their physicochemical properties, such as molecular weight, solubility, and lipophilicity, to ensure they are suitable for binding to protein targets[185,186]. I chose this dataset as screening diversity datasets would help us screen for different functional scaffolds for possible lead compounds.

7.4.2 Molecular Docking

Around 8000 compounds from the NCI diversity datasets[184] were virtually screened against the crystal structure of AMPKβ1 using molecular docking. Molecular docking simulations predicted how well each compound fit into the binding site and the

interactions with key residues based on the previously established pharmacophore model. Ligands were scored, ranked and sorted based on their predicted binding affinity and interaction quality. The top 40 compounds from the virtual screening were selected and ordered from the NCI database (Figure 7.4) for further experimental validation in the Yang lab using biochemical assays, focusing on their potential as AMPKβ1 selective activators.

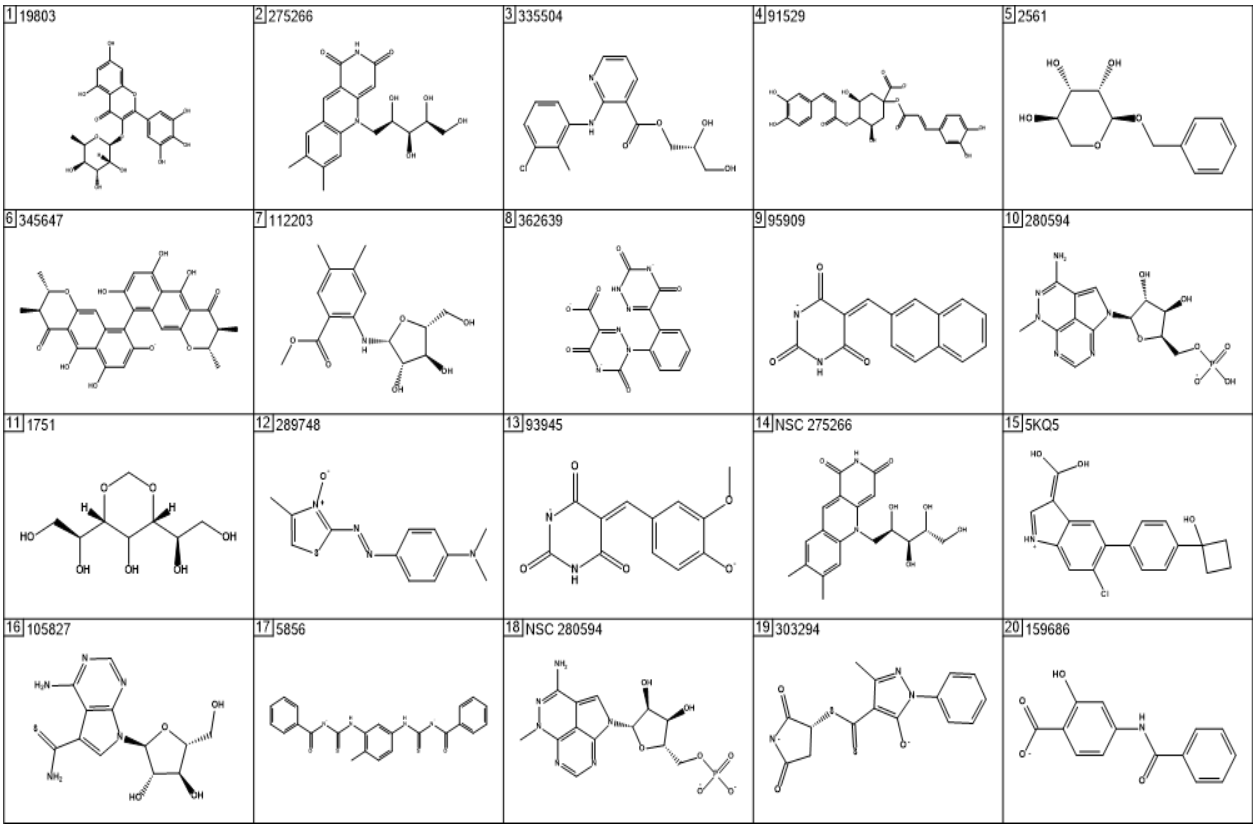


Figure 7.4: Chemical structures of the top 20 compounds from the virtual screen showcasing different functional groups and scaffolds being screened.

7.5 Biochemical assays

7.5.1 Expression and isolation of AMPK proteins

To study the selective activation of AMPKβ1, I first recombinantly expressed and purified different isoforms of AMPK. Plasmids encoding various AMPK isoforms were obtained from Professor Jon Oakhill from St. Vincent's Institute of Medical Research. These plasmids contained the genetic sequences for the α, β, and γ subunits, allowing for the expression of different combinations of AMPK isoforms. I expressed heterotrimeric human AMPK $\alpha 1\beta 1\gamma 1$ and $\alpha 1\beta 2\gamma 1$ as a fusion protein with a histidine tag on the N-terminal in *E.coli* using a pET DUET expression system as previously described[187]. I also expressed other isoforms of human AMPK $\alpha 1\beta 1\gamma 1$ and $\alpha 2\beta 2\gamma 1$ in a similar manner.

Along with the expression of different AMPK isoforms, I also recombinantly expressed CaMKK2 (calcium/calmodulin dependent protein kinase 2), a known downstream activator of AMPK[152,188]. Since the recombinantly expressed AMPK is not active, I needed to activate (phosphorylation at Thr172) it in solution by incubating with CaMKK2 in the presence of AMP. I received the CaMKK2 plasmid as a fusion protein with a GST tag on the N-terminal and a histidine tag on the C-terminal from Professor Jon Oakhill. CaMKK2 was expressed in *E. coli* using a pGEX expression system as previously described[189].

Purification protocols for both AMPK proteins and CaMKK2 were carried out using similar protocols. After harvesting the cells, pellets were lysed by sonication to extract the expressed fusion proteins. The cell lysates were then subjected to centrifugation to remove debris and obtain clear protein extracts. The target proteins (AMPK isoforms and CaMKK2) were purified using a Nickel-NTA affinity column. The purity and integrity of the

purified proteins were assessed using SDS-PAGE and Western blotting (Figure 7.5). After purification, AMPK proteins were pooled and activated by CaMKK2 in the presence of AMP. After activation, the protein mixture was passed through a S200 Superdex gel filtration column to separate the kinases. These steps ensured that the proteins are suitable for downstream functional assays (Figure 7.5).

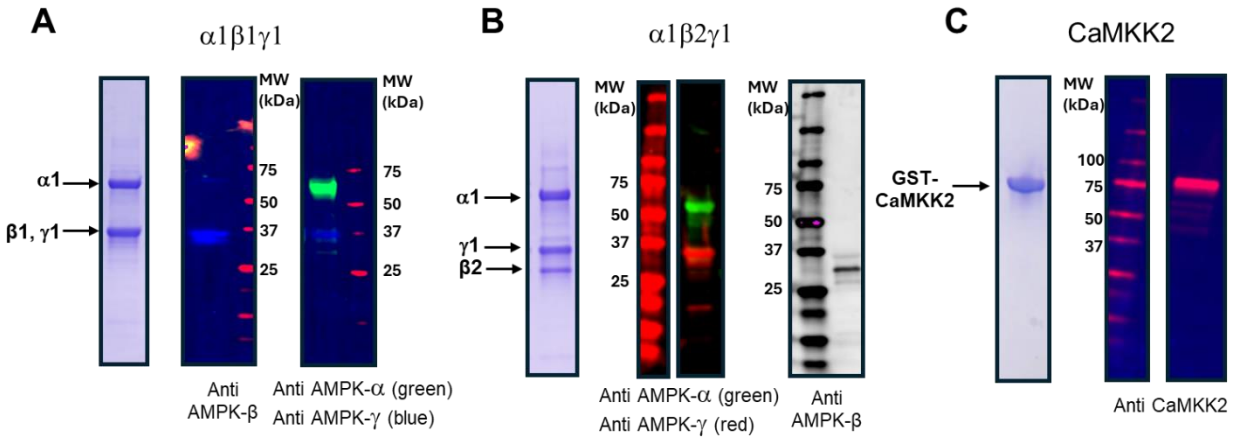


Figure 7.5: Representative coomassie stained SDS-PAGE gels and western blots for AMPK and CaMKK2 proteins. **A)** $\alpha 1\beta 1\gamma 1$ **B)** $\alpha 1\beta 2\gamma 1$ **C)** CaMKK2

7.5.2 Kinase-Glo activity assay

Next, to assess the effects of small molecules screened from the NCI datasets and the novel compounds synthesized in the Yang lab on AMPKβ1 activation, I used a luminescence-based kinase-Glo activity assay[190]. The *in vitro* assay monitors the activity of purified kinases by quantifying ATP. Luminescence signal is inversely proportional to the amount of kinase activity and directly proportional to the ATP present. The kinase assay measures the phosphorylation of SAMS peptide (a known AMPK substrate)[191], by recombinantly expressed and purified AMPK proteins. The reaction is carried out in the presence of ATP which is converted to ADP. Once the reaction is quenched, the

remaining ATP in the reaction mixture is detected as light signal using a luciferase/luciferin detection system (Figure 7.6).

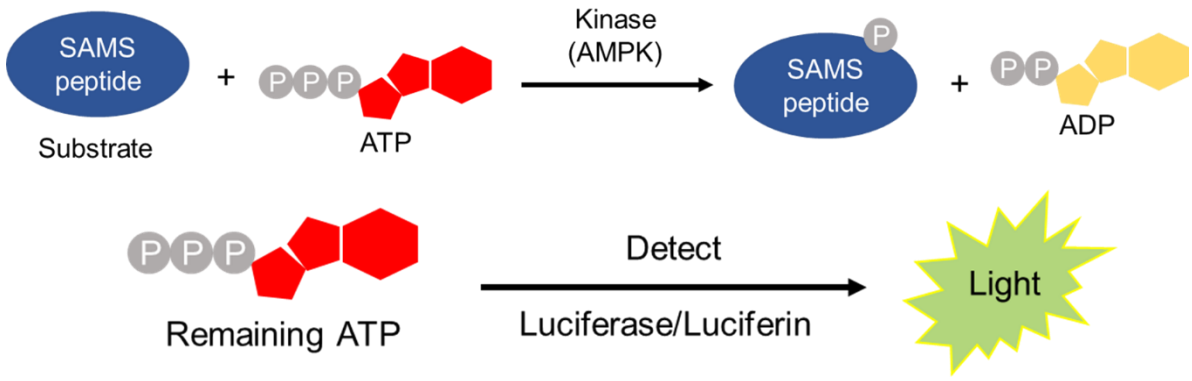


Figure 7.6: Schematic representation of the kinase-Glo assay.

The assay was performed in the presence of small molecules to assess their effects on AMPKβ1 activity and the kinase's ability to phosphorylate its target substrate, indicating its activation status. I used PF compound as a positive control and Staurosporine (a known inhibitor of AMPK's activity)[192] as a negative control for this assay. Of the 40 compounds being tested from the virtual screen, only 11 showed any positive effects on AMPK activation, with PF and PF-CN having the biggest effect on increasing the AMPKβ1 activity (Figure 7.7). These 11 hits along with PF-CN were taken further for testing in HeLa cells.

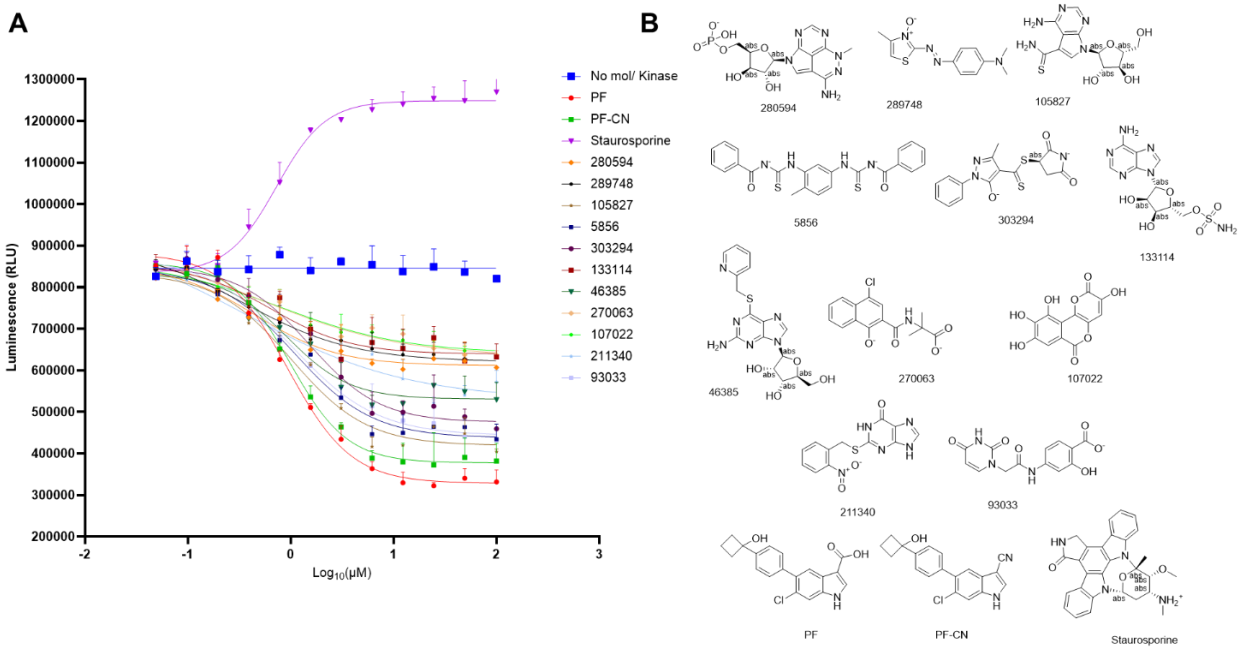


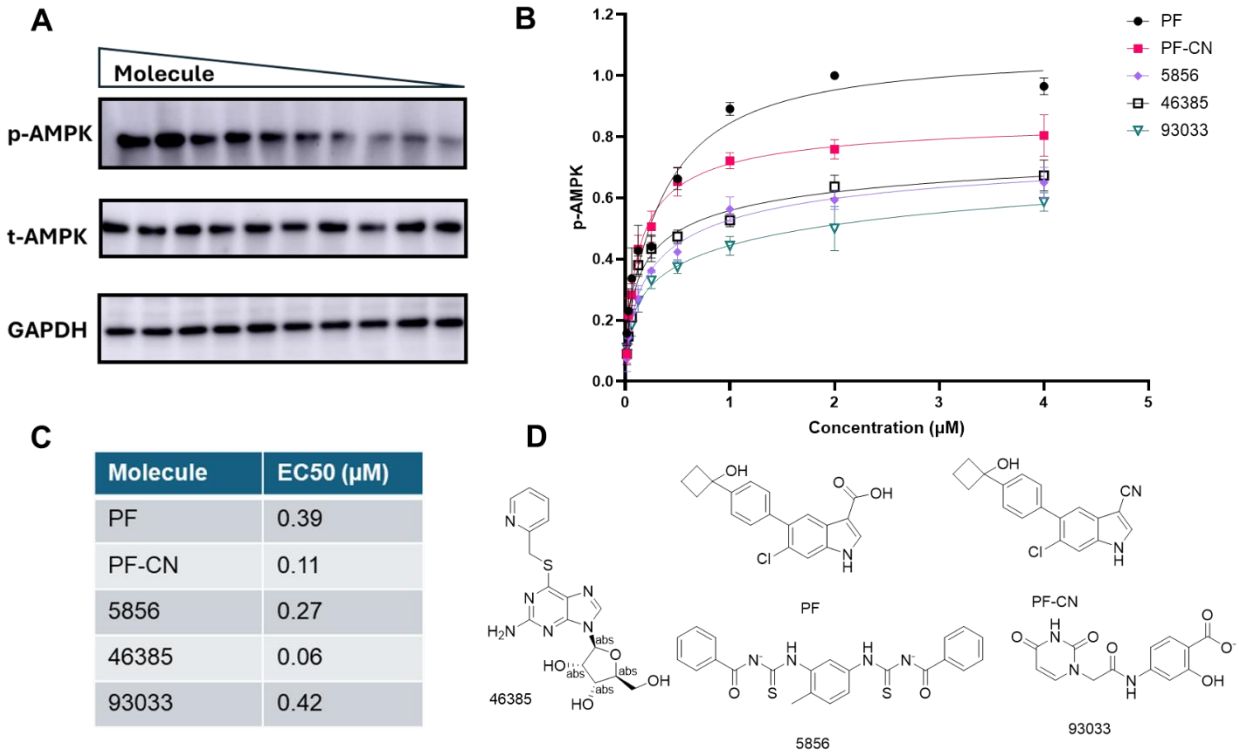
Figure 7.7: Results from kinase-Glo luminescence assay of small molecules with AMPKβ1 **A)** Luminescence signal as a function of ligand concentration is plotted. **B)** Chemical structures of the ligands that showed any effect on AMPKβ1 activity assay.

7.5.3 HeLa cell-based kinase activity assay

Hits from the *in vitro* kinase-Glo assay were evaluated for the functional activation of AMPK in HeLa cells to assess if the effects seen *in vitro* could be translated into cells. HeLa cells expressing different AMPK isoforms were treated with increasing concentration of ligands and AMPK activity was monitored using western blot analysis using antibodies probing for phosphorylation of the alpha subunit at Thr172.

Cells were passaged and allowed to grow to ~60-70% confluence in a 12 well plate. The cells were treated with increasing amounts of small molecules and incubated for 16 hours after which cells were lysed and harvested using RIPA lysis buffer following the manufacturer's protocol. The protein lysate concentration was assessed using a BCA

assay and 10 µg of protein was run on an SDS-PAGE. The gel was transferred to a PVDV membrane using Bio-Rad turbo blot transfer system. The blot was first probed using a rabbit p-AMPK Ab specific for detecting phosphorylation of Thr172 in alpha subunit. This was followed by stripping and re-probing the blot with a mouse t-AMPK Ab to assess the total AMPK protein. Finally, the blot was stripped and re-probed again with a chicken GAPDH Ab to detect the levels of GAPDH which was used as a loading control.



Molecule	EC50 (µM)
PF	0.39
PF-CN	0.11
5856	0.27
46385	0.06
93033	0.42

Figure 7.8: Results from HeLa cell-based kinase activity assay. **A)** Representative blots from a HeLa cell assay probing for p-AMPK, t-AMPK and loading control GAPDH signals. **B)** Graphical representation of the signals from western blots. p-AMPK signals plotted as a function of ligand concentration. **C)** EC50 values of different ligands **D)** Chemical structures of small molecules that showed AMPK activity in HeLa cells.

Of the 13 molecules being screened (including PF and PF-CN), only 5 compounds showed positive effects on AMPK activity in HeLa cells in the concentration range being tested. PF and PF-CN again showed the overall biggest effect on AMPK activation, while

PF-CN and ligand 46385 seemed to be the fastest acting with the lowest EC50 values in the concentration range being assessed (Figure 7.8). Since HeLa cells express both β1 and β2 isoforms of AMPK[193–195] it was difficult to assess selectivity, but overall kinase activation could be estimated.

7.5.4 ITC Binding studies

The 3 compounds that showed AMPK activity in HeLa cells along with PF and PF-CN were taken further to assess their binding affinities to AMPKβ1. This assay would provide direct evidence of binding the underlying thermodynamic parameters. ITC experiments showed that PF-CN bound significantly better than PF compound (Figure 7.9) to the AMPKβ1 isoform. Although all the other hits - 46385, 5856 and 93033 did bind to AMPKβ1, but their binding affinities was significantly lower as compared to the PF compound.

A

Molecule	Binding Affinity	Kd	ΔH (kJ/mol)	ΔS(J/mol·K)	ΔG(kJ/mol)
PF	-	1.4E-08 ± 5.2E-10	-85.2 ± 1.1	-135.6 ± 3.2	-44.8 ± 1.0
PF-CN	Increase	4.1E-09 ± 1.2E-09	-79.4 ± 4.7	-105.5 ± 14.9	-47.9 ± 0.7
46385	Decrease	5.6E-07 ± 3.2E-07	8.6 ± 1.7	150.1 ± 2.7	-36.2 ± 1.7
5856	Decrease	1.9E-06 ± 7.6E-07	10.6 ± 1.1	145.3 ± 3.3	-32.7 ± 0.9
93033	Decrease	3.7E-06 ± 2.1E-06	14.7 ± 4.1	154.7 ± 9.2	-31.4 ± 1.3

B

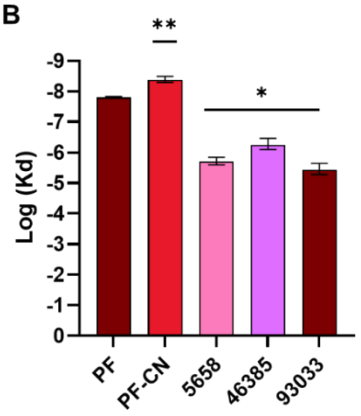


Figure 7.9: A) Results from binding studies of molecules with AMPKβ1. **B)** Graphical representation of binding affinities of ligands with AMPKβ1. Statistical analysis was performed using two tailed Welch's *t*-test (*p<0.5, **p<0.1).

7.5.5 Selectively of compounds binding to AMPK isoforms

To assess the selectivity of compounds PF, PF-CN, 46385, 5856 and 93033 towards either β1 or β2 isoform of AMPK, I performed the kinase-Glo assay described above with recombinantly expressed and purified AMPKβ2 isoform. The concentrations of the SAMS peptide, AMPK and ATP were held constant in the assay, and only ligand concentration was varied to assess the effect on kinase activity.

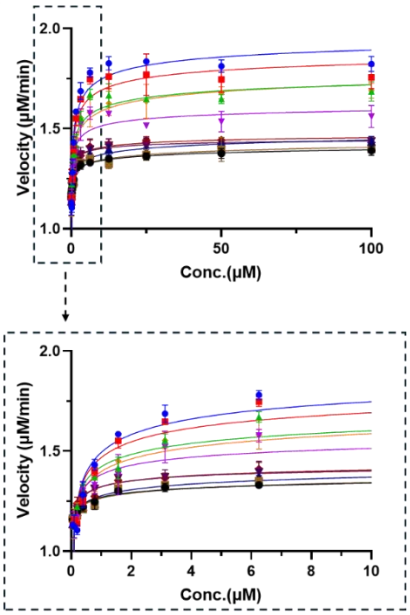
To analyze the kinetic parameters and compare the selectivity between β1 or β2, I converted the luminescence signals from both experiments into reaction rates. Since the kinase-Glo reaction is a type of ATP consumption assay, I was able to measure the rate at which AMPK isoforms utilize ATP during the reaction. I then plotted the reaction rates against ligand concentration to compare the effects of ligands (Figure 7.10A). PF binds to AMPKβ1 in the interface between the α and β subunits and activates it. Since this binding is a type of an allosteric activation event[167], I fit the curve using allosteric sigmoidal model to obtain various kinetic properties of the reaction (Figure 7.10B). The sigmoidal model being used here is a more complex model for enzymatic kinetics as compared to the commonly used Michelis Menten equation, but the sigmoidal model accounts for cooperativity and allosteric effects and is more suitable for proteins with multiple subunits[196,197]. The allosteric sigmoidal model uses the following equation:

$$v = V_{max} * [S]^h / (Khalf^h + [S]^h)$$

where v is the reaction rate, Vmax is the maximum enzyme velocity, Khalf is the concentration of substrate that produces a half-maximal enzyme velocity (it is the EC50), S is the substrate concentration, h is the Hill slope and relates to the cooperativity, Kprime is related to the Km and is computed as Khalf^h.

Based on the kinase-Glo assay using both AMPKβ1 and β2 isoforms, I found that Vmax for all the ligands was consistently higher for AMPKβ1 (Figure 7.10) suggesting

A



B

Allosteric sigmoidal		PF	PF-CN	5856	46385	93033
AMPKb1	Vmax	2.032	1.956	1.877	1.673	1.932
	h	0.3436	0.3278	0.2695	0.2977	0.2446
	Khalf	0.05141	0.03481	0.01461	0.005255	0.01949
	Kprime	0.3606	0.3326	0.3202	0.2096	0.3817
	R^2	0.9318	0.9174	0.9313	0.8586	0.9333
AMPKb2	Vmax	1.533	1.616	1.636	1.470	1.518
	h	0.1590	0.1350	0.1604	0.3511	0.2673
	Khalf	5.066e-005	7.496e-005	0.0003714	0.001978	0.0007790
	Kprime	0.2076	0.2774	0.2816	0.1124	0.1476
	R^2	0.9429	0.9062	0.9630	0.9179	0.9206

Figure 7.10: A) Data from the kinase-Glo luminescence assay converted to reaction rates and fitted using allosteric sigmoidal model. **B)** Enzyme kinetics parameters assessed from the curve fitting model.

higher catalytic efficiency of AMPKβ1 compared to AMPKβ2 when interacting with molecules i.e., under saturating substrate conditions AMPKβ1 processes the substrate faster than AMPKβ2.

Similarly, I found that Kprime (Km) was higher for all the ligands with AMPKβ1 (Figure 7.10) which suggests while AMPKβ1 is more efficient at high substrate concentration, AMPKβ2 might have higher affinity for substrates at lower concentrations. The higher Vmax of AMPKβ1 with ligands suggests selective activation of β1 could result in more effective modulation of metabolic pathways crucial for gut barrier integrity. Understanding these kinetic differences could guide the design of more potent and

selective AMPKβ1 activators, potentially leading to better therapeutic outcomes for IBD patients.

Next, to investigate a direct relationship between the selectivity of these 5 ligands to different AMPK isoforms, I carried out ITC binding experiments with recombinantly expressed and purified AMPKβ2 isoform. None of the three molecules 5856, 46385 and 93033 bound to AMPKβ2. Both PF and PF-CN seemed to bind to AMPKβ2 with mild binding affinity. The binding affinity of PF-CN to AMPKβ2 seemed to be lower than of PF to AMPKβ2, but it was not found to be statistically significant (Figure 7.11).

A

Molecule	Binding Affinity	Kd	ΔH (kJ/mol)	ΔS(J/mol·K)	ΔG(kJ/mol)
PF	-	6.2E-06 ± 3.8E-07	-33.3 ± 0.5	-13.6 ± 2.1	-29.7 ± 0.1
PF-CN	Decrease	2.2E-04 ± 1.2E-04	-42.6 ± 2.1	-71.8 ± 5.2	-21.2 ± 1.2

B

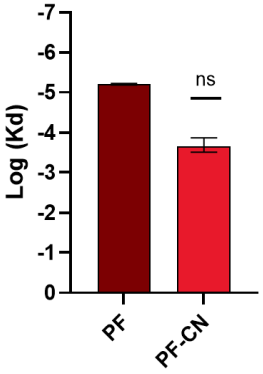


Figure 7.11: A) Results from binding studies of molecules with AMPKβ2. **B)** Graphical representation of binding affinities with AMPKβ2. Statistical analysis was performed using two tailed Welch's *t*-test (ns = no significance)

Since none of the hits from the virtual screening showed direct binding to AMPKβ2, the effects seen in the *in vitro* as well as the HeLa cell assay might have been caused due to off target interactions.

On comparing the binding affinities between AMPKβ1 and β2 I found that both PF and PF-CN are more selective towards the β1 isoform, with PF-CN being significantly more selective towards binding to AMPKβ1 than the PF compound (Figure 7.12). To further investigate the rationale behind these different binding affinities, I carried out

molecular docking studies of PF and PF-CN with both AMPKβ1 and AMPKβ2 isoforms. The binding site is located between the interface of alpha and beta subunits. I found that for PF compound, some key interactions with residues D88 and K29 were missing when bound to AMPKβ2 compared to β1 binding which could explain the significant reduction seen in binding affinity of PF to AMPKβ2 (Figure 7.12). Similarly, for PF-CN, apart from missing interactions with residues D88 and K29, another key interaction with residue K31 was also missing when bound to AMPKβ2 isoform which was previously seen when bound to AMPKβ1 (Figure 7.12). This could possibly explain the further reduction in binding affinity of PF-CN towards AMPKβ2 and being more selective for AMPKβ1.

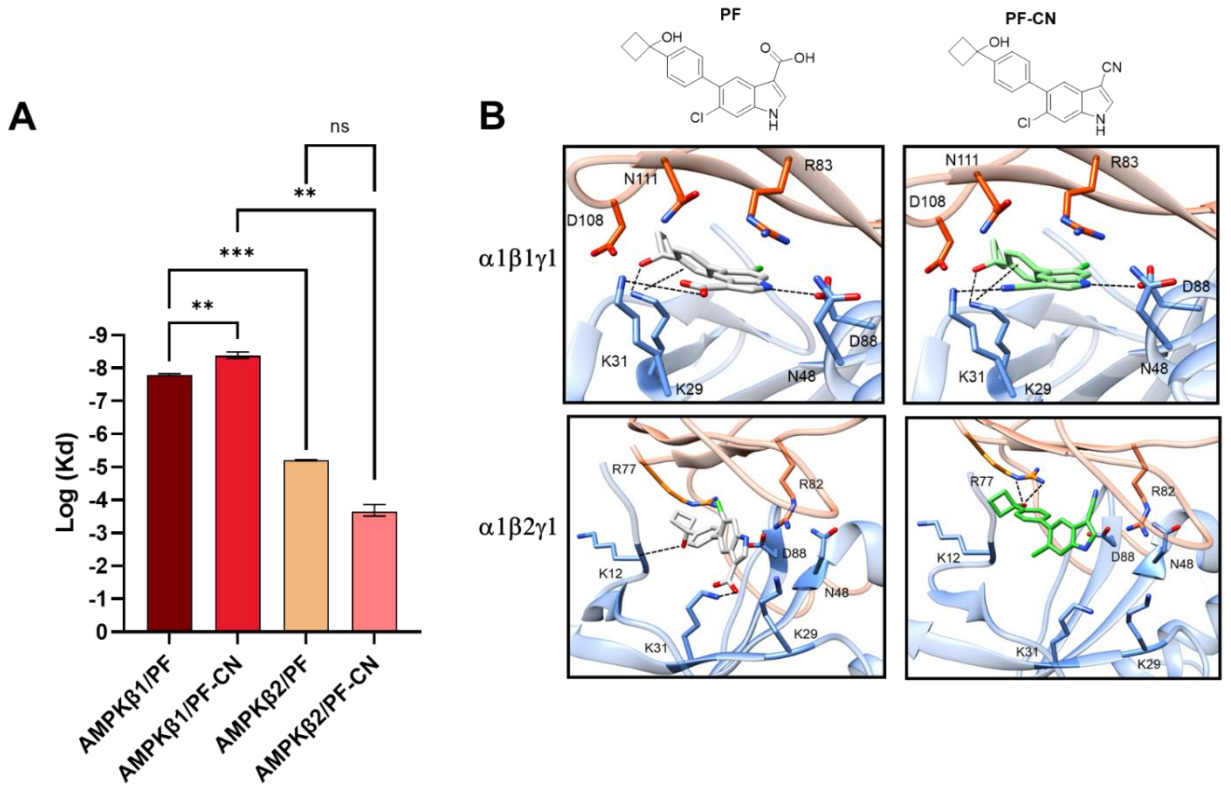


Figure 7.12: A) Graphical representation of binding affinities of PF and PF-CN with AMPKβ1 and AMPKβ2 isoforms. **B)** Docked poses of PF and PF-CN in the binding site of AMPKβ1 (top panel) and AMPKβ2 (bottom panel). Statistical analysis was performed using two tailed Welch's *t*-test (**p<0.1, ***p<0.01).

7.6 Conclusion

In this chapter, I developed and proposed novel molecules based on a pharmacophore model, some of which are expected to selectively bind to AMPKβ1 with better affinity. In parallel to synthesizing novel compounds in the Yang lab, I carried out virtual screening from the existing pool of commercially available ligands to find new scaffolds and lead compounds. The top hits from the virtual screen were further screened in the Yang lab using a luminescence-based assay *in vitro* and a cell based *in vivo* assay to further narrow down the hits to only a handful of compounds. These hits were then tested for their binding affinities to different AMPK isoforms.

Of all the molecules tested, only PF-CN bound significantly better than the control molecule PF to AMPKβ1. PF-CN was also found to be more selective towards AMPKβ1. The difference in binding could be attributed to missing interactions with key residues in the binding pocket for the PF-CN and AMPKβ2 complex. Although some other compounds screened from NCI datasets did bind to AMPKβ1, the binding affinities for these compounds was significantly lower than the control PF compound. Interestingly, none of the hits from the NCI datasets bound to AMPKβ2 isoform.

From this screening assay, only PF-CN was promising enough to be taken further for additional experiments, to explore the physiological relevance of these findings and the therapeutic efficacy of the designed molecules. This will be studied in single cell systems and organoid models in the Ghosh lab.

Even though none of the molecules from the virtual screening made it to the next stage of drug development, the three molecules from the virtual screen showed p-AMPK activity in HeLa cells and bound to AMPKβ1 in the micromolar ranges. For future studies these

three molecules, possessing different functional scaffolds compared to the PF compound could be used as a starting template to design new series of compounds that can target AMPKβ1 selectively. I was able to also showcase how a drug discovery and development pipeline could be executed to find potential lead compounds taking into account both the synthesis and the *in silico* screening capabilities of the Yang lab.

7.7 Methods

Molecular Docking

All steps for the docking experiments were carried out similar to that mentioned in Chapter 2 of this thesis using Schrodinger suite 2019-20. The crystallographic structure of AMPK was retrieved from RCSB Protein Data Bank, PDB ID: 5KQ5[167]. The protein was prepared using Maestro's Protein Preparation Wizard[94]. The receptor grids were generated at the center of mass of the pocket residues where the ligand was bound in the crystal structure and were made large enough to contain the binding site of the protein and the surrounding surface regions. Ligands were constructed in Maestro[94] and LigPrep[96] was used to prepare the ligands for molecular docking. Each generated ligand was docked into the binding site using Glide[95] with extra precision docking and default parameters to generate 100 poses for the ligand-receptor complex. The poses were clustered together using a cutoff RMSD value of 2 Å. The ligand interaction tool of the Molecular Operating Environment (MOE) software[97] was used to study the expected interactions between ligand and protein residues in the binding sites. All the docked pose images were generated using Chimera [98].

Expression and purification of AMPK isoforms

AMPK was transformed into *E. coli* NEB BL21 DE3 strain and transformants were selected on LB (Luria–Bertani) agar plates containing ampicillin (100µg/mL) and Kanamycin (50µg/mL). Single colonies were used to inoculate 10mL of LB medium containing required antibiotics. For large-scale expression and purification, 1 L of LB broth supplemented with 100µg/ml ampicillin and 50µg/ml Kanamycin was inoculated with 25 ml of overnight culture and grown in a shaking incubator at 37 °C to an OD600 of 0.8. Protein expression was induced with 100µM (final concentration) IPTG, the temperature was reduced to 18 °C, and the cells were grown for an additional 18 h. Cells were harvested and resuspended in 50 mL lysis buffer (50 mM Tris, pH 8.0, 150 mM NaCl, 5% glycerol, 2 mM TCEP, 20 mM imidazole). The cell suspension was sonicated on ice with 10 sec on/off pulse for 10-20 min at 60% intensity. Insoluble material was removed by centrifugation at 18x000g for 30 min at 4 °C, and the supernatant was loaded onto a 5 mL HisTrap™ HP column (GE Healthcare) and washed with ten column volumes of lysis buffer (50 mM Tris, pH 8.0, 150 mM NaCl, 5% glycerol, 2 mM TCEP, 20 mM imidazole). Bound proteins were eluted using a linear gradient (10 column volumes) with elution buffer (lysis buffer containing 300 mM imidazole). Fractions containing AMPK subunits were pooled based on SDS-PAGE analysis and dialyzed overnight in dialysis buffer (50 mM Tris, pH 8.0, 150 mM NaCl, 5% glycerol, 2 mM TCEP). For some experiments, the AMPK α1β1γ1 or α1β2γ1 isoforms were further purified by gel filtration chromatography with a Superdex-200 Hi Load column (GE Healthcare) in SEC buffer (50 mM Tris, pH 8.0, 150 mM NaCl, 5% glycerol, 2 mM TCEP). The SEC monomeric and soluble aggregate peaks were pooled separately and dialyzed in dialysis buffer as before.

Expression and purification of GST-CaMKK2

GST-CaMKK2 was expressed and purified using the same conditions as the AMPK isoforms mentioned above.

Kinase-Glo assay

Kinase-Glo assay was carried out using a kit from Promega[190]. Standard ATP curves were prepared using manufacturer's protocol. Different substrate and kinase concentrations were tested and optimized using recommendations from the manufacturer. For the kinase reaction, AMPK enzyme (1µM) solution was added first to a white opaque 96 well plate. Next, SAMS peptide (10µM) was added to the wells followed by serially diluted small molecules (0-100µM). Finally, ATP (100µM) was added to initiate the reaction and incubated for 40 minutes at 37°C. The reaction was quenched using Glo reagent and incubated for 30 minutes. This was followed by incubation with Glo detection reagent for 30 minutes at RT. The luminescence reading was measured using a plate reader. The graphs were plotted and analyzed on GraphPad prism.

HeLa cell culture

HeLa cells were maintained in a 37º humidified incubator with 5% CO2 in Modified Eagle's Medium (Gibco) supplemented with 10% heat inactivated horse serum (Gibco) and 5-10% FBS (Gibco).

Quantitative western blot

Quantitative western blots were accomplished by normalizing total protein concentration using the Pierce BCA assay and following the manufacturer's protocol. Identical quantities of total protein were loaded onto a 4-20% SDS-PAGE gel (BioRad) and run for 40 minutes at 160V. The protein was then transferred to an activated low fluorescence PVDF membrane (BioRad) using the TransBlot Turbo system (BioRad). Blots were incubated for 1h at RT in 5% BSA in TBST, followed by overnight incubation with primary antibody (1:1000 dilution) in 5% BSA at 4ºC. The blot was then washed three times for 5 minutes each in TBST at RT. Secondary antibody (1:5000) was added in 5% BSA in TBST and allowed to incubate at RT for 1h. The membrane was then washed three times for 5 minutes each in TBST at RT, rinsed in MilliQ water three times. HRP reagent was added and incubated for 30 seconds and then imaged using the Amersham imager. The blots were incubated with stripping buffer for 30 mins and blocked again for 1 h at RT followed by incubation steps for primary and secondary antibodies as described above.

Isothermal Titration Calorimetry

Calorimetric measurements were carried out using a Low Volume ITC instrument (TA Instruments) as described in Chapter 2 of this thesis. All measurements were carried out at 25°C. The protein was dialyzed in 50mM HEPES buffer (pH 7.5), 150mM NaCl to a concentration of 10-100µM. The ligand solution contained 100µM-1mM of the small molecule dissolved in the same buffer as the protein. Data was analyzed using the NanoAnalyze software (TA Instruments) for fitting points to the independent binding

model. Experimental heats of the protein-small molecule titration were corrected for heats of dilution of the ligands into buffer alone.

7.8 Acknowledgements

I would like to thank Professor Jon Oakhill for graciously providing me with all the plasmids that I used in this study. I would like to thank Joseph Sawires for providing me with both the PF and the PF-CN molecules for my assays. I would like to acknowledge Professor Ghosh for her constant guidance and help with various aspects of this project. I would also like to thank Dr. Christian Seitz and Professor Andrew McCammon for their guidance and help with the virtual screening of molecules from NCI datasets.

REFERENCES

(1) Alzheimer; Association. Alzheimer's Association 2024 Alzheimer's Disease Facts and Figures. *Alzheimer's Assoc.* **2024**, *20* (5), 1–146.

(2) Clare, R.; King, V. G.; Wirenfeldt, M.; Vinters, H. V. Synapse Loss in Dementias. *Journal of Neuroscience Research*. J Neurosci Res August 1, **2010**, pp 2083–2090.

(3) Brun, A.; Liu, X.; Erikson, C. Synapse Loss and Gliosis in the Molecular Layer of the Cerebral Cortex in Alzheimer's Disease and in Frontal Lobe Degeneration. *Neurodegeneration* **1995**, *4* (2), 171–177.

(4) Brunnström, H. R.; Englund, E. M. Cause of Death in Patients with Dementia Disorders. *Eur. J. Neurol.* **2009**, *16* (4), 488–492.

(5) Kochanek, K. D.; Murphy, S. L.; Xu, J.; Arias, E. National Vital Statistics Reports Volume 72, Number 10, September 22, 2023. **2020**.

(6) Hardy, J. A.; Higgins, G. A. Alzheimer's Disease: The Amyloid Cascade Hypothesis. *Science*. American Association for the Advancement of Science **1992**, pp 184–185.

(7) Wood, W. G.; Eckert, G. P.; Igbavboa, U.; Müller, W. E. Amyloid Beta-Protein Interactions with Membranes and Cholesterol: Causes or Casualties of Alzheimer's Disease. *Biochimica et Biophysica Acta - Biomembranes*. Elsevier March 10, **2003**, pp 281–290.

(8) Iversen, L. L.; Mortishire-Smith, R. J.; Pollack, S. J.; Shearman, M. S. The Toxicity in Vitro of β-Amyloid Protein. *Biochemical Journal*. Biochem J **1995**, pp 1–16.

(9) Cummings, J. Anti-Amyloid Monoclonal Antibodies Are Transformative Treatments That Redefine Alzheimer's Disease Therapeutics. *Drugs* **2023**, *83* (7), 569–576.

(10) Pul, R.; Dodel, R.; Stangel, M. Antibody-Based Therapy in Alzheimer's Disease. *Expert Opinion on Biological Therapy*. Expert Opin Biol Ther March **2011**, pp 343–357.

(11) Cummings, J.; Osse, A. M. L.; Cammann, D.; Powell, J.; Chen, J. Anti-Amyloid Monoclonal Antibodies for the Treatment of Alzheimer's Disease. *BioDrugs*. BioDrugs January 1, **2024**, pp 5–22.

(12) Sinclair, L. I.; Tayler, H. M.; Love, S. Synaptic Protein Levels Altered in Vascular Dementia. *Neuropathol. Appl. Neurobiol.* **2015**, *41* (4), 533–543.

(13) Clinton, J.; Forsyth, C.; Royston, M. C.; Roberts, G. W. Synaptic Degeneration Is the Primary Neuropathological Feature in Prion Disease: A Preliminary Study. *Neuroreport* **1993**, *4* (1), 65–68.

(14) Calabrese, B.; Wilson, M. S.; Halpain, S. Development and Regulation of Dendritic Spine Synapses. *Physiology*. Physiology (Bethesda) February **2006**, pp 38–47.

(15) Hayashi, M. L.; Choi, S. Y.; Shankaranarayana Rao, B. S.; Jung, H. Y.; Lee, H. K.; Zhang, D.; Chattarji, S.; Kirkwood, A.; Tonegawa, S. Altered Cortical Synaptic Morphology and Impaired Memory Consolidation in Forebrain- Specific Dominant-Negative PAK Transgenic Mice. *Neuron* **2004**, *42* (5), 773–787.

(16) Morgado-Bernal, I. Learning and Memory Consolidation: Linking Molecular and Behavioral Data. *Neuroscience*. Neuroscience March 10, **2011**, pp 12–19.

(17) Biancalana, M.; Koide, S. Molecular Mechanism of Thioflavin-T Binding to Amyloid Fibrils. *Biochimica et Biophysica Acta - Proteins and Proteomics*. Biochim Biophys Acta July **2010**, pp 1405–1412.

(18) Inbar, P.; Li, C. Q.; Takayama, S. A.; Bautista, M. R.; Yang, J. Oligo(Ethylene Glycol) Derivatives of Thioflavin T as Inhibitors of Protein-Amyloid Interactions. *ChemBioChem* **2006**, *7* (10), 1563–1566.

(19) Habib, L. K.; Lee, M. T. C.; Yang, J. Inhibitors of Catalase-Amyloid Interactions Protect Cells from β-Amyloid-Induced Oxidative Stress and Toxicity. *J. Biol. Chem.* **2010**, *285* (50), 38933–38943.

(20) Song, J. M.; DiBattista, A. M.; Sung, Y. M.; Ahn, J. M.; Turner, R. S.; Yang, J.; Pak, D. T. S.; Lee, H. K.; Hoe, H. S. A Tetra(Ethylene Glycol) Derivative of Benzothiazole Aniline Ameliorates Dendritic Spine Density and Cognitive Function in a Mouse Model of Alzheimer's Disease. *Exp. Neurol.* **2014**, *252*, 105–113.

(21) Megill, A.; Lee, T.; DiBattista, A. M.; Min Song, J.; Spitzer, M. H.; Rubinshtein, M.; Habib, L. K.; Capule, C. C.; Mayer, M.; Scott Turner, R.; Kirkwood, A.; Yang, J.; Pak, D. T. S.; Lee, H. K.; Hoe, H. S. A Tetra(Ethylene Glycol) Derivative of Benzothiazole Aniline Enhances Ras-Mediated Spinogenesis. *J. Neurosci.* **2013**, *33* (22), 9306–9318.

(22) Yuste, R. The Discovery of Dendritic Spines by Cajal. *Front. Neuroanat.* **2015**, *9* (APR), 123598.

(23) Yoshihara, Y.; De Roo, M.; Muller, D. Dendritic Spine Formation and Stabilization. *Current Opinion in Neurobiology*. Curr Opin Neurobiol April **2009**, pp 146–153.

(24) Leuner, B.; Falduto, J.; Shors, T. J. Associative Memory Formation Increases the Observation of Dendritic Spines in the Hippocampus. *J. Neurosci.* **2003**, *23* (2), 659–665.
(25) Knobloch, M.; Mansuy, I. M. Dendritic Spine Loss and Synaptic Alterations in Alzheimer's Disease. *Molecular Neurobiology*. Mol Neurobiol **2008**, pp 73–82.

(26) Penzes, P.; Cahill, M. E.; Jones, K. A.; Vanleeuwen, J. E.; Woolfrey, K. M. Dendritic Spine Pathology in Neuropsychiatric Disorders. *Nature Neuroscience*. NIH Public Access March **2011**, pp 285–293.

(27) Cifelli, J. L.; Dozier, L.; Chung, T. S.; Patrick, G. N.; Yang, J. Benzothiazole Amphiphiles Promote the Formation of Dendritic Spines in Primary Hippocampal Neurons. *J. Biol. Chem.* **2016**, *291* (23), 11981–11992.

(28) Cifelli, J. L.; Berg, K. R.; Yang, J. Benzothiazole Amphiphiles Promote RasGRF1-Associated Dendritic Spine Formation in Human Stem Cell-Derived Neurons. *FEBS Open Bio* **2020**, *10* (3), 386–395.

(29) Sibucao, K. UC San Diego UC San Diego Electronic Theses and Dissertations Title Photoaffinity Labeling Studies on a Promoter of Dendritic Spine Formation. **2017**.

(30) Kane, R. E. Actin Polymerization and Interaction with Other Proteins in Temperature-Induced Gelation of Sea Urchin Egg Extracts. *J. Cell Biol.* **1976**, *71* (3), 704–714.

(31) Kane, R. E. Preparation and Purification of Polymerized Actin from Sea Urchin Egg Extracts. *J. Cell Biol.* **1975**, *66* (2), 305–315.

(32) Otto, J. J.; Kane, R. E.; Bryan, J. Formation of Filopodia in Coelomocytes: Localization of Fascin, a 58,000 Dalton Actin Cross-Linking Protein. *Cell* **1979**, *17* (2), 285–293.

(33) Edwards, R. A.; Herrera-Sosa, H.; Otto, J.; Bryan, J. Cloning and Expression of a Murine Fascin Homolog from Mouse Brain. *J. Biol. Chem.* **1995**, *270* (18), 10764–10770.

(34) Zhang, F. R.; Tao, L. H.; Shen, Z. Y.; Lv, Z.; Xu, L. Y.; Li, E. M. Fascin Expression in Human Embryonic, Fetal, and Normal Adult Tissue. *J. Histochem. Cytochem.* **2008**, *56* (2), 193–199.

(35) Han, S.; Huang, J.; Liu, B.; Xing, B.; Bordeleau, F.; Reinhart-King, C. A.; Li, W.; Zhang, J. J.; Huang, X. Y. Improving Fascin Inhibitors to Block Tumor Cell Migration and Metastasis. *Mol. Oncol.* **2016**, *10* (7), 966–980.

(36) Ono, S.; Yamakita, Y.; Yamashiro, S.; Matsudaira, P. T.; Gnarra, J. R.; Obinata,

T.; Matsumura, F. Identification of an Actin Binding Region and a Protein Kinase C Phosphorylation Site on Human Fascin. *J. Biol. Chem.* **1997**, *272* (4), 2527–2533.

(37) Sedeh, R. S.; Fedorov, A. A.; Fedorov, E. V.; Ono, S.; Matsumura, F.; Almo, S. C.; Bathe, M. Structure, Evolutionary Conservation, and Conformational Dynamics of Homo Sapiens Fascin-1, an F-Actin Crosslinking Protein. *J. Mol. Biol.* **2010**, *400* (3), 589–604.

(38) Jansen, S.; Collins, A.; Yang, C.; Rebowski, G.; Svitkina, T.; Dominguez, R. Mechanism of Actin Filament Bundling by Fascin. *J. Biol. Chem.* **2011**, *286* (34), 30087–30096.

(39) Vignjevic, D.; Kojima, S. I.; Aratyn, Y.; Danciu, O.; Svitkina, T.; Borisy, G. G. Role of Fascin in Filopodial Protrusion. *J. Cell Biol.* **2006**, *174* (6), 863–875.

(40) Yang, S.; Huang, F. K.; Huang, J.; Chen, S.; Jakoncic, J.; Leo-Macias, A.; Diaz-Avalos, R.; Chen, L.; Zhang, J. J.; Huang, X. Y. Molecular Mechanism of Fascin Function in Filopodial Formation. *J. Biol. Chem.* **2013**, *288* (1), 274–284.

(41) Mattila, P. K.; Lappalainen, P. Filopodia: Molecular Architecture and Cellular Functions. *Nature Reviews Molecular Cell Biology*. Nat Rev Mol Cell Biol June 10, **2008**, pp 446–454.

(42) Winkelman, J. D.; Suarez, C.; Hocky, G. M.; Harker, A. J.; Morganthaler, A. N.; Christensen, J. R.; Voth, G. A.; Bartles, J. R.; Kovar, D. R. Fascin- and α-Actinin-Bundled Networks Contain Intrinsic Structural Features That Drive Protein Sorting. *Curr. Biol.* **2016**, *26* (20), 2697–2706.

(43) Claessens, M. M. A. E.; Semmrich, C.; Ramos, L.; Bausch, A. R. Helical Twist Controls the Thickness of F-Actin Bundles. *Proc. Natl. Acad. Sci. U. S. A.* **2008**, *105* (26), 8819–8822.

(44) Pelosi, G.; Pastorino, U.; Pasini, F.; Maissoneuve, P.; Fraggetta, F.; Iannucci, A.; Sonzogni, A.; De Manzoni, G.; Terzi, A.; Durante, E.; Bresaola, E.; Pezzella, F.; Viale, G. Independent Prognostic Value of Fascin Immunoreactivity in Stage I Nonsmall Cell Lung Cancer. *Br. J. Cancer* **2003**, *88* (4), 537–547.

(45) Machesky, L. M.; Lia., A. Fascin: Invasive Filopodia Promoting Metastasis. *Commun. Integr. Biol.* **2010**, *3* (3), 263–270.

(46) Valkov, A.; Sorbye, S. W.; Kilvaer, T. K.; Donnem, T.; Smeland, E.; Bremnes, R. M.; Busund, L. T. The Prognostic Impact of TGF-B1, Fascin, NF-Kb and PKC-ζ Expression in Soft Tissue Sarcomas. *PLoS One* **2011**, *6* (3), e17507.

(47) Gun, B. D.; Bahadir, B.; Bektas, S.; Barut, F.; Yurdakan, G.; Kandemir, N. O.;

Ozdamar, S. O. Clinicopathological Significance of Fascin and CD44v6 Expression in Endometrioid Carcinoma. *Diagn. Pathol.* **2012**, *7* (1).

(48) Rodrigues, P. C.; Sawazaki-Calone, I.; de Oliveira, C. E.; Macedo, C. C. S.; Dourado, M. R.; Cervigne, N. K.; Miguel, M. C.; do Carmo, A. F.; Lambert, D. W.; Graner, E.; da Silva, S. D.; Alaoui-Jamali, M. A.; Leme, A. F. P.; Salo, T. A.; Coletta, R. D. Fascin Promotes Migration and Invasion and Is a Prognostic Marker for Oral Squamous Cell Carcinoma. *Oncotarget* **2017**, *8* (43), 74736–74754.

(49) Lin, S.; Taylor, M. D.; Singh, P. K.; Yang, S. How Does Fascin Promote Cancer Metastasis? *FEBS Journal*. FEBS J March 1, **2021**, pp 1434–1446.

(50) Li, A.; Dawson, J. C.; Forero-Vargas, M.; Spence, H. J.; Yu, X.; König, I.; Anderson, K.; Machesky, L. M. The Actin-Bundling Protein Fascin Stabilizes Actin in Invadopodia and Potentiates Protrusive Invasion. *Curr. Biol.* **2010**, *20* (4), 339–345.

(51) Van Audenhove, I.; Denert, M.; Boucherie, C.; Pieters, L.; Cornelissen, M.; Gettemans, J. Fascin Rigidity and L-Plastin Flexibility Cooperate in Cancer Cell Invadopodia and FilopodiaS. *J. Biol. Chem.* **2016**, *291* (17), 9148–9160.

(52) Jacquemet, G.; Hamidi, H.; Ivaska, J. Filopodia in Cell Adhesion, 3D Migration and Cancer Cell Invasion. *Current Opinion in Cell Biology*. Curr Opin Cell Biol October 1, **2015**, pp 23–31.

(53) Jayo, A.; Malboubi, M.; Antoku, S.; Chang, W.; Ortiz-Zapater, E.; Groen, C.; Pfisterer, K.; Tootle, T.; Charras, G.; Gundersen, G. G.; Parsons, M. Fascin Regulates Nuclear Movement and Deformation in Migrating Cells. *Dev. Cell* **2016**, *38* (4), 371–383.

(54) Pfisterer, K.; Jayo, A.; Parsons, M. Control of Nuclear Organization by F-Actin Binding Proteins. *Nucleus* **2017**, *8* (2), 126–133.

(55) Zanet, J.; Jayo, A.; Plaza, S.; Millard, T.; Parsons, M.; Stramer, B. Fascin Promotes Filopodia Formation Independent of Its Role in Actin Bundling. *J. Cell Biol.* **2012**, *197* (4), 477–486.

(56) Oak, Y. Filopodia-Independent Roles of the Actin Bundling Protein Fascin in Promoting Cell Motility. **2014**.

(57) Lamb, M. C.; Tootle, T. L. Fascin in Cell Migration: More than an Actin Bundling Protein. *Biology*. Multidisciplinary Digital Publishing Institute (MDPI) November 1, **2020**, pp 1–18.

(58) Elkhatib, N.; Neu, M. B.; Zensen, C.; Schmoller, K. M.; Louvard, D.; Bausch, A.

R.; Betz, T.; Vignjevic, D. M. Fascin Plays a Role in Stress Fiber Organization and Focal Adhesion Disassembly. *Curr. Biol.* **2014**, *24* (13), 1492–1499.

(59) Zhang, J.; Fonovic, M.; Suyama, K.; Bogyo, M.; Scott, M. P. Rab35 Controls Actin Bundling by Recruiting Fascin as an Effector Protein. *Science.* **2009**, *325* (5945), 1250–1254.

(60) Beghein, E.; Devriese, D.; Van Hoey, E.; Gettemans, J. Cortactin and Fascin-1 Regulate Extracellular Vesicle Release by Controlling Endosomal Trafficking or Invadopodia Formation and Function. *Sci. Rep.* **2018**, *8* (1), 1–16.

(61) Saad, A.; Bijian, K.; Qiu, D.; Da Silva, S. D.; Marques, M.; Chang, C. H.; Nassour, H.; Ramotar, D.; Damaraju, S.; Mackey, J.; Bismar, T.; Witcher, M.; Alaoui-Jamali, M. A. Insights into a Novel Nuclear Function for Fascin in the Regulation of the Amino-Acid Transporter SLC3A2. *Sci. Rep.* **2016**, *6*.

(62) Cohan, C. S.; Welnhofer, E. A.; Zhao, L.; Matsumura, F.; Yamashiro, S. Role of the Actin Bundling Protein Fascin in Growth Cone Morphogenesis: Localization in Filopodia and Lamellipodia. *Cell Motil. Cytoskeleton* **2001**, *48* (2), 109–120.

(63) Lowery, L. A.; Vactor, D. Van. The Trip of the Tip: Understanding the Growth Cone Machinery. *Nature Reviews Molecular Cell Biology*. Nat Rev Mol Cell Biol May **2009**, pp 332–343.

(64) Korobova, F.; Svitkina, T. Arp2/3 Complex Is Important for Filopodia Formation, Growth Cone Motility, and Neuritogenesis in Neuronal Cells. *Mol. Biol. Cell* **2008**, *19* (4), 1561–1574.

(65) Ziv, N. E.; Smith, S. J. Evidence for a Role of Dendritic Filopodia in Synaptogenesis and Spine Formation. *Neuron* **1996**, *17* (1), 91–102.

(66) Korobova, F.; Svitkina, T. M. Molecular Architecture of Synaptic Actin Cytoskeleton in Hippocampal Neurons Reveals a Mechanism of Dendritic Spine Morphogenesis. *Mol. Biol. Cell* **2010**, *21* (1), 165–176.

(67) Portera-Cailliau, C.; Pan, D. T.; Yuste, R. Activity-Regulated Dynamic Behavior of Early Dendritic Protrusions: Evidence for Different Types of Dendritic Filopodia. *J. Neurosci.* **2003**, *23* (18), 7129–7142.

(68) Berg, K. R. *UC San Diego UC San Diego Electronic Theses and Dissertations Title Investigations into the nootropic effects of ethylene glycol derivatives of benzothiazole aniline*.**2021**.

(69) Wang, J.; Lu, Z.; Wientjes, M. G.; Au, J. L. S. Delivery of SiRNA Therapeutics: Barriers and Carriers. *AAPS Journal*. AAPS J December **2010,** pp 492–503.

(70) Gunawardane, L. S.; Saito, K.; Nishida, K. M.; Miyoshi, K.; Kawamura, Y.; Nagami, T.; Siomi, H.; Siomi, M. C. A Slicer-Mediated Mechanism for Repeat-Associated SiRNA 5′ End Formation in Drosophila. *Science (80-86).* **2007**, *315* (5818), 1587–1590.

(71) Westerink, R. H. S.; Ewing, A. G. The PC12 Cell as Model for Neurosecretion. In *Acta Physiologica*; Acta Physiol (Oxf), **2008**; Vol. 192, pp 273–285.

(72) Guroff, G. PC12 Cells as a Model of Neuronal Differentiation. In *Cell Culture in the Neurosciences*; Springer, Boston, MA, **1985**; pp 245–272.

(73) Radio, N. M.; Breier, J. M.; Shafer, T. J.; Mundy, W. R. Assessmentof Chemical Effects on Neurite Outgrowth in PC12 Cells Using High Content Screening. *Toxicol. Sci.* **2008**, *105* (1), 106–118.

(74) Das, K. P.; Freudenrich, T. M.; Mundy, W. R. Assessment of PC12 Cell Differentiation and Neurite Growth: A Comparison of Morphological and Neurochemical Measures. *Neurotoxicol. Teratol.* **2004**, *26* (3), 397–406.

(75) Southworth, H. N. Scanning Electron Microscopy and Microanalysis. In *Physicochemical Methods of Mineral Analysis*; Springer New York, **1975**; pp 421–450.

(76) Schindelin, J.; Arganda-Carreras, I.; Frise, E.; Kaynig, V.; Longair, M.; Pietzsch, T.; Preibisch, S.; Rueden, C.; Saalfeld, S.; Schmid, B.; Tinevez, J. Y.; White, D. J.; Hartenstein, V.; Eliceiri, K.; Tomancak, P.; Cardona, A. Fiji: An Open-Source Platform for Biological-Image Analysis. *Nature Methods*. Nature Publishing Group June 28, **2012**, pp 676–682.

(77) Kocsis, E.; Trus, B. L.; Steer, C. J.; Bisher, M. E.; Steven, A. C. Image Averaging of Flexible Fibrous Macromolecules: The Clathrin Triskelion Has an Elastic Proximal Segment. *J. Struct. Biol.* **1991**, *107* (1), 6–14.

(78) Yamashiro-Matsumura, S.; Matsumura, F. Purification and Characterization of an F-Actin-Bundling 55-Kilodalton Protein from HeLa Cells. *J. Biol. Chem.* **1985**, *260* (8), 5087–5097.

(79) Huang, J.; Dey, R.; Wang, Y.; Jakoncic, J.; Kurinov, I.; Huang, X. Y. Structural Insights into the Induced-Fit Inhibition of Fascin by a Small-Molecule Inhibitor. *J. Mol. Biol.* **2018**, *430* (9), 1324–1335.

(80) Huang, J.; Dey, R.; Wang, Y.; Jakoncic, J.; Kurinov, I.; Huang, X. Y. Structural Insights into the Induced-Fit Inhibition of Fascin by a Small-Molecule Inhibitor. *J. Mol. Biol.* **2018**, *430* (9), 1324–1335.

(81) Chen, L.; Yang, S.; Jakoncic, J.; Zhang, J. J.; Huang, X. Y. Migrastatin Analogues

Target Fascin to Block Tumour Metastasis. *Nature* **2010**, *464* (7291), 1062–1066.

(82) Alburquerque-González, B.; Bernabé-García, M.; Montoro-García, S.; Bernabé-García, Á.; Rodrigues, P. C.; Ruiz Sanz, J.; López-Calderón, F. F.; Luque, I.; Nicolas, F. J.; Cayuela, M. L.; Salo, T.; Pérez-Sánchez, H.; Conesa-Zamora, P. New Role of the Antidepressant Imipramine as a Fascin1 Inhibitor in Colorectal Cancer Cells. *Exp. Mol. Med.* **2020**, *52* (2), 281–292.

(83) Francis, S.; Croft, D.; Schüttelkopf, A. W.; Parry, C.; Pugliese, A.; Cameron, K.; Claydon, S.; Drysdale, M.; Gardner, C.; Gohlke, A.; Goodwin, G.; Gray, C. H.; Konczal, J.; McDonald, L.; Mezna, M.; Pannifer, A.; Paul, N. R.; Machesky, L.; McKinnon, H.; Bower, J. Structure-Based Design, Synthesis and Biological Evaluation of a Novel Series of Isoquinolone and Pyrazolo[4,3-c] Pyridine Inhibitors of Fascin 1 as Potential Anti-Metastatic Agents. *Bioorganic Med. Chem. Lett.* **2019**, *29* (8), 1023–1029.

(84) Djakovic, S. N.; Schwarz, L. A.; Barylko, B.; DeMartino, G. N.; Patrick, G. N. Regulation of the Proteasome by Neuronal Activity and Calcium/Calmodulin-Dependent Protein Kinase II. *J. Biol. Chem.* **2009**, *284* (39), 26655–26665.

(85) Schwarz, L. A.; Hall, B. J.; Patrick, G. N. Activity-Dependent Ubiquitination of GluA1 Mediates a Distinct AMPA Receptor Endocytosis and Sorting Pathway. *J. Neurosci.* **2010**, *30* (49), 16718–16729.

.

(86) Cartier, A. E.; Djakovic, S. N.; Salehi, A.; Wilson, S. M.; Masliah, E.; Patrick, G. N. Regulation of Synaptic Structure by Ubiquitin C-Terminal Hydrolase L1. *J. Neurosci.* **2009**, *29* (24), 7857–7868.

(87) Schneider, C. A.; Rasband, W. S.; Eliceiri, K. W. NIH Image to ImageJ: 25 Years of Image Analysis. *Nature Methods*. Nature Publishing Group June 28, **2012**, pp 671–675.

(88) Meng, X.-Y.; Zhang, H.-X.; Mezei, M.; Cui, M. Molecular Docking: A Powerful Approach for Structure-Based Drug Discovery. *Curr. Comput. Aided-Drug Des.* **2012**, *7* (2), 146–157.

(89) McConkey, B. J.; Sobolev, V.; Edelman, M. The Performance of Current Methods in Ligand-Protein Docking. *Curr. Sci.* **2002**, *83* (7), 845–856.

(90) Halgren, T. A. Identifying and Characterizing Binding Sites and Assessing Druggability. *J. Chem. Inf. Model.* **2009**, *49* (2), 377–389.

(91) Clarke, D. T. Circular Dichroism and Its Use in Protein-Folding Studies. *Methods Mol. Biol.* **2011**, *752*, 59–72.

(92) Greenfield, N. J. Using Circular Dichroism Spectra to Estimate Protein Secondary

Structure. *Nat. Protoc.* **2007**, *1* (6), 2876–2890.

(93) Freire, E.; Mayorga, O. L.; Straume, M. Isothermal Titration. *Anal. Chem.* **1990**, *62* (18), 950A-959A.

(94) Schrödinger. Maestro | Schrödinger. *Schrödinger Release 2018-1*. **2018**.

(95) Friesner, R. A.; Murphy, R. B.; Repasky, M. P.; Frye, L. L.; Greenwood, J. R.; Halgren, T. A.; Sanschagrin, P. C.; Mainz, D. T. Extra Precision Glide: Docking and Scoring Incorporating a Model of Hydrophobic Enclosure for Protein-Ligand Complexes. *J. Med. Chem.* **2006**, *49* (21), 6177–6196.

(96) Madhavi Sastry, G.; Adzhigirey, M.; Day, T.; Annabhimoju, R.; Sherman, W. Protein and Ligand Preparation: Parameters, Protocols, and Influence on Virtual Screening Enrichments. *J. Comput. Aided. Mol. Des.* **2013**, *27* (3), 221–234.

(97) Molecular Operating Environment. Molecular Operating Environment (MOE). *08;* **2016**.

(98) Pettersen, E. F.; Goddard, T. D.; Huang, C. C.; Couch, G. S.; Greenblatt, D. M.; Meng, E. C.; Ferrin, T. E. UCSF Chimera - A Visualization System for Exploratory Research and Analysis. *J. Comput. Chem.* **2004**, *25* (13), 1605–1612.

(99) Congreve, M.; Murray, C. W.; Blundell, T. L. Keynote Review: Structural Biology and Drug Discovery. *Drug Discovery Today*. Elsevier Current Trends July 1, **2005**, pp 895–907.

(100) Brito, J. A.; Archer, M. X-Ray Crystallography. In *Practical Approaches to Biological Inorganic Chemistry*; Elsevier Inc., **2013**; pp 217–255.

(101) Bruce Alberts; Alexander Johnson; Julian Lewis. Analyzing Protein Structure and Function. In *Molecular Biology of the Cell*; Garland Science, **2002**.

(102) Schlichting, I. X-Ray Crystallography of Protein-Ligand Interactions. In *Methods in Molecular Biology*; Methods Mol Biol, **2005**; Vol. 305, pp 155–165.

(103) Fenwick, R. B.; Esteban-Martiín, S.; Richter, B.; Lee, D.; Walter, K. F. A.; Milovanovic, D.; Becker, S.; Lakomek, N. A.; Griesinger, C.; Salvatella, X. Weak Long-Range Correlated Motions in a Surface Patch of Ubiquitin Involved in Molecular Recognition. *J. Am. Chem. Soc.* **2011**, *133* (27), 10336–10339.

(104) Carugo, O.; Argos, P. Protein-Protein Crystal-Packing Contacts. *Protein Sci.* **1997**, *6* (10), 2261–2263.

(105) DeLucas, L. J.; Hamrick, D.; Cosenza, L.; Nagy, L.; McCombs, D.; Bray, T.; Chait,

A.; Stoops, B.; Belgovskiy, A.; William Wilson, W.; Parham, M.; Chernov, N. Protein Crystallization: Virtual Screening and Optimization. *Progress in Biophysics and Molecular Biology*. Pergamon July 1, **2005**, pp 285–309.

(106) Francis, S.; Croft, D.; Schüttelkopf, A. W.; Parry, C.; Pugliese, A.; Cameron, K.; Claydon, S.; Drysdale, M.; Gardner, C.; Gohlke, A.; Goodwin, G.; Gray, C. H.; Konczal, J.; McDonald, L.; Mezna, M.; Pannifer, A.; Paul, N. R.; Machesky, L.; McKinnon, H.; Bower, J. Structure-Based Design, Synthesis and Biological Evaluation of a Novel Series of Isoquinolone and Pyrazolo[4,3-c]Pyridine Inhibitors of Fascin 1 as Potential Anti-Metastatic Agents. *Bioorganic Med. Chem. Lett.* **2019**, *29* (8), 1023–1029.

(107) Congreve, M.; Carr, R.; Murray, C.; Jhoti, H. A "Rule of Three" for Fragment-Based Lead Discovery? *Drug Discovery Today*. Drug Discov Today October 1, **2003**, pp 876–877.

(108) Blundell, T. L.; Jhoti, H.; Abell, C. High-Throughput Crystallography for Lead Discovery in Drug Design. *Nature Reviews Drug Discovery*. Nature Publishing Group **2002**, pp 45–54.

(109) Dessau, M. A.; Modis, Y. Protein Crystallization for X-Ray Crystallography. *J. Vis. Exp.* **2010**, No. 47.

(110) Palmer, A. G. NMR Characterization of the Dynamics of Biomacromolecules. *Chem. Rev.* **2004**, *104* (8), 3623–3640.

(111) Kay, L. E. NMR Studies of Protein Structure and Dynamics. In *Journal of Magnetic Resonance*; Academic Press, **2005**; Vol. 173, pp 193–207.

(112) Frueh, D. P.; Goodrich, A. C.; Mishra, S. H.; Nichols, S. R. NMR Methods for Structural Studies of Large Monomeric and Multimeric Proteins. *Current Opinion in Structural Biology*. NIH Public Access October **2013**, pp 734–739.

(113) Jiang, Y.; Kalodimos, C. G. NMR Studies of Large Proteins. *Journal of Molecular Biology*. Academic Press August 18, **2017**, pp 2667–2676.

(114) Cavanagh, J.; Fairbrother, W. J.; Palmer, A. G.; Rance, M.; Skelton, N. J. *Protein NMR Spectroscopy: Principles and Practice*; Elsevier, **2006**.

(115) Wüthrich, K. NOE-Observable 1H-1H Distances in Nucleic Acids. In *NMR of proteins and nucleic acid*; John Wiley, **1986**; pp 203–219.

(116) Grzesiek, S.; Bax, A. An Efficient Experiment for Sequential Backbone Assignment of Medium-Sized Isotopically Enriched Proteins. *J. Magn. Reson.* **1992**, *99* (1), 201–207.

(117) Farmer, B. T.; Venters, R. A.; Spicer, L. D.; Wittekind, M. G.; Müller, L. A Refocused and Optimized HNCA: Increased Sensitivity and Resolution in Large Macromolecules. *J. Biomol. NMR* **1992**, *2* (2), 195–202.

(118) Ikura, M.; Kay, L. E.; Bax, A. A Novel Approach for Sequential Assignment of 1H, 13C, and 15N Spectra of Larger Proteins: Heteronuclear Triple-Resonance Three-Dimensional NMR Spectroscopy. Application to Calmodulin. *Biochemistry* **1990**, *29* (19), 4659–4667.

(119) Pervushin, K.; Riek, R.; Wider, G.; Wüthrich, K. Attenuated T2 Relaxation by Mutual Cancellation of Dipole-Dipole Coupling and Chemical Shift Anisotropy Indicates an Avenue to NMR Structures of Very Large Biological Macromolecules in Solution. *Proc. Natl. Acad. Sci. U. S. A.* **1997**, *94* (23), 12366–12371.

(120) Bax, A.; Ikura, M. An Efficient 3D NMR Technique for Correlating the Proton And15N Backbone Amide Resonances with the α-Carbon of the Preceding Residue in Uniformly15N/13C Enriched Proteins. *J. Biomol. NMR* **1991**, *1* (1), 99–104.

(121) Ulrich, E. L.; Akutsu, H.; Doreleijers, J. F.; Harano, Y.; Ioannidis, Y. E.; Lin, J.; Livny, M.; Mading, S.; Maziuk, D.; Miller, Z.; Nakatani, E.; Schulte, C. F.; Tolmie, D. E.; Kent Wenger, R.; Yao, H.; Markley, J. L. BioMagResBank. *Nucleic Acids Res.* **2008**, *36* (SUPPL. 1), D402–D408.

(122) Mielke, S. P.; Krishnan, V. V. Characterization of Protein Secondary Structure from NMR Chemical Shifts. *Progress in Nuclear Magnetic Resonance Spectroscopy*. NIH Public Access April 4, **2009**, pp 141–165.

(123) Kabsch, W. XDS. *Acta Crystallogr. D. Biol. Crystallogr.* **2010**, *66* (Pt 2), 125–132.

(124) McCoy, A. J.; Grosse-Kunstleve, R. W.; Adams, P. D.; Winn, M. D.; Storoni, L. C.; Read, R. J. Phaser Crystallographic Software. *J. Appl. Crystallogr.* **2007**, *40* (4), 658–674.

(125) Emsley, P.; Lohkamp, B.; Scott, W. G.; Cowtan, K. Features and Development of Coot. *Acta Crystallogr. Sect. D Biol. Crystallogr.* **2010**, *66* (4), 486–501.

(126) Adams, P. D.; Afonine, P. V.; Bunkóczi, G.; Chen, V. B.; Davis, I. W.; Echols, N.; Headd, J. J.; Hung, L. W.; Kapral, G. J.; Grosse-Kunstleve, R. W.; McCoy, A. J.; Moriarty, N. W.; Oeffner, R.; Read, R. J.; Richardson, D. C.; Richardson, J. S.; Terwilliger, T. C.; Zwart, P. H. PHENIX: A Comprehensive Python-Based System for Macromolecular Structure Solution. *Acta Crystallogr. Sect. D Biol. Crystallogr.* **2010**, *66* (2), 213–221.

(127) Bruker. *TopSpin | NMR Data Analysis | Bruker*.

(128) Petrauskas, V.; Kazlauskas, E.; Gedgaudas, M.; Baranauskienė, L.; Zubrienė, A.; Matulis, D. Thermal Shift Assay for Protein–Ligand Dissociation Constant Determination. *TrAC - Trends in Analytical Chemistry*. Elsevier January 1, **2024**, p 117417.

(129) Hodson, R. Inflammatory Bowel Disease. *Nature*. Massachusetts Medical Society November 19, **2016**, p S97.

(130) Dotson, J. L.; Boyle, B. Crohn Disease. In *Pediatric Gastrointestinal and Liver Disease, Sixth Edition*; StatPearls Publishing, **2020**; pp 461-473.e8.

(131) Ungaro, R.; Mehandru, S.; Allen, P. B.; Peyrin-Biroulet, L.; Colombel, J. F. Ulcerative Colitis. *The Lancet*. Lancet April 29, **2017**, pp 1756–1770.

(132) Baumgart, D. C.; Carding, S. R. Inflammatory Bowel Disease: Cause and Immunobiology. *Lancet*. Lancet May 12, **2007**, pp 1627–1640.

(133) Kaplan, G. G. The Global Burden of IBD: From 2015 to 2025. *Nature Reviews Gastroenterology and Hepatology*. Nat Rev Gastroenterol Hepatol December 1, **2015**, pp 720–727.

(134) Kornbluth, A.; Sachar, D. B. Ulcerative Colitis Practice Guidelines in Adults: American College of Gastroenterology, Practice Parameters Committee. *American Journal of Gastroenterology*. Am J Gastroenterol **2010**, pp 501–523.

(135) Rutgeerts, P.; Vermeire, S.; Van Assche, G. Biological Therapies for Inflammatory Bowel Diseases. *Gastroenterology*. Gastroenterology **2009**, pp 1182–1197.

(136) Ewe, K.; Press, A. G.; Singe, C. C.; Stufler, M.; Ueberschaer, B.; Hommel, G.; Büschenfelde, K. H. M. Zum. Azathioprine Combined with Prednisolone or Monotherapy with Prednisolone in Active Crohn's Disease. *Gastroenterology* **1993**, *105* (2), 367–372.

(137) Feagan, B. G.; Rochon, J.; Fedorak, R. N.; Irvine, E. J.; Wild, G.; Sutherland, L.; Steinhart, A. H.; Greenberg, G. R.; Gillies, R.; Hopkins, M.; Hanauer, S. B.; McDonald, J. W. D. Methotrexate for the Treatment of Crohn's Disease. *N. Engl. J. Med.* **1995**, *332* (5), 292–297.

(138) Hanauer, S. B.; Feagan, B. G.; Lichtenstein, G. R.; Mayer, L. F.; Schreiber, S.; Colombel, J. F.; Rachmilewitz, D.; Wolf, D. C.; Olson, A.; Bao, W.; Rutgeerts, P. Maintenance Infliximab for Crohn's Disease: The ACCENT I Randomised Trial. *Lancet* **2002**, *359* (9317), 1541–1549.

(139) Sandborn, W. J.; Van Assche, G.; Reinisch, W.; Colombel, J.; D'Haens, G.; Wolf, D. C.; Kron, M.; Tighe, M. B.; Lazar, A.; Thakkar, R. B. Adalimumab Induces and Maintains Clinical Remission in Patients with Moderate-to-Severe Ulcerative

Colitis. *Gastroenterology* **2012**, *142* (2).

(140) Cohen, J. L.; Strong, S. A.; Hyman, N. H.; Buie, W. D.; Dunn, G. D.; Ko, C. Y.; Fleshner, P. R.; Stahl, T. J.; Kim, D. G.; Bastawrous, A. L.; Perry, W. B.; Cataldo, P. A.; Rafferty, J. F.; Ellis, C. N.; Rakinic, J.; Gregorcyk, S.; Shellito, P. C.; Kilkenny, J. W.; Ternent, C. A.; Koltun, W.; Tjandra, J. J.; Orsay, C. P.; Whiteford, M. H.; Penzer, J. R. Practice Parameters for the Surgical Treatment of Ulcerative Colitis. *Dis. Colon Rectum* **2005**, *48* (11), 1997–2009.

(141) Ba'ath, M. E.; Mahmalat, M. W.; Kapur, P.; Smith, N. P.; Dalzell, A. M.; Casson, D. H.; Lamont, G. L.; Baillie, C. T. Surgical Management of Inflammatory Bowel Disease. *Arch. Dis. Child.* **2007**, *92* (4), 312–316.

(142) Ben-Horin, S.; Chowers, Y. Review Article: Loss of Response to Anti-TNF Treatments in Crohn's Disease. *Alimentary Pharmacology and Therapeutics*. Aliment Pharmacol Ther **2011**, pp 987–995.

(143) Ahluwalia, J. P. Immunotherapy in Inflammatory Bowel Disease. *Medical Clinics of North America*. Med Clin North Am May **2012**, pp 525–544.

(144) Sahoo, D.; Swanson, L.; Sayed, I. M.; Katkar, G. D.; Ibeawuchi, S. R.; Mittal, Y.; Pranadinata, R. F.; Tindle, C.; Fuller, M.; Stec, D. L.; Chang, J. T.; Sandborn, W. J.; Das, S.; Ghosh, P. Artificial Intelligence Guided Discovery of a Barrier-Protective Therapy in Inflammatory Bowel Disease. *Nat. Commun.* **2021**, *12* (1), 1–14.

(145) Shen, L.; Su, L.; Turner, J. R. Mechanisms and Functional Implications of Intestinal Barrier Defects. *Digestive Diseases*. Dig Dis November **2009**, pp 443–449.

(146) Chang, J.; Leong, R. W.; Wasinger, V. C.; Ip, M.; Yang, M.; Phan, T. G. Impaired Intestinal Permeability Contributes to Ongoing Bowel Symptoms in Patients With Inflammatory Bowel Disease and Mucosal Healing. *Gastroenterology* **2017**, *153* (3), 723-731.

.

(147) Florholmen, J. Mucosal Healing in the Era of Biologic Agents in Treatment of Inflammatory Bowel Disease. *Scandinavian Journal of Gastroenterology*. Scand J Gastroenterol January 1, **2014**, pp 43–52.

(148) Fries, W.; Belvedere, A.; Vetrano, S. Sealing the Broken Barrier in IBD: Intestinal Permeability, Epithelial Cells and Junctions. *Curr. Drug Targets* **2013**, *14* (12), 1460–1470.

(149) Kiesslich, R.; Duckworth, C. A.; Moussata, D.; Gloeckner, A.; Lim, L. G.; Goetz, M.; Pritchard, D. M.; Galle, P. R.; Neurath, M. F.; Watson, A. J. M. Local Barrier Dysfunction Identified by Confocal Laser Endomicroscopy Predicts Relapse in

Inflammatory Bowel Disease. *Gut* **2012**, *61* (8), 1146–1153.

(150) D'Incà, R.; De Leo, V.; Corrao, G.; Martines, D.; D'Odorico, A.; Mestriner, C.; Venturi, C.; Longo, G.; Sturniolo, G. C. Intestinal Permeability Test As A Predictor of Clinical Course in Crohn's Disease. *Am. J. Gastroenterol.* **1999**, *94* (10), 2956–2960.

(151) Yan, Y.; Zhou, X. E.; Xu, H. E.; Melcher, K. Structure and Physiological Regulation of AMPK. *International Journal of Molecular Sciences*. Int J Mol Sci November 9, **2018**.

(152) Kim, J.; Yang, G.; Kim, Y.; Kim, J.; Ha, J. AMPK Activators: Mechanisms of Action and Physiological Activities. *Experimental and Molecular Medicine*. Exp Mol Med April 22, **2016**.

(153) Xue, Y.; Zhang, H.; Sun, X.; Zhu, M. J. Metformin Improves Ileal Epithelial Barrier Function in Interleukin-10 Deficient Mice. *PLoS One* **2016**, *11* (12), e0168670.

(154) Koh, S. J.; Kim, J. M.; Kim, I. K.; Ko, S. H.; Kim, J. S. Anti-Inflammatory Mechanism of Metformin and Its Effects in Intestinal Inflammation and Colitis-Associated Colon Cancer. *J. Gastroenterol. Hepatol.* **2014**, *29* (3), 502–510.

(155) Xu, B.; Li, Y. L.; Xu, M.; Yu, C. C.; Lian, M. Q.; Tang, Z. Y.; Li, C. X.; Lin, Y. Geniposide Ameliorates TNBS-Induced Experimental Colitis in Rats via Reducing Inflammatory Cytokine Release and Restoring Impaired Intestinal Barrier Function. *Acta Pharmacol. Sin.* **2017**, *38* (5), 688–698.

(156) Takahara, M.; Takaki, A.; Hiraoka, S.; Adachi, T.; Shimomura, Y.; Matsushita, H.; Nguyen, T. T. T.; Koike, K.; Ikeda, A.; Takashima, S.; Yamasaki, Y.; Inokuchi, T.; Kinugasa, H.; Sugihara, Y.; Harada, K.; Eikawa, S.; Morita, H.; Udono, H.; Okada, H. Berberine Improved Experimental Chronic Colitis by Regulating Interferon-γ- and IL-17A-Producing Lamina Propria CD4+ T Cells through AMPK Activation. *Sci. Rep.* **2019**, *9* (1).

(157) Bai, A.; Ma, A. G.; Yong, M.; Weiss, C. R.; Ma, Y.; Guan, Q.; Bernstein, C. N.; Peng, Z. AMPK Agonist Downregulates Innate and Adaptive Immune Responses in TNBS-Induced Murine Acute and Relapsing Colitis. *Biochem. Pharmacol.* **2010**, *80* (11), 1708–1717.

(158) Chen, L.; Wang, J.; You, Q.; He, S.; Meng, Q.; Gao, J.; Wu, X.; Shen, Y.; Sun, Y.; Wu, X.; Xu, Q. Activating AMPK to Restore Tight Junction Assembly in Intestinal Epithelium and to Attenuate Experimental Colitis by Metformin. *Front. Pharmacol.* **2018**, *9* (JUL).

(159) Blagih, J.; Coulombe, F.; Vincent, E. E.; Dupuy, F.; Galicia-Vázquez, G.; Yurchenko, E.; Raissi, T. C.; VanderWindt, G. J. W.; Viollet, B.; Pearce, E. L.;

Pelletier, J.; Piccirillo, C. A.; Krawczyk, C. M.; Divangahi, M.; Jones, R. G. The Energy Sensor AMPK Regulates T Cell Metabolic Adaptation and Effector Responses InVivo. *Immunity* **2015**, *42* (1), 41–54.

(160) Salminen, A.; Kaarniranta, K. AMP-Activated Protein Kinase (AMPK) Controls the Aging Process via an Integrated Signaling Network. *Ageing Research Reviews*. Ageing Res Rev April **2012**, pp 230–241.

(161) Yang, W. L.; Perillo, W.; Liou, D.; Marambaud, P.; Wang, P. AMPK Inhibitor Compound C Suppresses Cell Proliferation by Induction of Apoptosis and Autophagy in Human Colorectal Cancer Cells. *J. Surg. Oncol.* **2012**, *106* (6), 680–688.

(162) Zheng, L.; Kelly, C. J.; Colgan, S. P. Physiologic Hypoxia and Oxygen Homeostasis in the Healthy Intestine. A Review in the Theme: Cellular Responses to Hypoxia. *Am. J. Physiol. - Cell Physiol.* **2015**, *309* (6), C350–C360.

(163) Kim, J.; Kundu, M.; Viollet, B.; Guan, K. L. AMPK and MTOR Regulate Autophagy through Direct Phosphorylation of Ulk1. *Nat. Cell Biol.* **2011**, *13* (2), 132–141.

(164) Hardie, D. G. AMPK and Autophagy Get Connected. *EMBO Journal*. Nature Publishing Group February 2, **2011**, pp 634–635.

(165) Scott, J. W.; Ling, N.; Issa, S. M. A.; Dite, T. A.; O'Brien, M. T.; Chen, Z. P.; Galic, S.; Langendorf, C. G.; Steinberg, G. R.; Kemp, B. E.; Oakhill, J. S. Small Molecule Drug A-769662 and AMP Synergistically Activate Naive AMPK Independent of Upstream Kinase Signaling. *Chem. Biol.* **2014**, *21* (5), 619–627.

(166) Cool, B.; Zinker, B.; Chiou, W.; Kifle, L.; Cao, N.; Perham, M.; Dickinson, R.; Adler, A.; Gagne, G.; Iyengar, R.; Zhao, G.; Marsh, K.; Kym, P.; Jung, P.; Camp, H. S.; Frevert, E. Identification and Characterization of a Small Molecule AMPK Activator That Treats Key Components of Type 2 Diabetes and the Metabolic Syndrome. *Cell Metab.* **2006**, *3* (6), 403–416.

(167) Cameron, K. O.; Kung, D. W.; Kalgutkar, A. S.; Kurumbail, R. G.; Miller, R.; Salatto, C. T.; Ward, J.; Withka, J. M.; Bhattacharya, S. K.; Boehm, M.; Borzilleri, K. A.; Brown, J. A.; Calabrese, M.; Caspers, N. L.; Cokorinos, E.; Conn, E. L.; Dowling, M. S.; Edmonds, D. J.; Eng, H.; Fernando, D. P.; Frisbie, R.; Hepworth, D.; Landro, J.; Mao, Y.; Rajamohan, F.; Reyes, A. R.; Rose, C. R.; Ryder, T.; Shavnya, A.; Smith, A. C.; Tu, M.; Wolford, A. C.; Xiao, J. Discovery and Preclinical Characterization of 6-Chloro-5-[4-(1-Hydroxycyclobutyl)Phenyl]-1H-Indole-3-Carboxylic Acid (PF-06409577), a Direct Activator of Adenosine Monophosphate-Activated Protein Kinase (AMPK), for the Potential Treatment of Diabetic Neph. *J. Med. Chem.* **2016**, *59* (17), 8068–8081.

(168) Wolber, G.; Langer, T. LigandScout: 3-D Pharmacophores Derived from Protein-

Bound Ligands and Their Use as Virtual Screening Filters. *J. Chem. Inf. Model.* **2005**, *45* (1), 160–169.

(169) Xiao, B.; Sanders, M. J.; Carmena, D.; Bright, N. J.; Haire, L. F.; Underwood, E.; Patel, B. R.; Heath, R. B.; Walker, P. A.; Hallen, S.; Giordanetto, F.; Martin, S. R.; Carling, D.; Gamblin, S. J. Structural Basis of AMPK Regulation by Small Molecule Activators. *Nat. Commun.* **2013**, *4*.

(170) Yan, Y.; Edward Zhou, X.; Novick, S. J.; Shaw, S. J.; Li, Y.; Brunzelle, J. S.; Hitoshi, Y.; Griffin, P. R.; Eric Xu, H.; Melcher, K. Structures of AMP-Activated Protein Kinase Bound to Novel Pharmacological Activators in Phosphorylated, Non-Phosphorylated, and Nucleotide-Free States. *J. Biol. Chem.* **2019**, *294* (3), 953–967.

(171) Cokorinos, E. C.; Delmore, J.; Reyes, A. R.; Albuquerque, B.; Kjøbsted, R.; Jørgensen, N. O.; Tran, J. L.; Jatkar, A.; Cialdea, K.; Esquejo, R. M.; Meissen, J.; Calabrese, M. F.; Cordes, J.; Moccia, R.; Tess, D.; Salatto, C. T.; Coskran, T. M.; Opsahl, A. C.; Flynn, D.; Blatnik, M.; Li, W.; Kindt, E.; Foretz, M.; Viollet, B.; Ward, J.; Kurumbail, R. G.; Kalgutkar, A. S.; Wojtaszewski, J. F. P.; Cameron, K. O.; Miller, R. A. Activation of Skeletal Muscle AMPK Promotes Glucose Disposal and Glucose Lowering in Non-Human Primates and Mice. *Cell Metab.* **2017**, *25* (5), 1147-1159.

(172) Ryder, T. F.; Calabrese, M. F.; Walker, G. S.; Cameron, K. O.; Reyes, A. R.; Borzilleri, K. A.; Delmore, J.; Miller, R.; Kurumbail, R. G.; Ward, J.; Kung, D. W.; Brown, J. A.; Edmonds, D. J.; Eng, H.; Wolford, A. C.; Kalgutkar, A. S. Acyl Glucuronide Metabolites of 6-Chloro-5-[4-(1-Hydroxycyclobutyl)Phenyl]-1 H-Indole-3-Carboxylic Acid (PF-06409577) and Related Indole-3-Carboxylic Acid Derivatives Are Direct Activators of Adenosine Monophosphate-Activated Protein Kinase (AMPK). *J. Med. Chem.* **2018**, *61* (16), 7273–7288.

(173) Salatto, C. T.; Miller, R. A.; Cameron, K. O.; Cokorinos, E.; Reyes, A.; Ward, J.; Calabrese, M. F.; Kurumbail, R. G.; Rajamohan, F.; Kalgutkar, A. S.; Tess, D. A.; Shavnya, A.; Genung, N. E.; Edmonds, D. J.; Jatkar, A.; Maciejewski, B. S.; Amaro, M.; Gandhok, H.; Monetti, M.; Cialdea, K.; Bollinger, E.; Kreeger, J. M.; Coskran, T. M.; Opsahl, A. C.; Boucher, G. G.; Birnbaum, M. J.; DaSilva-Jardine, P.; Rolph, T. Selective Activation of AMPK B1-Containing Isoforms Improves Kidney Function in a Rat Model of Diabetic Nephropathy. *J. Pharmacol. Exp. Ther.* **2017**, *361* (2), 303–311.

(174) Ngoei, K. R. W.; Langendorf, C. G.; Ling, N. X. Y.; Hoque, A.; Varghese, S.; Camerino, M. A.; Walker, S. R.; Bozikis, Y. E.; Dite, T. A.; Ovens, A. J.; Smiles, W. J.; Jacobs, R.; Huang, H.; Parker, M. W.; Scott, J. W.; Rider, M. H.; Foitzik, R. C.; Kemp, B. E.; Baell, J. B.; Oakhill, J. S. Structural Determinants for Small-Molecule Activation of Skeletal Muscle AMPK A2β2γ1 by the Glucose Importagog SC4. *Cell Chem. Biol.* **2018**, *25* (6), 728-737.

(175) Langendorf, C. G.; Ngoei, K. R. W.; Scott, J. W.; Ling, N. X. Y.; Issa, S. M. A.; Gorman, M. A.; Parker, M. W.; Sakamoto, K.; Oakhill, J. S.; Kemp, B. E. Structural Basis of Allosteric and Synergistic Activation of AMPK by Furan-2-Phosphonic Derivative C2 Binding. *Nat. Commun.* **2016**, *7*.

(176) Calabrese, M. F.; Rajamohan, F.; Harris, M. S.; Caspers, N. L.; Magyar, R.; Withka, J. M.; Wang, H.; Borzilleri, K. A.; Sahasrabudhe, P. V.; Hoth, L. R.; Geoghegan, K. F.; Han, S.; Brown, J.; Subashi, T. A.; Reyes, A. R.; Frisbie, R. K.; Ward, J.; Miller, R. A.; Landro, J. A.; Londregan, A. T.; Carpino, P. A.; Cabral, S.; Smith, A. C.; Conn, E. L.; Cameron, K. O.; Qiu, X.; Kurumbail, R. G. Structural Basis for AMPK Activation: Natural and Synthetic Ligands Regulate Kinase Activity from Opposite Poles by Different Molecular Mechanisms. *Structure* **2014**, *22* (8), 1161–1172.

(177) Ovens, A. J.; Gee, Y. S.; Ling, N. X. Y.; Yu, D.; Hardee, J. P.; Chung, J. D.; Ngoei, K. R. W.; Waters, N. J.; Hoffman, N. J.; Scott, J. W.; Loh, K.; Spengler, K.; Heller, R.; Parker, M. W.; Lynch, G. S.; Huang, F.; Galic, S.; Kemp, B. E.; Baell, J. B.; Oakhill, J. S.; Langendorf, C. G. Structure-Function Analysis of the AMPK Activator SC4 and Identification of a Potent Pan AMPK Activator. *Biochem. J.* **2022**, *479* (11), 1181–1204.

(178) Li, X.; Wang, L.; Zhou, X. E.; Ke, J.; De Waal, P. W.; Gu, X.; Tan, M. H. E.; Wang, D.; Wu, D.; Xu, H. E.; Melcher, K. Structural Basis of AMPK Regulation by Adenine Nucleotides and Glycogen. *Cell Res.* **2015**, *25* (1), 50–66.

(179) Hardie, D. G.; Ross, F. A.; Hawley, S. A. AMP-Activated Protein Kinase: A Target for Drugs Both Ancient and Modern. *Chemistry and Biology*. Europe PMC Funders October 10, **2012**, pp 1222–1236.

(180) Ren, J. X.; Li, L. L.; Zou, J.; Yang, L.; Yang, J. L.; Yang, S. Y. Pharmacophore Modeling and Virtual Screening for the Discovery of New Transforming Growth Factor-β Type I Receptor (ALK5) Inhibitors. *Eur. J. Med. Chem.* **2009**, *44* (11), 4259–4265.

(181) Feng, D.; Biftu, T.; Romero, F. A.; Kekec, A.; Dropinski, J.; Kassick, A.; Xu, S.; Kurtz, M. M.; Gollapudi, A.; Shao, Q.; Yang, X.; Lu, K.; Zhou, G.; Kemp, D.; Myers, R. W.; Guan, H. P.; Trujillo, M. E.; Li, C.; Weber, A.; Sebhat, I. K. Discovery of MK-8722: A Systemic, Direct Pan-Activator of AMP-Activated Protein Kinase. *ACS Med. Chem. Lett.* **2018**, *9* (1), 39–44.

(182) Lyne, P. D. Structure-Based Virtual Screening: An Overview. *Drug Discovery Today*. Drug Discov Today October 15, **2002**, pp 1047–1055.

(183) Kitchen, D. B.; Decornez, H.; Furr, J. R.; Bajorath, J. Docking and Scoring in Virtual Screening for Drug Discovery: Methods and Applications. *Nature Reviews*

Drug Discovery. Nat Rev Drug Discov November **2004**, pp 935–949.

(184) Zaharevd; McCormack, K. *Compound Sets - NCI DTP Data - NCI Wiki*.

(185) Zweifach, A. The National Cancer Institute's Plated Compound Sets Can Be a Valuable Resource for Academic Researchers. *SLAS Discov.* **2020**, *25* (1), 2–6.

(186) Wang, J.; Ge, Y.; Xie, X. Q. Development and Testing of Druglike Screening Libraries. *J. Chem. Inf. Model.* **2019**, *59* (1), 53–65.

(187) Rajamohan, F.; Harris, M. S.; Frisbie, R. K.; Hoth, L. R.; Geoghegan, K. F.; Valentine, J. J.; Reyes, A. R.; Landro, J. A.; Qiu, X.; Kurumbail, R. G. Escherichia Coli Expression, Purification and Characterization of Functional Full-Length Recombinant A2β2γ3 Heterotrimeric Complex of Human AMP-Activated Protein Kinase. *Protein Expr. Purif.* **2010**, *73* (2), 189–197.

(188) Day, E. A.; Ford, R. J.; Steinberg, G. R. AMPK as a Therapeutic Target for Treating Metabolic Diseases. *Trends in Endocrinology and Metabolism*. Trends Endocrinol Metab August 1, **2017**, pp 545–560.

(189) Smith, D. B.; Johnson, K. S. Single-Step Purification of Polypeptides Expressed in Escherichia Coli as Fusions with Glutathione S-Transferase. *Gene* **1988**, *67* (1), 31–40.

.

(190) Promega. *Kinase-Glo® Luminescent Kinase Assays*.

(191) Yu, D.; Peng, Y.; Ayaz-Guner, S.; Gregorich, Z. R.; Ge, Y. Comprehensive Characterization of AMP-Activated Protein Kinase Catalytic Domain by Top-Down Mass Spectrometry. *J. Am. Soc. Mass Spectrom.* **2016**, *27* (2), 220–232.

(192) Chandrashekarappa, D. G.; McCartney, R. R.; Schmidt, M. C. Ligand Binding to the AMP-Activated Protein Kinase Active Site Mediates Protection of the Activation Loop from Dephosphorylation. *J. Biol. Chem.* **2013**, *288* (1), 89–98.

(193) Protein Atlas. *PNOC protein expression summary - The Human Protein Atlas*. https://www.proteinatlas.org/ENSG00000131791-PRKAB2

(194) Motoshima, H.; Goldstein, B. J.; Igata, M.; Araki, E. AMPK and Cell Proliferation – AMPK as a Therapeutic Target for Atherosclerosis and Cancer. *J. Physiol.* **2006**, *574* (1), 63–71.

(195) Protein Atlas. *PNOC protein expression summary - The Human Protein Atlas*. https://www.proteinatlas.org/ENSG00000111725-PRKAB1

(196) Hammes, G. G.; Wu, C. W. Kinetics of Allosteric Enzymes. *Annual review of biophysics and bioengineering*. **1974**, pp 1–33.

(197) Demongeot, J.; Laurent, M. Sigmoidicity in Allosteric Models. *Math. Biosci.* **1983**, *67* (1), 1–17.